Optical properties of hydrogenated graphene and Fe/GaAs(001) from first principles

Dissertation

zur Erlangung des Doktorgrades der Naturwissenschaften
(Dr. rer. nat.) der Fakultät für Physik der Universität Regensburg

vorgelegt von

Sebastian Putz

aus Hutthurm

im Jahr 2014

Das Promotionsgesuch wurde eingereicht am: 16. April 2014
Das Promotionskolloquium fand statt am: 30. Juni 2014
Die Arbeit wurde angeleitet von: Prof. Dr. Jaroslav Fabian

Vorsitzender: Prof. Dr. Christian Back
1. Gutachter: Prof. Dr. Jaroslav Fabian
2. Gutachter: Prof. Dr. Thomas Niehaus
Weiterer Prüfer: Prof. Dr. Andreas Schäfer

Contents

Preface

“Nature isn’t classical, dammit, and if you want to make a simulation of nature, you’d better make it quantum mechanical, and by golly it’s a wonderful problem, because it doesn’t look so easy.” This is how Richard Feynman concluded his 1981 speech on *Simulating Physics with Computers* [1]. He would certainly rejoice in the progress that has been made since then, but simulating nature on the computer continues to be a fascinating challenge.

This dissertation is an account of what I have learned about simulating physics on the computer, applied to a set of material systems in the field of spintronics. I have tried to not only present the usual problem-method-results scheme, but also to provide a broader—and sometimes interdisciplinary—context to bolster the hard facts. While this work is certainly intended to present research results, it was very important to me that this thesis provide introductory reading for my successors in our research group, or for anyone who is interested in *ab initio* calculations of solid-state optics. It was written with that goal in mind.

The material systems investigated in this study are hydrogenated graphene and the Fe/GaAs(001) heterostructure. Both systems are of great interest to semiconductor spintronics. While Fe/GaAs(001) is a prototypical spin injection device, hydrogenated graphene offers a reversibly tunable band gap, allowing for its use in novel spin manipulation devices. Learning more about hydrogenated graphene thus contributes to the second pillar of spintronics (spin manipulation), whereas understanding Fe/GaAs(001) advances the first and the third pillar (spin injection and spin detection).

These systems have been studied previously, with a focus on the anisotropic transport properties of Fe/GaAs(001), and the structural, electronic, and thermodynamic properties of hydrogenated graphene. However, a systematic study of their optical properties was missing. Optical methods are often ideal tools for investigating solid-state systems. They are usually non-invasive, allowing for samples to be studied *in situ*, well understood, very accurate, and they can often be implemented as relatively simple and cheap setups.

One of the main ideas leading to this work was to motivate and facilitate the use of optical methods in the experimental study of hydrogenated graphene and Fe/GaAs(001). The results presented here cover a large photon energy range, providing guidelines for selecting the energy at which the samples should be probed. I genuinely hope that experimentalists will find the results of this thesis interesting, and that they devise experiments that put them to fruitful use.

The challenges in calculating optical properties from scratch (*ab initio*) are manifold. First, one has to select suitable model systems that can be calculated with reasonable effort. They have to be represented as a periodically repeated unit cell, if possible with optimized structure. Next, the right method (code package) needs to be chosen. Then the electronic band structure is obtained from the self-consistent electron density. The optical properties are calculated on top of that. Most importantly, all these results must be converged, which is possibly the biggest challenge, especially when it comes to optics. However, the obtained results are timely and can help advance semiconductor spintronics, which certainly outweighs the effort.

Finally, let me describe how this thesis is organized. The first chapter shows how the scientific trinity of theory, experiment, and simulation continues to push back the frontiers of our knowledge. *Ab initio* material calculations are introduced as a particular type of simulation. Chapter 2 is a pedagogical account of theoretical and practical aspects of density functional theory methods for the solid state. Theoretical background on the optical properties of solids is given in the third chapter, along with the formalism used to interpret the specific results for the optical conductivity of hydrogenated graphene (Ch. 4), and the anisotropic polar magneto-optical Kerr effect of Fe/GaAs (Ch. 5). Major parts of Chapter 4 and 5 are based on the references [2] and [3], respectively.

Regensburg, April 2014 Sebastian Putz

1

The Study of Structure

Humans are strange creatures. As naked apes with feeble arms and voices, lacking claws and fangs, we have become thinkers and tinkers in a continuous endeavor to extend our minds and bodies. Applying the few biological assets we have—hands, brains, and larynx—humans have developed language and tools in an unprecedented co-evolution of cognitive and motor abilities. The purest of our languages is mathematics, and the scientific method our sharpest tool.

The biological evolution of our bodies operates on a timescale orders of magnitude longer than a lifetime, which is why the evolution of modern humans for the last 10,000 years has been an evolution of ideas. Ideas are structured sets of information capable of interaction, reproduction and evolution—just like genes—for which the term *memes* was coined [4]. While genes are encoded in the structure of a complex biomolecule, memes are abstract entities encoded in the interaction of neurons. In that sense, genes and memes are just two instances of the same abstraction: information encoded in structure.

To form ideas we need information, but our biological sensors provide only narrow channels for information input. We see only a tiny fraction of the electromagnetic spectrum, we hear only a very limited range of acoustic frequencies, we can smell and taste only a small portion of molecules, and all that with poor resolution. Given this limited sensory input and the average physical size of our bodies, it is not surprising that the human brain cannot deal comfortably with small and large scales. The way we overcome this mediocrity is by extending our phenotype [5], by building tools that widen our information channels to include smaller and larger orders of magnitude: microscopes and telescopes.

The information gathered with these instruments does not have any inherent structure, and the massive amount of information flowing in through our artificially widened input channels needs to be analyzed, structured, and interpreted. After many useless or outright destructive approaches, including superstition and religion, the scientific method—essentially a formalized version of childlike curiosity—has prevailed as the only system of thought that takes reality seriously. It is the knife with which we carve models of reality out of randomness by falsification. These models are then cast into the language of mathematics, which is our universal way of describing structure, to spark new ideas and to aid in the development of new tools, eventually leading to the formation of new models in a possibly infinite cycle of discovery, description, and development.

What can we learn from that? The first important conclusion is that structure encodes information relevant to higher levels of the structural hierarchy, as Philip Anderson has so famously observed in his seminal 1972 paper *More Is Different* [6]. Electrons and quarks are "not aware" that they form atoms, atoms are not aware that they form molecules, molecules that they form cells, cells that they form multicellular organisms capable of composing a symphony or killing each other—they simply interact with entities of the same type without regard for the function of the structure they form, and yet they contribute to the emergence of phenomena one level higher. This means that to understand a system we to need go at least one level deeper in our investigations.

The second conclusion, in the words of Francis Crick, is that in order to understand function, we need to study structure [7] (and that is exactly what he did). Indeed, structured information, encoded in physical entities and their interactions, is a universal, cosmic idea. Physics, the ultimate fundamental science, is in essence the study of structure and interaction.

1.1 Simulation – Computing Reality

The scientific method is the way scientific inquiry is put into practice. Observations of inexplicable natural phenomena or the pursuit of a technological goal demand a scientific answer to the question of why a particular phenomenon occured, or how a goal can be achieved. Based on current knowledge, a hypothesis is formed that provides a possible answer, and that can be used to make testable predictions. The hypothesis is then tested in experiments in order to falsify those predictions under reproducible, controlled conditions.

If the hypothesis is found to be false it has to be modified and the cycle starts over. In case the hypothesis has not been falsified after several independent repetitions of an experiment it can be considered established knowledge. If they refer to related subjects, many such hypotheses form a scientific theory, which is an elaborate set of accumulated knowledge about a specific trait of nature.

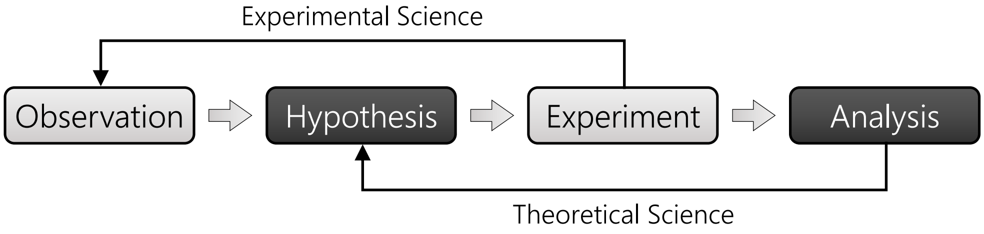

Figure 1.1 – The scientific method as the formalized process of scientific inquiry.

Over the last centuries the natural sciences have evolved in a process of differentiation and specialization. The division of labor makes scientific research more efficient: theoretical research focuses on forming hypotheses and analyzing results, while experimental research performs experiments and makes new observations. All this assumes that we are able to describe our subject of inquiry theoretically, and that we can devise a suitable experiment. But what if the system is too complex for theoretical treatment, too big, intricate, or costly for experimental study? With the ever-increasing computational power available to us, a third branch of science continues to thrive: simulation.

The human brain is the most complex system known. With only about 10 watts of power consumption it can perform between 10^{13} and 10^{16} synaptic operations per second [8]. Its strength lies in connecting information, processing it collectively, and finding patterns in it. However, it performs poorly when it comes to bulk logical operations, lacking both speed and memory. Computers complement and extend our brains, and enable us to deal with amounts of information orders of magnitude larger than what all human brains together could ever process. They are the simulation tool we use to cope with systems too complex for purely theoretical and experimental study. The relationship of theory, experiment, and simulation is best illustrated by the *Landau Triangle* [9, 10].[1]

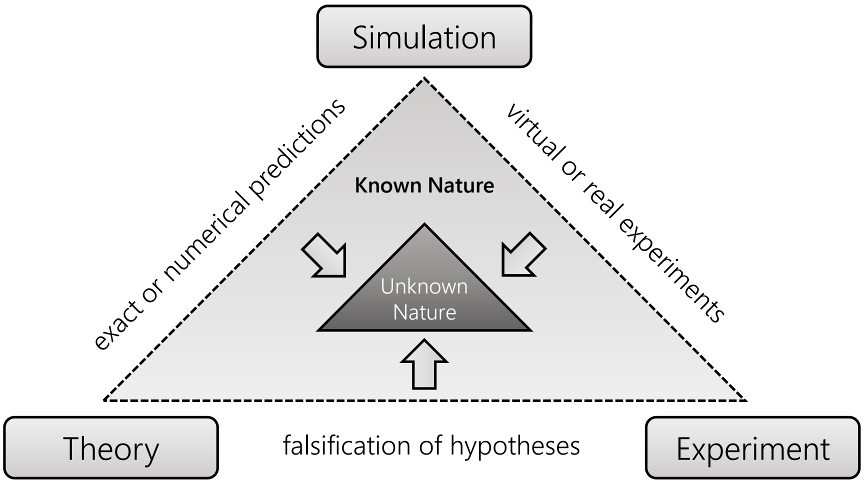

Figure 1.2 – The Landau Triangle illustrates how theoretical, experimental, and computational science interact to decrease our ignorance about nature.

We have learned that in order to understand a phenomenon on one level of the structural hierarchy, we need to go one level deeper and study the components of the system and their interactions. What does that mean for simulation, which is basically a virtual experiment? It means that we need to describe the components and interactions of the system at hand as accurately as we can because their collective behavior results in the effects we seek to study one hierarchical level higher. That reveals the twofold purpose of simulations: On one hand, if we understand the components of a complex system very well, we can use a simulation to predict the behavior of the system with confidence. On the other hand, by comparing the simulation of a system to reality, we can test how well we understand the components of the system.

---

[1] Many things in physics are named after Lev Davidovich Landau, but the Landau Triangle was established by David P. Landau, professor of physics at the University of Georgia.

Solid state physics is a good example. Solids are collections of vast numbers of atoms in various degrees of ordering. The properties and effects on the level of the solid can only be understood by investigating how the components of the solid—electrons and nuclei—interact with each other or with external perturbations. If we have sufficient understanding of those components and how they interact to form a solid, and if we can translate this to a format a computer can handle, we can simulate solids and predict their properties. This is where *ab initio* calculations enter the stage.

1.2 The Purest of Calculations

The Latin term *ab initio* translates to "from the beginning." This means that an *ab initio* calculation is an attempt to describe a system *in its entirety* using existing theories only, ignoring all empirical knowledge about it, except the best currently known values of physical constants. An *ab initio* calculation in its purest form is free of parameters and includes all theoretical models of nature down to the level of quarks. However, it is impossible (at least so far) but also unnecessary to include quantum chromodynamics or other quantum field theories in the *ab initio* calculation of a solid.

Fortunately, physical theories on different scales decouple, and an entity studied by one theory can be treated as a black box by another theory one level higher in the structural hierarchy. For solids, this generally means we consider electrons and unstructured nuclei, interacting only through electromagnetism, and non-relativistic[2] quantum mechanics as the theoretical framework for *ab initio* calculations.

Such a pure form of *ab initio* calculation has never been seen in the wild, as a variety of simplifications and approximations on different levels are necessary to make *ab initio* calculations computationally feasible. We will focus on the most common and widespread approach for solids: *ab initio* density functional theory (DFT; see Chapter 2).

---

[2] In some cases relativistic effects have to be included even for solids, in particular when spin-orbit coupling effects play a role. This is especially important for the field of spintronics.

1.3 Computational Materials Science

The technological progress of our civilization has been a sequence of increasingly advanced and impactful material technologies. It is no surprise that we label entire eras, like the Stone, Bronze, Iron, and Silicon Age, by the materials that dominated them. Today, we are beginning to understand enough about materials to move away from traditional trial-and-error materials design towards the computer-aided development of highly optimized compounds.

Computational materials science seeks to advance our abilities to interpret experiments, and to understand and predict material properties. Since material properties are relevant over many length scales, ranging from the tiniest transistors to the longest bridges, computational materials science must span many orders of magnitude (see Fig. 1.3). Moreover, the goal of high-throughput materials design is obstructed by two major problems: First, predicting the most stable crystal structure of a given material is an intricate problem, and all other properties crucially depend on it. Second, the need for multi-parameter optimization, often involving quantum mechanics, is still very expensive.

Developing a unified multi-scale framework for materials design is a fascinating challenge. The development of many technologies could benefit from the computational optimization of the underlying materials, including batteries, photovoltaics, hydrogen storage, medical applications, automotive and aerospace, microelectronics, and many more. With this work we contribute a computational study of two different systems that is intended to help determine if they are suited for applications in novel material technologies.

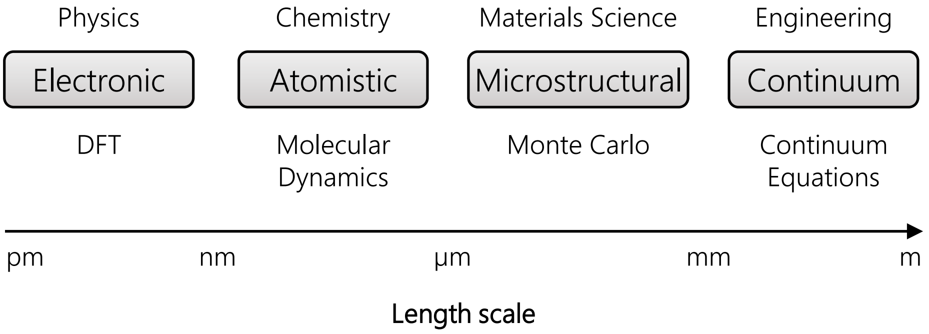

Figure 1.3 – Materials modelling on different length scales is governed by different scientific disciplines and computational methods. Developing a new framework for unified multi-scale modelling remains a challenge.

1.4 The Future of Computational Science

Computers are the result of scientific research, and they have aided scientific research ever since. This is a positive feedback cycle resulting in an exponential growth of computational power. That observation was first popularized by Gordon Moore at Fairchild Semiconductor in 1965 and is widely known as *Moore's law* [11]. It states that the complexity of integrated circuits, which is a measure of computational power, roughly doubles every 18 months. The physical limits of miniaturization are natural boundaries for the validity of Moore's law, but inevitably new technology will increase computational power in the same way miniaturization did—and Moore's law is likely to remain valid.

For computational science this means that raw power is not the limiting factor anymore. Instead, we will be constrained by our ability to envision and predict. We will face increasingly data-rich problems, such as real-time streaming of volumetric data, analyzing the signals of vast sensor arrays, simulating climate and weather, predicting the consequences of natural or man-made disasters, estimating the costs and benefits of large industrial projects, distinguishing causative and correlative relations in huge datasets, and many more.

Most of these problems are ill-posed and require significant interdisciplinary effort. There will soon be a need for "multi-scale intellectuals" and data scientists who try to answer questions outside of any given specialty and comfort zone. In politics, and for society in general, simulations already have great potential to influence high-leverage decisions. Making such predictions will become increasingly simple, but it is the consequences of those predictions that matter.

Future computational science must be approached from the viewpoint of the entire ecosystem, taking all factors and resources into account. Are we ready for exaflop systems processing massive datasets on the yottabyte scale, with a power consumption of megawatts and costs of $100 million per calculation?[3] We need to make sure that our algorithms are ready to exploit such expensive systems with short lifetimes.

Most important of all, we need to ensure that we learn something that is commensurate with the investment. If we solve those problems, the continuous increase in computational power will soon allow simulations at an unprecedented scale, laying the ground for new discoveries.

---

[3] These are actual numbers brought forward by the US National Nuclear Security Administration in 2012.

2

Density Functional Theory

Many-body systems are a fundamental challenge to theoretical physics. While quantum mechanics provides a sophisticated framework for the non-relativistic description of matter, there are only very few systems that can be solved exactly, like the hydrogen atom or the harmonic oscillator. Basically every system of three or more interacting particles escapes exact quantum mechanical treatment and needs to be caught with approximations. Those usually rely on separating the many-body wave function that describes the system as a whole into a combination of single-particle wave functions that describe either interacting particles or non-interacting particles in an effective potential. This is a reasonable approach for small systems, but it does not scale very well.

Macroscopic chunks of matter contain a number of electrons on the order of the Avogadro constant $N_\mathrm{A} \approx 6 \times 10^{23}$. With four coordinates assigned to each electron (three space coordinates and one spin coordinate), the many-body wave function Ψ of such a system depends on about 24×10^{23} variables—it is impossible to solve the corresponding many-body Schrödinger equation. Separating the problem into an astronomical number of single-particle wave functions is no less complex. Clearly, we need a different approach.

2.1 Solids as Many-Body Systems

Attempting to solve the Schrödinger equation for large systems kept many luminous minds busy for the best part of the last century. A prominent result of that endeavor is density functional theory (DFT), an elegant way of treating large interacting many-body systems such as solids. Built up only from electrons and about one hundred different kinds of atomic nuclei, solids form the vast variety of materials that surrounds us. Computational materials science makes use of the practical aspects of DFT to simulate solids, predict their properties, and motivate their use in technological applications. As we will see, three fundamental approximations to the exact quantum mechanical description of solids are necessary to reach that goal.

We start with a collection of electrons and point-like atomic nuclei in vacuum, subject to the Coulomb interaction only. The system is non-relativistic, there are no external electric or magnetic fields, and the total electric charge of the system is zero. We can then express the Hamiltonian $\hat{H}$ of this system as follows:

$$\hat{H} = \hat{T}_{\mathrm{N}} + \hat{T}_{\mathrm{e}} + \hat{V}_{\mathrm{eN}} + \hat{V}_{\mathrm{ee}} + \hat{V}_{\mathrm{NN}}. \tag{2.1}$$

The first two terms of that sum are the kinetic energy operators $\hat{T}$ for the nuclei (N) and the electrons (e), while the last three terms are the interaction potential operators $\hat{V}$ for the different combinations of particle types.

In computational materials science it is common to use atomic units to simplify the notation. We choose Hartree atomic units for the purposes of this exposition:[1]

$$\text{Hartree atomic units:} \qquad m_e = e = \hbar = \frac{1}{4\pi\epsilon_0} = 1. \tag{2.2}$$

We can now give explicit expressions for the different terms of the Hamiltonian in (2.1). Let Z_i denote the charge and M_i the mass of nucleus i, and let $\mathbf{R}_i$ and $\mathbf{r}_j$ be the positions of nucleus i and electron j, respectively. Then the components of the Hamiltonian read

---

[1] These units lead to formally dimensionless values. Quantities that do have a dimension in SI units are indicated by the formal unit symbol a.u. for “atomic units.”

$$\hat{T}_{\mathrm{N}} = -\frac{1}{2}\sum_i \frac{1}{M_i}\nabla^2_{\mathbf{R}_i}, \tag{2.3}$$

$$\hat{T}_{\mathrm{e}} = -\frac{1}{2}\sum_i \nabla^2_{\mathbf{r}_i}, \tag{2.4}$$

$$\hat{V}_{\mathrm{eN}} = -\sum_{i,j} \frac{Z_i}{\left|\mathbf{R}_i - \mathbf{r}_j\right|}, \tag{2.5}$$

$$\hat{V}_{\mathrm{ee}} = +\frac{1}{2}\sum_{i\neq j} \frac{1}{\left|\mathbf{r}_i - \mathbf{r}_j\right|}, \tag{2.6}$$

$$\hat{V}_{\mathrm{NN}} = +\frac{1}{2}\sum_{i\neq j} \frac{Z_i Z_j}{\left|\mathbf{R}_i - \mathbf{R}_j\right|}. \tag{2.7}$$

The observation that the proton mass is about 1836 times the electron mass motivates the first fundamental approximation: In typical solids, the electron dynamics happens on a scale four to five orders of magnitude faster than the dynamics of the nuclei. From the viewpoint of the electronic system the nuclei can thus be considered fixed. This is called the *Born-Oppenheimer approximation*. Applying that to the Hamiltonian in (2.1) we can drop the kinetic term $\hat{T}_{\mathrm{N}}$. Also, the interaction potential operator $\hat{V}_{\mathrm{NN}}$ reduces to a constant E_{NN} that we will ignore in the following.

The positions of the nuclei $\{\mathbf{R}_1,\ldots,\mathbf{R}_M\}$, with M being the total number of nuclei, enter the system properties as parameters. For example, they define the adiabatic total energy surface $E_{\mathrm{tot}}(\mathbf{R}_1,\ldots,\mathbf{R}_M)$. It is therefore possible to find the ideal atomic structure of a solid by minimizing its total energy with respect to these parameters. Similarly, all other system properties depend parametrically on the atomic positions. After this first approximation the Hamiltonian of a solid can be written as

$$\hat{H} = -\frac{1}{2}\sum_i \nabla^2_{\mathbf{r}_i} - \sum_{i,j} \frac{Z_i}{\left|\mathbf{R}_i - \mathbf{r}_j\right|} + \frac{1}{2}\sum_{i\neq j} \frac{1}{\left|\mathbf{r}_i - \mathbf{r}_j\right|}. \tag{2.8}$$

In principle, we can determine the many-body wave function of this system by solving the corresponding Schrödinger equation

$$i\frac{\partial}{\partial t}\Psi(\{\mathbf{r}_i\},t) = \hat{H}\Psi(\{\mathbf{r}_i\},t), \tag{2.9}$$

where $\{\mathbf{r}_i\}$ is a shorthand notation for the spatial coordinates $\mathbf{r}_1,\ldots,\mathbf{r}_m$ of all m electrons of the system.[2] Since the Hamiltonian $\hat{H}$ is not explicitly time-dependent we can assume the time evolution of the wave function as

$$\Psi(\{\mathbf{r}_i\},t) = \Psi(\{\mathbf{r}_i\})e^{-iEt} \tag{2.10}$$

and the problem reduces to the following time-independent Schrödinger equation:

$$\left(-\frac{1}{2}\sum_i \nabla^2_{\mathbf{r}_i} - \sum_{i,j}\frac{Z_i}{|\mathbf{R}_i - \mathbf{r}_j|} + \frac{1}{2}\sum_{i\neq j}\frac{1}{|\mathbf{r}_i - \mathbf{r}_j|}\right)\Psi(\{\mathbf{r}_i\}) = E\Psi(\{\mathbf{r}_i\}). \tag{2.11}$$

The many-body wave function $\Psi(\{\mathbf{r}_i\})$ is a complex, scalar function in a multidimensional configuration space that is very difficult to calculate in general. Computational methods focussing on the wave function give excellent results only for small molecules. In order to reach "chemical accuracy" (that means accurate values for chemical bond lengths and cohesive energies) these methods are limited to systems with a number of chemically active electrons on the order of 10. For larger systems, wave function centered methods encounter a forbidding *exponential wall* of computational and storage cost.

In fact, Walter Kohn—Nobel laureate and one of the founding fathers of modern DFT—argues that for systems with more than, say, 1000 electrons the many-body wave function is not a legitimate scientific concept anymore. Illegitimacy in this context means that such a wave function cannot be calculated with sufficient accuracy, nor can it be recorded for later retrieval in its entirety. This so called *van Vleck catastrophe* is discussed in detail in Walter Kohn's Nobel lecture [12].

The search for a more manageable quantity to describe large many-body systems began in 1927, just one year after Erwin Schrödinger had published his famous equation [13–16], and brought forth Thomas-Fermi density functional theory [17, 18], which was later modified by Dirac [19]. Indeed, it was the first attempt to express the energy of many-body systems as a *functional of the density* (hence the name), a real and scalar quantity in three-dimensional real space.

---

[2] For the moment we do not consider the electron spin, as it has no relevance for the formal derivation of density functional theory other than enforcing a fermionic wave function that is antisymmetric under exchange of spatial coordinates.

2.2 Thomas-Fermi-Dirac Theory

The total energy of the homogeneous electron gas is a function of the electron density, which compeletely specifies the system. The basic idea behind Thomas-Fermi-Dirac theory (TFD) is to apply concepts of the homogeneous electron gas to inhomogeneous systems. In such systems the electron density $n(\mathbf{r})$ is a spatially varying quantity, and the components of the total energy of a system can be expressed as *functionals* of it. Enrico Fermi and Llewellyn Thomas[3] independently derived a functional expression for the total energy of an inhomogeneous many-body system [17, 18]. Their original 1927 model did not include correlation or exchange, but Paul Dirac amended it in 1930 by adding an expression for exchange [19]:

$$E_{\mathrm{TFD}}[n(\mathbf{r})] = T_{\mathrm{e}}[n(\mathbf{r})] + E_{\mathrm{eN}}[n(\mathbf{r})] + E_{\mathrm{ee}}[n(\mathbf{r})] + E_{\mathrm{x}}[n(\mathbf{r})]. \tag{2.12}$$

The component functionals are the kinetic energy of the electrons T_{e}, the interaction energy of electrons and nuclei E_{eN}, the interaction energy of the electron density E_{ee} (the *Hartree energy*), and the *Slater-Dirac exchange energy* E_{x}. They are explicitly given by

$$T_{\mathrm{e}}[n(\mathbf{r})] = \frac{3}{10}(3\pi^2)^{\frac{2}{3}} \int \mathrm{d}\mathbf{r}\, n(\mathbf{r})^{\frac{5}{3}}, \tag{2.13}$$

$$E_{\mathrm{eN}}[n(\mathbf{r})] = \int \mathrm{d}\mathbf{r}\, v_{\mathrm{ext}}(\mathbf{r})\, n(\mathbf{r}), \tag{2.14}$$

$$E_{\mathrm{ee}}[n(\mathbf{r})] = \frac{1}{2}\int \mathrm{d}\mathbf{r}\,\mathrm{d}\mathbf{r}'\, \frac{n(\mathbf{r})\, n(\mathbf{r}')}{|\mathbf{r}-\mathbf{r}'|}, \tag{2.15}$$

$$E_{\mathrm{x}}[n(\mathbf{r})] = -\frac{3}{4}\left(\frac{3}{\pi}\right)^{\frac{1}{3}} \int \mathrm{d}\mathbf{r}\, n(\mathbf{r})^{\frac{4}{3}}. \tag{2.16}$$

Here, the term (2.14) includes the *external potential* $v_{\mathrm{ext}}(\mathbf{r})$ created by the nuclei or an arbitrarily distributed background charge. To ensure self-consistency of the density $n(\mathbf{r})$ we need to impose the constraint of a constant total number of electrons N:

---

[3] Llewellyn Thomas is said to have abandoned physics later in his life, bewildered by the intricacies of quantum mechanics. He turned to computer science instead.

$$\int \mathrm{d}\mathbf{r}\, n(\mathbf{r}) = N. \tag{2.17}$$

This optimization problem can be solved with the method of Lagrange multipliers. The stationary solutions of the corresponding Lagrange functional with the constant Lagrange multiplier μ have to fulfill

$$\frac{\delta}{\delta n(\mathbf{r})}\left\{E_{\mathrm{TFD}}[n(\mathbf{r})] - \mu\left(\int \mathrm{d}\mathbf{r}\, n(\mathbf{r}) - N\right)\right\} = 0, \tag{2.18}$$

which leads to the *Thomas-Fermi equation*

$$\frac{1}{2}(3\pi^2)^{\frac{2}{3}}\, n(\mathbf{r})^{\frac{2}{3}} + \int \mathrm{d}\mathbf{r}'\, \frac{n(\mathbf{r}')}{|\mathbf{r}-\mathbf{r}'|} - \left(\frac{3}{\pi}\right)^{\frac{1}{3}} n(\mathbf{r})^{\frac{1}{3}} = \mu - v_{\mathrm{ext}}(\mathbf{r}). \tag{2.19}$$

Given an external potential $v_{\mathrm{ext}}(\mathbf{r})$, this equation can be solved directly for the ground state density $n(\mathbf{r})$.

In general, Thomas-Fermi-Dirac theory is too inaccurate for most applications. Crudely approximating the kinetic energy and the exchange interaction, neglecting electron correlation altogether, it fails to predict chemical bonding and misses essential physics. Nonetheless, it is considered as the predecessor to modern density functional theory.

From equation (2.19) we see that the electron density $n(\mathbf{r})$ uniquely determines the external potential $v_{\mathrm{ext}}(\mathbf{r})$ up to a constant μ. This observation inspired Pierre Hohenberg and Walter Kohn to generalize that idea in their famous Hohenberg-Kohn theorems.

2.3 The Hohenberg-Kohn Theorems

The central tenet of density functional theory is that a many-particle system is completely and exactly specified by its particle density. While Thomas-Fermi-Dirac theory hinted at it early on, it took a few more decades for that idea to mature. Eventually, it culminated in the formulation of the Hohenberg-Kohn theorems in 1964 [20].

Theorem I

For any system of interacting particles in an external potential $v_{\mathrm{ext}}(\mathbf{r})$*, the ground state particle density* $n_0(\mathbf{r})$ *uniquely determines the external potential* $v_{\mathrm{ext}}(\mathbf{r})$ *up to a constant.*

Given the ground state density, the external potential and thus the Hamiltonian of the system are fully determined, except for a constant energy shift. This means that also the many-body wave functions for the ground state and for all excited states are determined. Therefore, *all properties of the system* are completely determined by the ground state density, but how do we obtain it?

Theorem II

For any system of interacting particles in an external potential $v_{\mathrm{ext}}(\mathbf{r})$*, there exists a universal density functional for the total energy* $E_{\mathrm{tot}}[n(\mathbf{r})]$ *whose global minimum value is the exact ground state energy* E_0 *at the exact ground state density* $n_0(\mathbf{r})$*:* $E_0 = E_{\mathrm{tot}}[n_0(\mathbf{r})]$.

All this holds true both for systems with non-degenerate, but also with degenerate ground states, as Kohn showed in 1985 [21]. On the technical side, it should be noted that the considered densities $n(\mathbf{r})$ must be *v-representable*, meaning that they are "well-behaved" (continuous, differentiable), integrate to an integer $N > 0$, and correspond to some external potential $v_{\mathrm{ext}}(\mathbf{r})$. The v-representability of densities $n(\mathbf{r})$ is still a matter of ongoing research, and well-behaved densities that are not v-representable do exist [22], but these cases are rather factitious. Fortunately, the densities of practically relevant systems are all v-representable, and this possible limitation has never been an issue in the DFT community.

While the Hohenberg-Kohn theorems are surprisingly simple to prove, their implications are tremendous: All the information that can be derived from the Hamiltonian by the solution of the Schrödinger equation is implicitly contained in the ground state density! The density is presented as a quantity of extraordinary richness, and the theorems point in the right direction as to the derivation of the density for arbitrary systems. However, we still lack a recipe for constructing the functional $E_{\mathrm{tot}}[n(\mathbf{r})]$ to obtain the ground state density n_0.

Theorem I states that all system properties, such as all partial energies, can be expressed as a functional of the density $n(\mathbf{r})$. Therefore the Hohenberg-Kohn (HK) total energy functional can be cast into the form

$$E_{\text{tot}}^{\text{HK}}[n(\mathbf{r})] = T[n(\mathbf{r})] + E_{\text{int}}[n(\mathbf{r})] + \int d\mathbf{r}\, v_{\text{ext}}(\mathbf{r}) n(\mathbf{r}), \tag{2.20}$$

but the exact expressions for the interacting kinetic energy functional $T[n(\mathbf{r})]$ and the interaction energy functional $E_{\text{int}}[n(\mathbf{r})]$ are unknown. At this point, Hohenberg-Kohn density functional theory is merely an exact reformulation of the many-body Schrödinger equation from the viewpoint of the particle density. It would be of little practical use if it were not for the formalism introduced by Walter Kohn and Lu Sham in 1965 [23], which enables us to find approximate total energy functionals to replace Eq. (2.20).

2.4 The Kohn-Sham Formalism

The basic idea of the Kohn-Sham formalism is to replace the original interacting many-body system with a supplementary system of independent particles and interacting density that has the same ground state density as the original system. This assumes the existence of such a supplementary system for each many-body system we consider—a property called *non-interacting-v-representability*. No rigorous proof has been given yet for its validity in real systems, but decades of experience suggest that it is an assumption we are safe to make [24].

For the sake of simplicity we require that the particles of the supplementary system move in a *local*, spin-dependent effective potential $v_{\text{eff}}^{\sigma}(\mathbf{r})$, so that the effective single-particle Hamiltonian reads

$$\hat{H}_{\text{eff}}^{\sigma} = -\frac{1}{2}\nabla^2 + v_{\text{eff}}^{\sigma}(\mathbf{r}). \tag{2.21}$$

We consider a system of $N = N^{\uparrow} + N^{\downarrow}$ electrons (the arrows $\sigma = \uparrow, \downarrow$ indicate spin-up and spin-down electrons) that can be described by the above Hamiltonian. To account for the Pauli exclusion principle we assume that in the ground state each orbital $\psi_i^{\sigma}(\mathbf{r})$ of the N lowest energy eigenvalues ε_i^{σ} is occupied with one electron. The density $n(\mathbf{r}) = n^{\uparrow}(\mathbf{r}) + n^{\downarrow}(\mathbf{r})$ of the supplementary system is thus given by

$$n(\mathbf{r}) = \sum_{\sigma} \sum_{i=1}^{N^\sigma} \psi_i^\sigma(\mathbf{r})\, \psi_i^{\sigma *}(\mathbf{r}). \tag{2.22}$$

The kinetic energy T_s of the independent particles can be expressed as

$$T_s[\{\psi_i^\sigma(\mathbf{r})\}] = -\frac{1}{2} \sum_{\sigma} \sum_{i=1}^{N^\sigma} \int \mathrm{d}\mathbf{r}\, \psi_i^{\sigma *}(\mathbf{r}) \left(\nabla^2 \psi_i^\sigma(\mathbf{r})\right), \tag{2.23}$$

which is an explicit functional of the orbitals $\psi_i^\sigma(\mathbf{r})$. However, Theorem I of Section 2.3 tells us that it can also be viewed as a density functional $T_s[n(\mathbf{r})]$ (in fact, it *must* be one). The interaction of the electron density with itself is described by the Hartree energy

$$E_{\mathrm{Hartree}}[n(\mathbf{r})] = \frac{1}{2} \int \mathrm{d}\mathbf{r}\, \mathrm{d}\mathbf{r}'\, \frac{n(\mathbf{r})\, n(\mathbf{r}')}{|\mathbf{r} - \mathbf{r}'|}. \tag{2.24}$$

Note that the above terms for the kinetic energy and the Hartree energy do not include exchange or correlation. The brilliance of the Kohn-Sham approach is to separate out all effects of exchange and correlation into an exchange-correlation functional $E_{\mathrm{xc}}[n(\mathbf{r})]$, for which we can find reasonable approximations—all other terms are exactly known. We can now rewrite the Hohenberg-Kohn functional (2.20) to obtain the Kohn-Sham total energy functional:

$$E_{\mathrm{tot}}^{\mathrm{KS}}[n(\mathbf{r})] = T_s[n(\mathbf{r})] + \int \mathrm{d}\mathbf{r}\, v_{\mathrm{ext}}(\mathbf{r})\, n(\mathbf{r}) + E_{\mathrm{Hartree}}[n(\mathbf{r})] + E_{\mathrm{xc}}[n(\mathbf{r})]. \tag{2.25}$$

Here, $v_{\mathrm{ext}}(\mathbf{r})$ is again the external potential of the nuclei, whose interaction energy E_{NN} enters as a constant that can be neglected. To illustrate the significance of the exchange-correlation energy functional $E_{\mathrm{xc}}[n(\mathbf{r})]$ we write it as

$$E_{\mathrm{xc}}[n(\mathbf{r})] = T[n(\mathbf{r})] - T_s[n(\mathbf{r})] + E_{\mathrm{int}}[n(\mathbf{r})] - E_{\mathrm{Hartree}}[n(\mathbf{r})]. \tag{2.26}$$

This shows that the exchange-correlation term incorporates the kinetic part of the correlation energy, as well as the effects of exchange and correlation of the electron-electron interaction that are not covered by the Hartree term. In that sense, the Kohn-Sham formalism can be viewed as the formal exactification of the Hartree method.

To obtain the ground state energy E_0 and the ground state density $n_0(\mathbf{r})$ for the effective Hamiltonian (2.21), which we assumed to be an equivalent description of the original interacting many-body system, we minimize the Kohn-Sham functional (2.25) subject to the constraint of orthonormal orbitals

$$\int \mathrm{d}\mathbf{r}\, \psi_i^\sigma(\mathbf{r})\, \psi_j^{\sigma *}(\mathbf{r}) = \delta_{i,j}. \tag{2.27}$$

Using the method of Lagrange multipliers we obtain the variational equation

$$\frac{\delta}{\delta \psi_i^{\sigma *}(\mathbf{r})} \left\{ T_s[\{\psi_i^\sigma(\mathbf{r})\}] + v_{\mathrm{eff}}^\sigma(\mathbf{r})\, \delta n(\mathbf{r},\sigma) - \varepsilon_i \left(\int \mathrm{d}\mathbf{r}\, \psi_i^\sigma(\mathbf{r})\, \psi_i^{\sigma *}(\mathbf{r}) - 1 \right) \right\} = 0, \tag{2.28}$$

where ε_i is a Lagrange multiplier and $v_{\mathrm{eff}}^\sigma(\mathbf{r})$ is the effective potential given by

$$v_{\mathrm{eff}}^\sigma(\mathbf{r}) = v_{\mathrm{ext}}(\mathbf{r}) + \frac{\delta E_{\mathrm{Hartree}}[n(\mathbf{r})]}{\delta n(\mathbf{r},\sigma)} + \frac{\delta E_{\mathrm{xc}}[n(\mathbf{r},\sigma)]}{\delta n(\mathbf{r},\sigma)} \tag{2.29}$$

$$= v_{\mathrm{ext}}(\mathbf{r}) + v_{\mathrm{Hartree}}(\mathbf{r}) + v_{\mathrm{xc}}^\sigma(\mathbf{r}). \tag{2.30}$$

From Eqs. (2.22) and (2.23) we obtain

$$\frac{\delta n(\mathbf{r},\sigma)}{\delta \psi_i^{\sigma *}(\mathbf{r})} = \psi_i^\sigma(\mathbf{r}) \qquad \text{and} \tag{2.31}$$

$$\frac{\delta T_s[\{\psi_i^\sigma(\mathbf{r})\}]}{\delta \psi_i^{\sigma *}(\mathbf{r})} = -\frac{1}{2}\nabla^2 \psi_i^\sigma(\mathbf{r}), \tag{2.32}$$

which we insert into (2.28). This yields

$$\left(-\frac{1}{2}\nabla^2 + v_{\mathrm{eff}}^\sigma(\mathbf{r}) \right) \psi_i^\sigma(\mathbf{r}) = \varepsilon_i \psi_i^\sigma(\mathbf{r}), \tag{2.33}$$

which is a Schrödinger-like single-particle equation for an effective Hamiltonian that looks exactly like (2.21). This leads to the following conclusion:

Kohn-Sham Formalism

The ground state of any system of interacting particles in an external potential $v_{\mathrm{ext}}(\mathbf{r})$ *is equivalent to the ground state of a system of non-interacting quasiparticles* $\psi_i^\sigma(\mathbf{r})$ *of energy* ε_i^σ *in an effective Kohn-Sham potential* $v_{\mathrm{KS}}^\sigma(\mathbf{r})$. *The solutions of the set of Schrödinger-like single-particle Kohn-Sham equations*

$$\hat{H}_{\mathrm{KS}}^\sigma \psi_i^\sigma(\mathbf{r}) = \left(-\frac{1}{2}\nabla^2 + v_{\mathrm{KS}}^\sigma(\mathbf{r})\right)\psi_i^\sigma(\mathbf{r}) = \varepsilon_i^\sigma \psi_i^\sigma(\mathbf{r}) \tag{2.34}$$

describe the ground state density $n_0(\mathbf{r})$ *according to (2.22). The effective potential* $v_{\mathrm{KS}}^\sigma(\mathbf{r})$ *is given by*

$$v_{\mathrm{KS}}^\sigma(\mathbf{r}) = v_{\mathrm{ext}}(\mathbf{r}) + v_{\mathrm{Hartree}}(\mathbf{r}) + v_{\mathrm{xc}}^\sigma(\mathbf{r}), \tag{2.35}$$

where $v_{\mathrm{xc}}^\sigma(\mathbf{r}) = \frac{\delta E_{\mathrm{xc}}[n(\mathbf{r},\sigma)]}{\delta n(\mathbf{r},\sigma)}$ *is the exchange-correlation potential, which contains all exchange and correlation effects for which the exact analytical form is unknown. In practice one works with approximate terms for the exchange-correlation energy* $E_{\mathrm{xc}}[n(\mathbf{r},\sigma)]$, *whose design has become its own field of research.*

It is important to note that neither the Kohn-Sham orbitals ψ_i^σ nor the energies ε_i^σ have any physical meaning. The only connection to the real, physical world is through Eq. (2.22) and the fact that the highest occupied state ε_i^σ, relative to the vacuum, equals the first ionization energy of the system. Other than that, the ε_i^σ are just Lagrange multipliers and the ψ_i^σ are quasiparticles that by construction reproduce the ground state density $n_0(\mathbf{r})$ of the original system. It is the ground state density that connects these quantities, which have a well-defined meaning only within the Kohn-Sham theory, to all other physical properties of the system.

Unfortunately, the detour via the Kohn-Sham orbitals is necessary to obtain the ground state density. It is entirely possible that there is a practical way to derive the density directly from the Hamiltonian, but it has not been found yet. Nonetheless, the Kohn-Sham formalism and the Hohenberg-Kohn theorems provide an exact, density-centered reformulation of the interacting many-body problem with profound consequences.

First, the Hohenberg-Kohn formulation of DFT replaces the virtually unsolvable problem of the many-body Schrödinger equation with the minimization of a density functional of the energy. Second, the Kohn-Sham formalism shows that we can minimize that functional by solving a set of independent single-particle equations involving an effective potential. That potential in turn is structured such that all terms whose exact analytical form is unknown are separated out into a local or nearly local exchange-correlation potential for which we can find practical approximations. It is this reformulation of the original problem on many levels that makes the numerical treatment of interacting many-body systems feasible.

2.5 Exchange-Correlation Functionals

The pivotal entity of density functional theory is the exchange-correlation functional $E_{\mathrm{xc}}[n(\mathbf{r})]$, whose existence is guaranteed by the Hohenberg-Kohn theorems. Any DFT calculation is only as good as the approximation it uses for that functional. The growing success of DFT over the last decades was nurtured by rapidly advancing computational prowess and the development of sufficiently accurate and versatile approximations to the exact exchange-correlation functional. While the Born-Oppenheimer approximation was the first fundamental approximation to the exact solid state Hamiltonian on our way towards a numerical treatment, the approximation of the exchange-correlation energy functional in DFT is the second one.

Nowadays, a vast zoo of functionals is available for all kinds of applications and classes of materials. Each functional has its idiosyncrasies, and some are applicable to a wide range of materials, while others should only be used for the special cases in which they excel. Exchange-correlation functionals can be classified by their locality properties, the amount and type of information they take into account, their degree of empiricism, and the constraints they satisfy.

There are two basic approaches to constructing an exchange-correlation functional: *nonempirical constraint satisfaction* and *semiempirical fitting* [25]. The first approach tries to construct parameter-free (except for fundamental constants) functionals that conform to formal properties of the exact exchange-correlation energy, such as scaling laws and asymptotic behavior. The second approach tends to disregard those formal constraints and fits the functionals to large empirical datasets gathered from experiments or accurate many-body calculations.

Nonempirical constraint satisfaction is a scientifically sound, prescriptive way to construct a hierarchy of exchange-correlation functionals with systematically increasing accuracy. The resulting functionals are universal by design and can be applied to a wide range of materials. In contrast, semiempirical functionals are descriptive. They typically involve many empirical parameters and produce accurate results only for systems not too different from the ones used for fitting the functionals. Many such functionals violate the formal constraints imposed by the exact exchange-correlation energy and fail to correctly describe even the one case where they could be exact: the homogeneous electron gas.

Semiempirical functionals are especially popular in quantum chemistry, which deals with molecular, localized systems, while solid state physics deals with extended, periodic systems, which require more universal, nonempirical functionals. This has caused many a controversy over which type of functional should be favored. In the solid state DFT community, philosophical and practical preference is given to nonempirical functionals.

John Perdew illustrated the classification of nonempirical functionals with his *Jacob's Ladder*[4] of exchange-correlation functionals [26] that leads from the inaccurate "Hartree world" to the "heaven of chemical accuracy"[5] (see Fig. 2.1). Users of DFT can ascend or descend along its rungs depending on their accuracy needs and the computational price they are willing to pay.

Climbing the ladder, the accuracy of the functionals increases with each rung. So does the computational cost and the conceptual complexity involved. Just like Russian matryoshka dolls, the functionals on each rung encompass the functionals on all lower rungs. By taking more information into account with each rung, more formal constraints imposed by the exact exchange-correlation energy can be satisfied. This produces a cadence of nonempirical functionals with systematically increasing complexity, accuracy and nonlocality.

The simplest approximation (the first rung) is to assume that the effects of exchange and correlation are purely local and can be described by the exchange-correlation energy of a homogeneous electron gas with a specific density. This is called the *local spin density approximation* (LSDA) [23]:

$$E_{\mathrm{xc}}^{\mathrm{LSDA}}[n(\mathbf{r},\sigma)] = \int \mathrm{d}\mathbf{r}\, n(\mathbf{r},\sigma)\, \epsilon_{\mathrm{xc}}^{\mathrm{hom}}\big(n(\mathbf{r},\sigma)\big). \tag{2.36}$$

---

[4] In Christian mythology, Jacob betrayed his older brother Esau of his birthright. During his escape, Jacob dreams of a ladder from earth to heaven, on which angels are ascending and descending.

[5] Chemical accuracy means that we can accurately describe the rates of chemical reactions. This translates to an energy error on the order of $\Delta E \lessapprox 1\,\frac{\mathrm{kcal}}{\mathrm{mol}} = 0.0434\,\mathrm{eV}$.

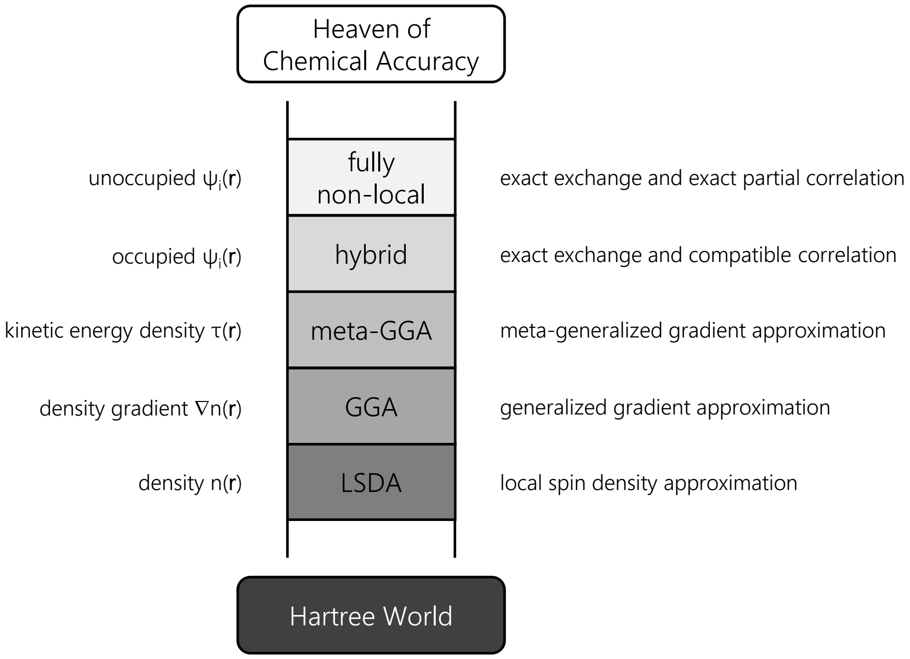

Figure 2.1 – (Adapted from [25]) The Jacob's Ladder of exchange-correlation functional approximations (after John Perdew). With each rung, additional ingredients (given on the left) are taken into account, which leads to an increase in accuracy, complexity, and computational cost.

Here, $\epsilon_{\mathrm{xc}}^{\mathrm{hom}}\big(n(\mathbf{r},\sigma)\big)$ is the exchange-correlation energy per particle of a homogeneous electron gas of density $n(\mathbf{r},\sigma)$. The spin quantization axis is assumed to be the same over the whole space.

LSDA assumes that a solid can locally be described by a homogeneous electron gas, which turns out to be a remarkably good approximation in many cases, even for solids with rapid electron density variations. This is because LSDA inherits the exact properties of the homogeneous electron gas and satisfies many of the general constraints on the exchange-correlation energy. Owing to its reasonable description of solids without long-range correlation effects, LSDA is still a widely used functional in solid state DFT. However, although it produces reasonably accurate bond lengths, it is less useful for molecular systems as it greatly overestimates binding energies.

This flaw can be mitigated by taking not only the local density, but also the local density gradient into account (second rung of the ladder). This requires knowledge of the density in a single point of space and in an infinitesimal region around that point, resulting in a class of semilocal functionals collectively called *generalized gradient approximation* (GGA) [27–29]. All GGA exchange-correlation energy functionals have the general form

$$E_{\mathrm{xc}}^{\mathrm{GGA}}[n(\mathbf{r},\sigma)] = \int \mathrm{d}\mathbf{r}\, n(\mathbf{r})\, \epsilon_{\mathrm{xc}}^{\mathrm{GGA}}\big(n(\mathbf{r},\sigma), \nabla n(\mathbf{r},\sigma)\big), \tag{2.37}$$

where the exchange-correlation energy per particle $\epsilon_{\mathrm{xc}}^{\mathrm{GGA}}$ depends on the spin-resolved density and density gradient. Naively one would think that for slowly varying densities the simple second-order gradient expansion (GE2),

$$E_{\mathrm{xc}}^{\mathrm{GE2}}[n_\uparrow, n_\downarrow] = \int \mathrm{d}\mathbf{r} \left[n\epsilon_{\mathrm{xc}}^{\mathrm{hom}}(n_\uparrow, n_\downarrow) + \sum_{\sigma,\sigma'} C_{\mathrm{xc}}^{\sigma\sigma'}(n_\uparrow, n_\downarrow) \frac{\nabla n_\sigma \cdot \nabla n_{\sigma'}}{n_\sigma^{2/3}\, n_{\sigma'}^{2/3}} \right], \tag{2.38}$$

is an improvement over LSDA. However, that expression violates an exact sum rule and performs worse than LSDA for many realistic systems [30]. The inadequacy of GE2 demonstrates precisely why it is so important to satisfy the constraints imposed by the exact exchange-correlation energy. The widely used and recommended GGA of John Perdew, Kieron Burke, and Matthias Ernzerhof (PBE) [27] is entirely nonempirical and honors all constraints that can be satisfied on the second rung of the ladder. It was used for all calculations presented in this work.

Meta-GGAs form the third rung of the ladder and take the kinetic energy densities $\tau_\sigma(\mathbf{r})$ of all occupied Kohn-Sham orbitals into account, where

$$\tau_\sigma(\mathbf{r}) = \frac{1}{2} \sum_i^{\mathrm{occ.}} |\nabla \psi_i^\sigma(\mathbf{r})|^2. \tag{2.39}$$

The kinetic energy densities $\tau_\sigma(\mathbf{r})$ are implicit functionals of the density and allow for the satisfaction of more constraints than the Laplacians $\nabla^2 n_\sigma(\mathbf{r})$, which they contain in the limit of slowly varying density.

So far, there is only one nonempirical meta-GGA, developed by Tao, Perdew, Staroverov, and Scuseria (TPSS) [31], which is of the form

$$E_{\mathrm{xc}}^{\mathrm{TPSS}}[n(\mathbf{r},\sigma)] = \int \mathrm{d}\mathbf{r}\, n(\mathbf{r})\, \epsilon_{\mathrm{xc}}^{\mathrm{TPSS}}\big(n(\mathbf{r},\sigma), \nabla n(\mathbf{r},\sigma), \tau_\sigma(\mathbf{r})\big). \tag{2.40}$$

TPSS does not satisfy all possible rung-three constraints, but it easily keeps pace with semiempirical functionals and greatly improves on PBE when it comes to molecular atomization energies and solid surface energies (see [25] and references therein).

On the fourth rung of the ladder, the exact exchange energy density $\epsilon_x^\sigma(\mathbf{r})$, which is a fully non-local functional of the Kohn-Sham orbitals $\psi_i^\sigma(\mathbf{r})$, is added as an ingredient. Here we find hybrid functionals that mix some exact exchange into meta-GGA or GGA exchange-correlation [32], like

$$E_{\mathrm{xc}}^{\mathrm{hybrid}} = E_{\mathrm{xc}}^{\mathrm{(meta-)GGA}} + a\left(E_{\mathrm{x}}^{\mathrm{exact}} - E_{\mathrm{x}}^{\mathrm{(meta-)GGA}}\right), \tag{2.41}$$

where $0 \leq a \leq 1$ with an optimal choice of $a = 1/4$. Other rung-four functionals are hyper-GGAs, which use exact exchange and compatible correlation constructed from meta-GGA ingredients [26]. Compatible means that the correlation part must be fully non-local at least in the occupied Kohn-Sham orbitals, like the exact exchange part. Popular semiempirical functionals like B3LYP [28, 29] are found on this level, while comparable nonempirical functionals are in development [33].

The fifth and final rung comprises functionals that combine exact exchange with a partially summated perturbation expansion of the correlation [26]. They are fully non-local functionals of the occupied as well as the unoccupied Kohn-Sham orbitals. On this level, there are no functionals for general use yet.

2.6 Self-Consistency

Choosing a suitable approximation to the exchange-correlation functional is not enough to set up and solve the Kohn-Sham equations. In order to construct the effective potential $v_{\mathrm{KS}}^\sigma(\mathbf{r})$ of (2.35) we need the density $n(\mathbf{r})$, and to obtain the density we need to solve the Kohn-Sham equations. Only an iterative approach can break this circle and reach approximate self-consistency of the density (or the effective potential, which is equivalent).

This approach is called the *self-consistent field cycle* (SCF cycle) and is illustrated in Fig. 2.2. We start with an initial estimate of the input density, which is typically a superposition of the atomic densities of the system. From that we construct the effective potential and set up the Kohn-Sham equations. What follows is the computationally most expensive step of solving the Kohn-Sham equations for a given basis set (see Section 2.7) to obtain the Kohn-Sham orbitals and energies. A new output density can then be calculated from those orbitals according to (2.22). That output density is necessarily different from any estimated, non-self-consistent input density.

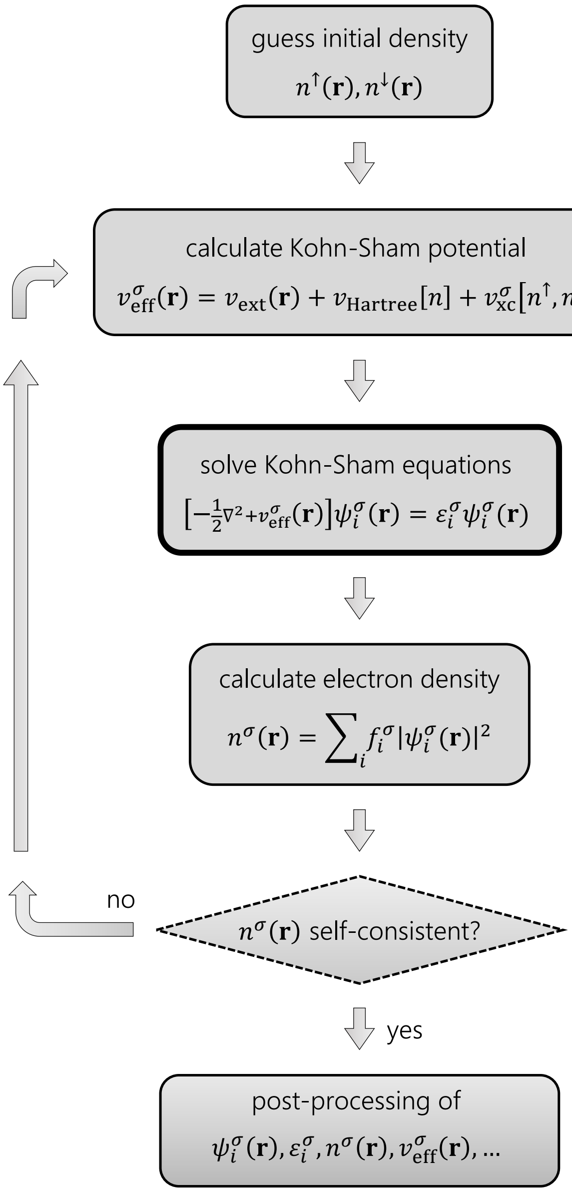

Figure 2.2 – Schematic prescription for an iterative, self-consistent solution of the Kohn-Sham equations.

The key to reaching self-consistency fast is to mix the output density with the input density of the same iteration in a clever way to generate the input density for the next iteration. This problem is more complicated than it seems. Simply using the output density as the new input density fails badly in many ways,[6] and linear schemes to update the density (*linear mixing*), such as

$$n_{i+1}^{\mathrm{in}} = n_i^{\mathrm{in}} + \alpha \left(n_i^{\mathrm{out}} - n_i^{\mathrm{in}} \right), \tag{2.42}$$

where i is the iteration index and $0 \leq \alpha \leq 1$ is the mixing factor, are very inefficient and not practical.

Methods involving the Jacobian or Hessian matrix prove to be more efficient than linear mixing. The family of *Broyden mixing* methods [36–41] take not only numerical details, but also algorithmic complexity into account, and update the inverse Jacobian successively with each iteration. Their efficiency has lead to the widespread use of Broyden-type mixing in contemporary Kohn-Sham solvers. Even more efficient and versatile, but also more complex mixing schemes are available in most DFT implementations today.

For real systems it is impossible to find the exact self-consistent density with numerical methods, but we can come arbitrarily close. Given an adequate mixing scheme, the input and output densities of the SCF cycle will differ less and less with each iteration, until finally a judiciously chosen convergence criterion is reached. The *density distance* d_n is such a criterion:

$$d_n = \frac{1}{\Omega_{\mathrm{cell}}} \int_{\Omega_{\mathrm{cell}}} \mathbf{dr} \left(n^{\mathrm{out}}(\mathbf{r}) - n^{\mathrm{in}}(\mathbf{r}) \right)^2 \leq d_n^{\mathrm{conv}}. \tag{2.43}$$

Here, Ω_{cell} is the real-space unit cell volume, and convergence is reached when at the end of an SCF iteration the density distance is smaller than d_n^{conv}. In a similar fashion, the difference of input and output values of many quantities derivable from the Kohn-Sham Hamiltonian can serve as a convergence criterion. Examples are the *charge distance* $d_Q = -ed_n$ (e is the positive elementary charge) or the total energy E_{tot} per unit cell.

In practice, the ground state density $n_0(\mathbf{r})$ itself is seldom the quantity of interest. Most DFT calculations involve finding the ground state density as the initial step, whose output is then processed to obtain other properties of the system, such as its electronic, mechanical, or optical properties. Post-processing a converged

---

[6] The reason for this is the behavior of the pre-self-consistent Kohn-Sham density near the minimum of the Kohn-Sham total energy functional, an excellent account of which is given by Refs. [34, 35].

density does not necessarily lead to an equally well converged quantity in each case. For this reason, any candid calculation must ensure the convergence of both density *and* target quantity.

2.7 The LAPW Basis Set

Solving the Kohn-Sham equations (2.34) on a computer necessarily means that we have to deal with limited resources. The Kohn-Sham orbitals ψ_i (the spin index is suppressed for simplicity) belong to a function space of infinite dimension, which is why they have to be projected on a finite basis set $\{\varphi_p\}$ of size P to be processed numerically:

$$\psi_i = \sum_{p=1}^{P} c_p^i \varphi_p. \tag{2.44}$$

Finding an appropriate basis set is the third fundamental approximation to solving the many-body Schrödinger equation of the solid-state Hamiltonian. An ideal basis set is both efficient (in other words, P is small) and describes the Kohn-Sham states accurately without being biased towards certain systems, which ensures general applicability. Given such a basis set, the solution of the Kohn-Sham equations (2.34) reduces to an eigenvalue problem of the form

$$\begin{bmatrix} \cdots & \cdots & \cdots \\ \vdots & \langle\varphi_m|\,\hat{H}_{\mathrm{KS}}\,|\varphi_n\rangle - \varepsilon_i\,\langle\varphi_m|\,\varphi_n\rangle & \vdots \\ \cdots & \cdots & \cdots \end{bmatrix} \begin{bmatrix} c_1^i \\ \vdots \\ c_P^i \end{bmatrix} = \begin{bmatrix} 0 \\ \vdots \\ 0 \end{bmatrix}. \tag{2.45}$$

Diagonalization of the Hamiltonian matrix $\left(\hat{H}_{\mathrm{KS}}\right)_{mn}$ leads to P eigenvalues ε_i and P eigenvectors $(c_1^i, \ldots, c_P^i)^{\mathrm{T}}$, which describe the Kohn-Sham orbitals ψ_i.

The most accurate basis set available today is the *Linearized Augmented Plane Wave* (LAPW) basis set [42, 43]. LAPW follows the classic *divide and conquer* approach, in that it divides the unit cell into spherical regions centered at the nuclei and the *interstitial* region between those spheres (see Fig. 2.3). Inside the spheres, the rapidly varying, atomic-like features of the wave function are represented by atomic orbitals. The smoothly varying wave functions in the interstitial are described by plane waves, which explains the term *augmented plane wave* (APW) [44, 45]. At the surfaces of the spheres, the atomic orbitals and the plane waves are made to match both in value and in slope.

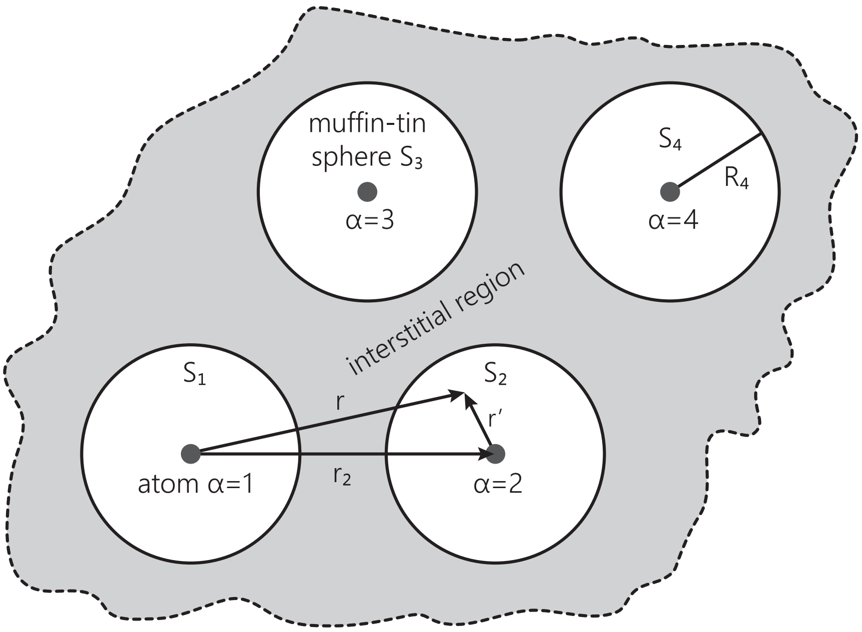

Figure 2.3 – Schematic view of how the LAPW method divides the unit cell into spheres around the nuclei and an interstitial region. The nomenclature used in Eq. (2.46) is also given. This two-dimensional projection inspired a rather picturesque name for a whole class of methods: *muffin tin* methods.

For a periodic crystal, the index i of the Kohn-Sham state ψ_i represents the quantum numbers n (the band index) and $\mathbf{k}$ (the crystal momentum, or a point in the first Brillouin zone), which label the solutions of the Hamiltonian $\hat{H}_{\mathrm{KS}}$ (again, the spin index σ is suppressed for simplicity of presentation). Typically, the first Brillouin zone of the system is sampled by a discrete k-point mesh. At each point $\mathbf{k}$ of that mesh, the solutions $\psi_{n\mathbf{k}}$ are determined for each band index n by solving (2.45) for the coefficients $c_p^{n\mathbf{k}}$. Note that advanced basis sets such as LAPW are k-dependent.

Let I be the interstitial region and S_α the sphere around atom α, then the functions of the LAPW basis set have the energy-independent form

$$\varphi_{\mathbf{K}}^{\mathbf{k}}(\mathbf{r}) = \begin{cases} \frac{1}{\sqrt{V}} e^{i(\mathbf{k}+\mathbf{K})\mathbf{r}} & \mathbf{r} \in I, \\ \sum\limits_{\ell,m} \left[A_{\ell m}^{\alpha,\mathbf{k}+\mathbf{K}} u_\ell^\alpha\left(r', E_\ell^\alpha\right) + B_{\ell m}^{\alpha,\mathbf{k}+\mathbf{K}} \dot{u}_\ell^\alpha\left(r', E_\ell^\alpha\right) \right] Y_m^\ell(\hat{\mathbf{r}}') & \mathbf{r} \in S_\alpha. \end{cases} \tag{2.46}$$

Here, $\mathbf{K}$ is a reciprocal lattice vector, and V is the volume of the unit cell. The position inside the sphere S_α is given by $\mathbf{r}' = \mathbf{r} - \mathbf{r}_\alpha$ (see Fig. 2.3), where $\hat{\mathbf{r}}'$ denotes a unit vector and $r' = |\mathbf{r}'|$. The summation indices ℓ and m are the orbital and the magnetic quantum number, respectively. The Y_m^ℓ are spherical harmonics, and the parameters $A_{\ell m}^{\alpha,\mathbf{k}+\mathbf{K}}$ and $B_{\ell m}^{\alpha,\mathbf{k}+\mathbf{K}}$ are determined by the condition that the basis function and its derivative be continuous at the boundaries of the spheres S_α. Furthermore, $u_\ell^\alpha\left(r', E_\ell^\alpha\right)$ is a solution of the radial Schrödinger equation for the free atom α with energy E_ℓ^α, which is an atom- and orbital-dependent linearization energy, whereas $\dot{u}_\ell^\alpha\left(r', E_\ell^\alpha\right)$ is its energy derivative.

If it were not for this linearization, the atomic orbital part of the augmented plane waves would be energy-dependent through $u_\ell^\alpha(r', E)$. This introduces additional computational complexity that renders the corresponding non-linear APW method, a predecessor of LAPW, impractical. The LAPW method replaces $u_\ell^\alpha(r', E)$ by a linear combination of $u_\ell^\alpha(r', E_{\text{lin}})$ and its energy derivative $\dot{u}_\ell^\alpha(r', E_{\text{lin}})$, evaluated at the linearization energy E_{lin}, which can be chosen atom- and orbital-dependent for greater accuracy. This leads to an efficient basis set suitable for describing electron states in an energy window ΔE around E_{lin}. The resulting wave functions are correct to first order in ΔE, while energies are correct to $(\Delta E)^2$.

The size P of the LAPW basis set is determined by a cutoff K_{max} for the reciprocal lattice vectors $\mathbf{K}$, as well as an upper limit ℓ_{max} for the orbital expansion. It can be shown that the overall accuracy of the LAPW basis set is determined by the quantity $R_\alpha^{\text{min}} K_{\text{max}}$ (or simply RK_{max}), which is the product of the smallest atomic sphere radius and K_{max}, the reciprocal lattice vector cutoff. Practical values for RK_{max} lie in the range of 7–9.

The *ab initio* code package WIEN2k [46–48], which has been used for most of the calculations presented in this work, implements a modern variant of the LAPW method.

2.8 Perspectives on DFT

Computational materials science has come a long way since Douglas Hartree and his father worked out the electronic structure of atoms with a desk calculator [49]. Hartree was not only a theoretical physicist, he also became a pioneer of computer science who built a differential analyzer and developed numerical methods. Both fields were as intertwined in his person as they are today, especially in computational materials science. Indeed, the theoretical foundations of density functional theory presented in this chapter are only half the story. Much of the success of DFT is rooted in its adequacy for computational treatment.

In their 1965 paper [23], Kohn and Sham presented the local density approximation to the exchange-correlation functional and emphasized that they "do not expect an accurate description of chemical binding." Luckily, they were wrong. DFT came to be the standard framework for a vast array of accurate numerical methods in quantum chemistry and solid state physics. More than 20,000 DFT-related publications appear each year.[7] In fact, the impact of DFT on electronic structure research was so strong that Walter Kohn and John Pople were awarded the 1998 Nobel prize in chemistry; Kohn for his development of density functional theory, and Pople for his work on wave function methods in computational chemistry. It was the first time the Nobel committee honored the development of numerical methods.

According to Walter Kohn [12], density functional theory has made two important contributions to the study of electronic structure. First, it greatly simplifies our view on the problem. By taking the vantage point of the electron density we are able to visualize and describe a many-body system in terms of a three-dimensional quantity in real space, rather than an abstract wave function in a high-dimensional Hilbert space. The second contribution is a practical one. DFT recasts the interacting many-body problem as a set of independent-particle equations with an easily approximable effective potential that contains all many-body effects.

Nowadays, DFT implementations are abundant. All the different exchange-correlation functionals, mixers, basis sets, integration techniques, and pseudopotentials result in countless combinations of methods, which may be compatible with each other or not. Therefore, in order to put DFT to fruitful use, it is essential to understand the quirks of each method and their intricate interplay.

---

[7] On April 18, 2014, Thomson Reuters' *Web of Science* returned 26,847 results for "density funtional theory" and the publication year 2013.

It is no surprise that early DFT was ridiculed by many quantum chemists and decried as a “dark art” by confused outsiders. Moreover, the apparent ease of use of many DFT implementations attracts many amateurs. Indeed, it is very easy to produce results with established DFT code packages, but it is just as easy to produce results completely void of physical content [50].

It takes insight, methodological skill, and, above all, experience to use a given DFT code not just as a “black box,” but as a sharp tool to predict material properties. Having said that, it is important to note that any DFT calculation should only be interpreted within the boundaries set by the method. In many cases, DFT calculations have to be regarded as model calculations for a given system, mostly because DFT also has limitations that have not been addressed so far.

Density functional theory is inherently a ground state theory. It does not capture electronic excited states, nor does it include any temperature-related phenomena, such as phonons in solids. Investigating excited states or finite-temperature phenomena on top of a pure DFT calculation invariably means extrapolating the theory to something it was not designed for. Although experience shows that this stretch is often justified—for example in this work—this should be kept in mind.

DFT also fails badly at the description of phenomena involving any kind of long-range correlation, such as van der Waals forces between atoms and molecules, or strongly correlated materials [51]. The reason for this is that most established exchange-correlation functionals model their correlation part as local or semilocal functionals of the density or other quantities, which is bound to misrepresent long-range correlation. An efficient, fully non-local treatment of correlation capturing such effects continues to be elusive.

3

Optical Properties of Solids

Our visual perception of the world is determined by the optical properties of the things that surround us. Using light to probe the properties of an object is a natural process for any animal equipped with a visual sense. However, being restricted by our anatomy and physiology, we can see only a narrow range of wavelengths and determine only macroscopic properties of an object, such as position, shape, color, luster, and surface roughness. It is the scientific study of optical properties that greatly extends our visual horizon.

Electromagnetic radiation is arguably the most versatile scientific tool, whose domain spans all relevant orders of magnitude. We can use it to study small-scale, microscopic properties such as the energy band structure of a solid, or measure the largest cosmic distances by using type Ia supernovae as standard candles [52]. The finiteness of the speed of light allows us to look back in time and study the era of inflation shortly after the big bang by analyzing fluctuations of intensity and polarization in the cosmic background radiation [53, 54].

Appreciating the richness of the scientific use of optics we focus on the optical properties of solids. This chapter outlines the connection between observable optical quantities and the microscopic properties of crystalline solids, and shows how those quantities can be obtained from *ab initio* calculations.

3.1 Interaction of Light and Matter

One of the fundamental questions of solid state optics is how the experimental observation of an optical quantity relates to the energy band structure of the solid. In general, there are two processes that contribute to an optical observable. On one hand, *intraband* processes are mediated by the electronic conduction of free charge carriers within the same energy band, which is relevant only in metallic solids. They can be described classically by the Drude model or by Boltzmann transport theory, or quantum mechanically by the density matrix formalism. On the other hand, *interband* transitions involve the absorption of a photon by an electron in an occupied state below the Fermi level, which then transitions to an unoccupied state above the Fermi level, thus involving two different energy bands. This is an intrinsically quantum mechanical process and needs to be described as such.

In practice it is common to restrict the analysis of intraband and interband processes to a small set of bands or to certain regions of the Brillouin zone that are responsible for dominant contributions to the optical quantity of interest. However, for *ab initio* calculations there is evidently no need to do so, as they are limited only by the efficiency and accuracy of their numerical methods and the available computing power. Irrelevant of the approach we choose, the collective effect of all intraband and interband processes is expressed by two equivalent, fundamental quantities: the dielectric function ε and the conductivity σ. They connect the microscopic interaction of light and matter to macroscopic observables such as reflectivity, absorption, or magneto-optical phenomena.

The interatomic distances in solids are on the order of 10^{-10} m. Since we are concerned with electromagnetic radiation in the near infrared, visible, and near ultraviolet range (which means wavelengths on the order of at least 10^{-8} m), it is justified to use Maxwell's equations for a macroscopic description of electromagnetic radiation in matter. Assuming a medium free of electric charges and using CGS-Gaussian units[1] we can express them as

$$\nabla \cdot \mathbf{D} = 0, \tag{3.1}$$

$$\nabla \cdot \mathbf{B} = 0, \tag{3.2}$$

$$\nabla \times \mathbf{H} = \frac{1}{c}\frac{\partial \mathbf{D}}{\partial t} + \frac{4\pi}{c}\mathbf{j}, \tag{3.3}$$

$$\nabla \times \mathbf{E} = -\frac{1}{c}\frac{\partial \mathbf{B}}{\partial t}, \tag{3.4}$$

---

[1] Although the use of non-SI units is generally discouraged, we employ CGS-Gaussian units for the sake of consistency with the calculation results presented later.

where c is the speed of light in vacuum. The electric displacement field **D**, the electric field **E**, the magnetic induction **B**, the magnetic field **H**, and the current density **j** are related by the material equations

$$\mathbf{D} = \varepsilon \cdot \mathbf{E}, \tag{3.5}$$

$$\mathbf{B} = \mu \cdot \mathbf{H}, \tag{3.6}$$

$$\mathbf{j} = \sigma \cdot \mathbf{E}. \tag{3.7}$$

For non-magnetic media, the dielectric function ε, the magnetic permeability μ, and the conductivity σ are complex and symmetric rank-2 tensors. Note that these equations capture only effects linear in **E** and **H**. To study non-linear optics one has to include terms of higher order. In the most general case of a medium inhomogeneous in space and time, Eq. (3.5) takes the form

$$\mathbf{D}(\mathbf{r}, t) = \int \mathrm{d}\mathbf{r}' \int \mathrm{d}t' \, \varepsilon(\mathbf{r} - \mathbf{r}'; t - t') \cdot \mathbf{E}(\mathbf{r}', t'), \tag{3.8}$$

where we assume the origin of the space and time coordinates to be irrelevant. Similar relations hold for the other two material equations. Note that all electromagnetic quantities involved here are in general complex.

Later we will describe monochromatic light in vacuum as an electric plane wave field with wave vector **k** and angular frequency ω. It is thus favorable to work with the material equations in reciprocal space. The electric field of light in an inhomogeneous medium can be expressed as a Fourier integral of the form

$$\mathbf{E}(\mathbf{r}, t) = \frac{1}{(2\pi)^4} \int \mathrm{d}\mathbf{k}' \int \mathrm{d}\omega' \, \mathbf{E}(\mathbf{k}', \omega') \, e^{i(\mathbf{k}' \cdot \mathbf{r} - \omega' t)}, \tag{3.9}$$

which reduces to a plane wave if $\mathbf{E}(\mathbf{k}', \omega') = (2\pi)^4 \mathbf{E}_0 \, \delta(\mathbf{k}' - \mathbf{k}) \, \delta(\omega' - \omega)$ for monochromatic light in vacuum:

$$\mathbf{E}(\mathbf{r}, t) = \mathbf{E}_0 \, e^{i(\mathbf{k} \cdot \mathbf{r} - \omega t)}. \tag{3.10}$$

The corresponding Fourier transformation of Eq. (3.8) leads to

$$\mathbf{D}(\mathbf{k}, \omega) = \varepsilon(\mathbf{k}, \omega) \cdot \mathbf{E}(\mathbf{k}, \omega). \tag{3.11}$$

Every medium is inhomogeneous on an atomic scale. However, from our previous observation that relevant wavelengths λ are much larger than any microscopic material length scales we conclude that the medium can be considered homogeneous. In fact, since $|\mathbf{k}| = 2\pi/\lambda$, we can work in the limit $\mathbf{k} \to 0$ and assume the reciprocal space quantities to depend only on the frequency ω.

It has been shown that the complex magnetic permeability tensor $\mu(\omega) = \mathbf{1}$ for optical frequencies, where $\mathbf{1}$ is the 3×3 unit matrix [55,56]. Since that is true even for metallic ferromagnets, we conclude that the interaction of electromagnetic radiation with matter at optical frequencies is dominated by the electric response. The complex tensor of the dielectric function $\varepsilon(\omega)$ and the complex optical conductivity[2] tensor $\sigma(\omega)$ are related by [57]

$$\varepsilon(\omega) = \mathbf{1} + \frac{4\pi i}{\omega}\sigma(\omega). \tag{3.12}$$

From this equation it follows that $\varepsilon(\omega)$ and $\sigma(\omega)$ are equivalent; they contain the same information. In fact, their real or imaginary parts alone contain the same information because they are related by Kramers-Kronig relations [58,59]. For the optical conductivity $\sigma(\omega)$ they read

$$\mathrm{Re}\left[\sigma_{\alpha\beta}(\omega)\right] = \frac{2}{\pi}\mathscr{P}\int_0^\infty \mathrm{d}\omega'\, \frac{\omega'}{\omega'^2 - \omega^2}\,\mathrm{Im}\left[\sigma_{\alpha\beta}(\omega')\right], \tag{3.13}$$

$$\mathrm{Im}\left[\sigma_{\alpha\beta}(\omega)\right] = -\frac{2}{\pi}\mathscr{P}\int_0^\infty \mathrm{d}\omega'\, \frac{\omega}{\omega'^2 - \omega^2}\,\mathrm{Re}\left[\sigma_{\alpha\beta}(\omega')\right], \tag{3.14}$$

where $\mathscr{P}$ denotes Cauchy's principal value and $\sigma_{\alpha\beta}(\omega)$ represents the $\alpha\beta$ component of $\sigma(\omega)$. Similar relations hold for $\varepsilon(\omega)$.

The Maxwell equations (3.1)–(3.4) together with the material equations (3.5)–(3.7) completely determine the propagation of light in a given medium. Thus, the consequence of Eqs. (3.12)–(3.14) is that either the real or the imaginary part of either $\varepsilon(\omega)$ or $\sigma(\omega)$ is sufficient to determine all macroscopic optical properties of the material at hand, which is exactly what we want. But how do we obtain $\varepsilon(\omega)$ or $\sigma(\omega)$ from the microscopic properties of the medium, such as its energy band structure?

---

[2] The term *optical conductivity* refers to the ac conductivity at optical frequencies.

Since we are interested in an *ab initio* description of optical material properties, the expressions used to calculate those quantities must be compatible with the numerical method used. The primary computational tool of this study, the DFT code package WIEN2k [47], implements the following random phase approximation formula for the imaginary part of $\varepsilon(\omega)$, which is compatible with the LAPW method [60]:

$$\begin{aligned}\mathrm{Im}\left[\varepsilon_{\alpha\beta}(\omega)\right] = &\frac{\hbar^2 e^2}{\pi m_e^2 \omega^2} \sum_{n \neq n'} \int \mathrm{d}\mathbf{k}\, \Pi^{\alpha}_{nn',\mathbf{k}} \Pi^{\beta}_{n'n,\mathbf{k}} \\ &\times \left[f(\epsilon_{n,\mathbf{k}}) - f(\epsilon_{n',\mathbf{k}})\right] \delta(\epsilon_{n',\mathbf{k}} - \epsilon_{n,\mathbf{k}} - \hbar\omega),\end{aligned} \tag{3.15}$$

where $\Pi^{\alpha}_{nn',\mathbf{k}} = \langle n',\mathbf{k}|\hat{p}_{\alpha}|n,\mathbf{k}\rangle$ is the transition matrix element of the α component of the momentum operator for a direct interband transition ($n \neq n'$) from the initial Kohn-Sham state $|n,\mathbf{k}\rangle$ with energy $\epsilon_{n,\mathbf{k}}$ into the final state $|n',\mathbf{k}\rangle$ with energy $\epsilon_{n',\mathbf{k}}$. The Fermi-Dirac distribution function evaluated at energy $\epsilon_{n,\mathbf{k}}$ is given by $f(\epsilon_{n,\mathbf{k}})$, and m_e denotes the electron mass.

Using Eq. (3.15) on top of a converged Kohn-Sham eigensystem obtained by a preceding *ab initio* DFT calculation, we can obtain $\varepsilon(\omega)$ and $\sigma(\omega)$ from the microscopic properties of the material. In the following we describe how those quantities influence the propagation of light in the medium and how we can calculate macroscopic optical properties from that. We again consider the plane wave given by Eq. (3.10) and define the refractive index $\mathbf{n} = c\mathbf{k}/\omega$ as the speed of light in vacuum divided by the phase velocity of light in the material. The light wave in the material is thus given by

$$\mathbf{E}(\mathbf{r},t) = \mathbf{E}_0 \cdot \exp\left[i\left(\frac{\omega}{c}\mathbf{n}\cdot\mathbf{r} - \omega t\right)\right]. \tag{3.16}$$

Combining that with the Maxwell equations and the material equations we arrive at the *Fresnel equation*

$$\left(\varepsilon(\omega) + \mathbf{n}_j \otimes \mathbf{n}_j - n_j^2 \mathbf{1}\right) \cdot \mathbf{E}_{0,j} = 0, \tag{3.17}$$

which in general has two solutions for the normalized eigenmodes $\mathbf{E}_{0,j}$ and the corresponding refractive indices $\mathbf{n}_j$ ($j = 1,2$). The dielectric tensor $\varepsilon(\omega)$ thus completely determines the propagation of light in the medium, and consequently all macroscopic optical quantities, such as the magneto-optical Kerr effect.

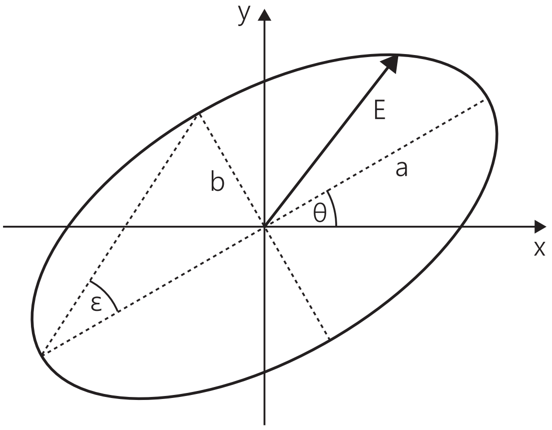

Figure 3.1 – Light that undergoes MOKE becomes elliptically polarized; the electric field vector $\mathbf{E}(\mathbf{r}, t)$ describes an ellipse. MOKE is quantitatively expressed by the Kerr rotation angle θ_K between the semimajor axis a of the ellipse and a given reference direction (x), and by the Kerr ellipticity angle ϵ_K, which represents the axis ratio b/a.

3.2 The Magneto-Optical Kerr Effect

When linearly polarized light is reflected from a magnetized medium it becomes elliptically polarized (see Fig. 3.1). This is called the *magneto-optical Kerr effect* (MOKE), after John Kerr, who discovered the effect in 1877 while experimenting with polarized light reflected from the poles of a magnet [61]. From then on MOKE has been developed into an essential tool of magnetism research.

MOKE allows for relatively simple experimental setups and provides a contact-free method of studying various properties of magnetic materials *in situ*. Among them are magnetic domains, which are directly observable using a Kerr microscope, and magnetization curves. MOKE was also used to study spin injection into semiconductors [62–65], which is of particular interest in semiconductor spintronics. Because of its high spatial, temporal, and in-depth resolution [66], MOKE can be used to study magnetization dynamics and buried magnetic layers. Those properties also make it an ideal readout technique for magneto-optical data storage devices [67], such as MiniDiscs, which were especially popular in Japan in the 1990s and early 2000s.

The origin of the MOKE ellipse can be understood from a simple classical picture. In Fig. 3.2, the incoming beam is linearly polarized along x. This causes the electrons in the medium to oscillate along the x direction. However, since the medium is magnetized along z, the electrons start to move on an elliptic orbit in the xy plane under the influence of the Lorentz force acting along y.

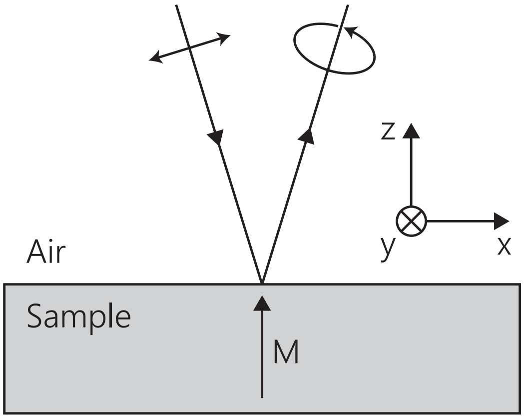

Figure 3.2 – Magneto-optical Kerr effect of a sample magnetized perpendicular to its surface, along with a definition of the coordinate system used in the text.

The emitted radiation is thus elliptically polarized. This argument is similar for media magnetized along x or y, which is why there are three basic MOKE configurations: *longitudinal, transverse,* and *polar* MOKE (see Fig. 3.3). This study deals only with polar MOKE (P-MOKE).

A more elaborate macroscopic picture involves decomposing the linearly polarized incoming beam into a left-handed circularly polarized and a right-handed circularly polarized beam, each being affected by a different complex refractive index. That means the beams experience different dispersion, which causes a phase shift and thus the rotation of the main polarization plane, and also different absorption, which causes the ellipticity. Below we will develop a quantitative theory of MOKE based on this macroscopic description.

The true microscopic origin of MOKE is of quantum mechanical nature and is related to an interplay of exchange splitting and spin-orbit coupling. Any material with an exchange-split band structure in the presence of spin-orbit coupling will exhibit a dielectric tensor that gives rise to magneto-optical effects. This suggests that MOKE can be used to study spin-orbit coupling effects in magnetized materials. By carefully choosing the probing wavelength it should even be possible to address specific interband transitions and probe the effective spin-orbit coupling fields of selected energy bands.

Together with the similar Faraday effect [68], which is measured in transmission instead of reflection, the Kerr effect is a founding member of a whole family of magneto-optical phenomena exploited in experimental magnetism research.

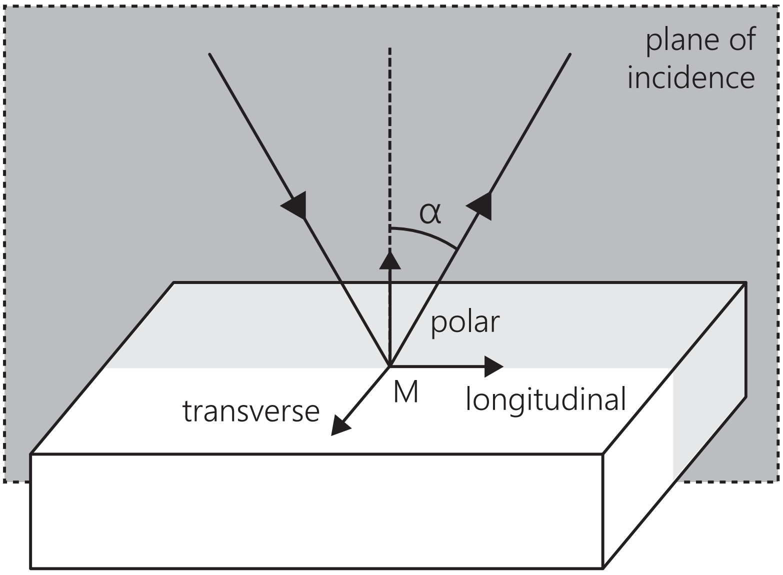

Figure 3.3 – The three basic configurations of MOKE. In this study we are concerned with polar MOKE at normal incidence ($\alpha = 0$).

3.3 Isotropic P-MOKE

We consider normal-incidence polar MOKE of a thin[3] film in the xy plane that is isotropic in that plane and magnetized along z. The presence of a magnetization $\mathbf{M}$ gives rise to off-diagonal components of the dielectric tensor that are at least linear (odd) in $\mathbf{M}$. Magneto-optical effects on the diagonal components are at least quadratic (even) in $\mathbf{M}$ and are neglected in the following discussion. The magnetization along z causes a tetragonal distortion of the structure, which is why the dielectric tensor component along z is different from those in the xy plane. Hence, the dielectric tensor takes the form[4] [56, 70]

$$\varepsilon = \begin{pmatrix} \varepsilon_{xx} & \varepsilon_{xy} & 0 \\ -\varepsilon_{xy} & \varepsilon_{xx} & 0 \\ 0 & 0 & \varepsilon_{zz} \end{pmatrix}. \tag{3.18}$$

The antisymmetry of the off-diagonal components ε_{xy} follows from the Onsager relations [55]. Reversing the magnetization of the system $\mathbf{M} \to -\mathbf{M}$ simply corresponds to a sign change $\varepsilon_{xy} \to -\varepsilon_{xy}$. Note that this tensor has C_∞ symmetry in

---

[3] Thin, yet thick enough to show no effects of reflection by the bottom surface. To include such effects, for example in multilayer structures, one has to follow different approaches, such as *Yeh's formalism* [69].

[4] The explicit dependence on ω is suppressed to simplify the notation.

the xy plane. Thus, changing the polarization direction of the linearly polarized incoming beam has no effect on the MOKE rotation or ellipticity. This is why we speak of *isotropic* P-MOKE.

First we solve the Fresnel equation to obtain the normalized eigenmodes and the associated refractive indices in the material. Inserting (3.18) into (3.17) and defining the vector of refractive indices as $\mathbf{n}_j = (0, 0, n_j)^\mathrm{T}$, we obtain

$$n_j^2 = \varepsilon_{xx} \pm i\varepsilon_{xy}, \tag{3.19}$$

$$\mathbf{E}_{0,j} = \frac{1}{\sqrt{2}} \begin{pmatrix} 1 \\ \pm i \end{pmatrix}, \tag{3.20}$$

where $j = 1, 2$. The normalized eigenmode $\mathbf{E}_{0,j}$ is expressed as a two-dimensional Jones vector [71] describing its polarization state.

The eigenmodes are thus left-handed circularly polarized and right-handed circularly polarized, each affected by a different complex refractive index. The difference in dispersion and absorption for the eigenmodes is directly given by the complex off-diagonal dielectric tensor component ε_{xy}.

In order to deduce the MOKE rotation and ellipticity angles, we have to compare the polarization state of the incoming partial beam $\mathbf{E}_j$ to that of the reflected beam $\mathbf{E}'_j$. The reflection is described by the complex reflection coefficient r_j defined by $\mathbf{E}'_j = r_j \cdot \mathbf{E}_j$, which is given by the Fresnel formula for normal incidence [72]:

$$r_j = \frac{n_j - 1}{n_j + 1}. \tag{3.21}$$

The coefficient r_j contains the information about the MOKE angles, and by writing $r_j = |r_j| \cdot e^{i\alpha_j}$ we find that

$$\frac{|r_2|}{|r_1|} e^{i(\alpha_2 - \alpha_1)} = \frac{1 + n_1}{1 - n_1} \frac{1 - n_2}{1 + n_2}. \tag{3.22}$$

The Kerr rotation angle θ_K is given by the phase difference of the normal modes in the material caused by the reflection,

$$\theta_K = \frac{1}{2}(\alpha_1 - \alpha_2), \tag{3.23}$$

while the Kerr ellipticity angle ϵ_K is the quotient of the minor and the major axis of the resulting polarization ellipse:

$$\tan \epsilon_K = \frac{|r_2| - |r_1|}{|r_2| + |r_1|}, \tag{3.24}$$

which can be rewritten as

$$\frac{|r_2|}{|r_1|} = \frac{1 + \tan \epsilon_K}{1 - \tan \epsilon_K}. \tag{3.25}$$

Inserting (3.23) and (3.25) into (3.22) we obtain the following exact expression for normal-incidence isotropic P-MOKE:

$$\frac{1 + \tan \epsilon_K}{1 - \tan \epsilon_K} e^{-2i\theta_K} = \frac{1 + n_1}{1 - n_1} \frac{1 - n_2}{1 + n_2}. \tag{3.26}$$

Since Kerr rotations and ellipticities are usually smaller than 1° [73], we can expand (3.26) in θ_K and ϵ_K. This yields the following approximation for the complex Kerr angle Φ_K:

$$\Phi_K = \theta_K + i\epsilon_K \approx i \frac{n_2 - n_1}{n_1 n_2 - 1} = \frac{-\varepsilon_{xy}}{(1 - \varepsilon_{xx})\sqrt{\varepsilon_{xx}}}, \tag{3.27}$$

where we have used (3.19) to obtain an expression in terms of the components of the dielectric tensor ε.

Equivalently, using (3.12), one can express Φ_K in terms of the optical conductivity:

$$\Phi_K = \theta_K + i\epsilon_K \approx \frac{\sigma_{xy}}{\sigma_{xx}\sqrt{1 + \frac{4\pi i}{\omega}\sigma_{xx}}}. \tag{3.28}$$

Note that the complex Kerr angle Φ_K, just like all other quantities derived from $\varepsilon(\omega)$ or $\sigma(\omega)$, is dependent on the angular frequency ω of the incoming beam. The above expressions are valid for the vast majority of isotropic materials with a dielectric tensor of the form (3.18) in the given configuration. In the following we will generalize the theory to anisotropic materials.

3.4 Anisotropic P-MOKE

Now we consider a sample in the same configuration (normal incidence, magnetization along z) that is anisotropic in the xy plane. As we will see, this is the case for the Fe/GaAs(001) heterostructure, which is one of the subjects of this study. Given the anisotropy of the sample, the dielectric tensor takes a slightly different form [56, 70, 74]:

$$\varepsilon = \begin{pmatrix} \varepsilon_{xx} & \varepsilon_{xy} & 0 \\ -\varepsilon_{xy} & \varepsilon_{yy} & 0 \\ 0 & 0 & \varepsilon_{zz} \end{pmatrix} = \begin{pmatrix} \varepsilon_{xx} & \varepsilon_{xy} & 0 \\ -\varepsilon_{xy} & \varepsilon_{xx}+\delta & 0 \\ 0 & 0 & \varepsilon_{zz} \end{pmatrix}, \tag{3.29}$$

where $\delta = \varepsilon_{yy} - \varepsilon_{xx}$ is a measure of the intrinsic anisotropy in the xy plane. The anisotropy of the dielectric tensor must be reflected in the magneto-optical Kerr effect, too. Thus, we should see changes in the MOKE angles when we rotate the polarization plane of the incoming linearly polarized beam. This is what we call anisotropic polar MOKE (AP-MOKE).

Just like in the isotropic case, we use the Fresnel equation to derive the normalized eigenmodes and the associated indices of refraction in the material. Inserting (3.29) into (3.17) yields

$$n_j^2 = \bar{\varepsilon} \pm \varepsilon_{xy}\sqrt{\tau^2 - 1}, \tag{3.30}$$

$$\mathbf{E}_{0,j} = \left(\sqrt{1 + \left|\tau \pm \sqrt{\tau^2-1}\right|^2}\right)^{-1} \begin{pmatrix} 1 \\ \tau \pm \sqrt{\tau^2 - 1} \end{pmatrix}, \tag{3.31}$$

where $\bar{\varepsilon} = (\varepsilon_{xx} + \varepsilon_{yy})/2$ is the average dielectric tensor component of the x and y direction, $\tau = \delta/(2\varepsilon_{xy})$ characterizes the intrinsic anisotropy and the magneto-optical activity of the system, and $j = 1, 2$.

In the case of a system with negligible anisotropy, that is for $\delta \ll \varepsilon_{xy}$ or $\tau \to 0$, this reduces to the solution for an isotropic system given in Eqs. (3.19) and (3.20). That means the observed rotation and the ellipticity of the reflected beam contain only purely magneto-optical contributions. On the other hand, if the magneto-optical activity of the material is much smaller than its intrinsic anisotropy, namely $\delta \gg \varepsilon_{xy}$ or $\tau \to \infty$, we obtain

$$n_1^2 = \varepsilon_{xx}, \quad (3.32) \qquad \mathbf{E}_{0,1} = \begin{pmatrix} 1 \\ 0 \end{pmatrix}, \quad (3.34)$$

$$n_2^2 = \varepsilon_{yy}, \quad (3.33) \qquad \mathbf{E}_{0,2} = \begin{pmatrix} 0 \\ 1 \end{pmatrix}. \quad (3.35)$$

In that latter case the rotation and the ellipticity of the reflected beam are caused by the intrinsic anisotropy of the system and contains no magneto-optical contributions. However, the general case involves a superposition of both effects.

The Jones vector formalism [71] provides a simple way of describing a reflection in terms of a reflection matrix ρ. If $\mathbf{E}$ denotes the incoming beam and $\mathbf{E}'$ the reflected beam, we can write

$$\begin{pmatrix} E_x' \\ E_y' \end{pmatrix} = \begin{pmatrix} \rho_{xx} & \rho_{xy} \\ \rho_{yx} & \rho_{yy} \end{pmatrix} \begin{pmatrix} E_x \\ E_y \end{pmatrix}. \tag{3.36}$$

Given that the material has the refractive indices n_j of (3.30) and that the surrounding medium has a refractive index of $n = 1$, we can use the boundary conditions of electromagnetism to derive [75]

$$\rho_{xx} = \frac{E_x'}{E_x} = \frac{\beta_2(1-n_1)(1+n_2) - \beta_1(1+n_1)(1-n_2)}{(\beta_2-\beta_1)(1+n_1)(1+n_2)}, \tag{3.37}$$

$$\rho_{xy} = \frac{E_x'}{E_y} = \frac{-2(n_2-n_1)}{(\beta_2-\beta_1)(1+n_1)(1+n_2)}, \tag{3.38}$$

$$\rho_{yx} = \frac{E_y'}{E_x} = \frac{2\beta_1\beta_2(n_2-n_1)}{(\beta_2-\beta_1)(1+n_1)(1+n_2)}, \tag{3.39}$$

$$\rho_{yy} = \frac{E_y'}{E_y} = \frac{\beta_2(1+n_1)(1-n_2) - \beta_1(1-n_1)(1+n_2)}{(\beta_2-\beta_1)(1+n_1)(1+n_2)}. \tag{3.40}$$

Here, the parameter β_j $(j = 1,2)$ describes the eigenmodes $\mathbf{E}_{0,j}$ in the material and is defined as

$$\beta_j = \frac{E_{0,j,y}}{E_{0,j,x}} = \tau \pm \sqrt{\tau^2 - 1}. \tag{3.41}$$

Finally, for an incoming beam polarized along the x direction, we can derive the following general expressions for the total observed rotation θ_{tot} and ellipticity ϵ_{tot} [75]:

$$\tan\left(2\theta_{\text{tot}}\right) = -2\,\frac{\operatorname{Re}\left[\rho_{xx}\bar{\rho}_{yx}\right]}{\left|\rho_{xx}\right|^2 - \left|\rho_{yx}\right|^2}, \tag{3.42}$$

$$\sin\left(2\epsilon_{\text{tot}}\right) = -2\,\frac{\operatorname{Im}\left[\rho_{xx}\bar{\rho}_{yx}\right]}{\left|\rho_{xx}\right|^2 + \left|\rho_{yx}\right|^2}. \tag{3.43}$$

Note that θ_{tot} and ϵ_{tot} include both intrinsic and magneto-optical contributions. The intrinsic contribution by the diagonal components of the dielectric tensor is even in the magnetization $\mathbf{M}$, while the magneto-optical contribution by the off-diagonal components is odd in $\mathbf{M}$ [55, 56, 76]. We can use that to extract the pure magneto-optical contribution to the total rotation and ellipticity, which we call AP-MOKE. The expansion

$$\theta_{\text{tot}}(M) = \theta_K(M) + \theta_{\text{diag}}\left(M^2\right), \tag{3.44}$$

$$\epsilon_{\text{tot}}(M) = \epsilon_K(M) + \epsilon_{\text{diag}}\left(M^2\right), \tag{3.45}$$

where the index K indicates a magneto-optical Kerr effect quantity, "diag" refers to the intrinsic contribution of the diagonal components of ε, and M is the value of the magnetization along z, leads to

$$\theta_K(M) = \frac{1}{2}\left(\theta_{\text{tot}}(M) - \theta_{\text{tot}}(-M)\right), \tag{3.46}$$

$$\epsilon_K(M) = \frac{1}{2}\left(\epsilon_{\text{tot}}(M) - \epsilon_{\text{tot}}(-M)\right). \tag{3.47}$$

The expressions (3.42) and (3.43) are valid only if the polarization of the incoming beam is along the x direction. However, the goal is to show the anisotropy of P-MOKE in materials that have an intrinsic anisotropy of the form (3.29). For that reason we have to consider rotations of the polarization plane of the incoming beam around the z axis.

We can use the above expressions for arbitrary polarization directions if we keep the polarization of the incoming beam fixed along the x direction while we rotate the sample in the xy plane in the opposite direction. A rotation of the polarization direction by an angle φ with respect to the x axis thus corresponds to a rotation of the sample by an angle $-\varphi$. In terms of the dielectric tensor of the sample, this can be expressed as

$$\varepsilon(-\varphi) = R_z(-\varphi)\varepsilon R_z^{\mathrm{T}}(-\varphi) = \begin{pmatrix} \varepsilon_{xx}(-\varphi) & \varepsilon_{xy}(-\varphi) & 0 \\ \varepsilon_{yx}(-\varphi) & \varepsilon_{yy}(-\varphi) & 0 \\ 0 & 0 & \varepsilon_{zz} \end{pmatrix}, \tag{3.48}$$

where the superscript T denotes the transpose. The rotation around the z axis by an angle $-\varphi$ is given by the rotation matrix

$$R_z(-\varphi) = \begin{pmatrix} \cos\varphi & \sin\varphi & 0 \\ -\sin\varphi & \cos\varphi & 0 \\ 0 & 0 & 1 \end{pmatrix}. \tag{3.49}$$

The transformed components of the dielectric tensor then read

$$\varepsilon_{xx}(-\varphi) = \varepsilon_{xx} + \frac{1}{2}\big(\delta - \delta\cos(2\varphi)\big), \tag{3.50}$$

$$\varepsilon_{yy}(-\varphi) = \varepsilon_{xx} + \frac{1}{2}\big(\delta + \delta\cos(2\varphi)\big), \tag{3.51}$$

$$\varepsilon_{xy}(-\varphi) = \varepsilon_{xy} + \delta\cos\varphi\sin\varphi, \tag{3.52}$$

$$\varepsilon_{yx}(-\varphi) = -\varepsilon_{xy} + \delta\cos\varphi\sin\varphi. \tag{3.53}$$

Taking into account that $\bar{\varepsilon}(-\varphi) = \big(\varepsilon_{xx}(-\varphi) + \varepsilon_{yy}(-\varphi)\big)/2 = (\varepsilon_{xx} + \varepsilon_{yy})/2 = \bar{\varepsilon}$ is invariant under rotation and that τ transforms according to

$$\tau(-\varphi) = \frac{\delta}{2(\varepsilon_{xy} + \delta\cos\varphi\sin\varphi)}, \tag{3.54}$$

we can obtain angle-dependent versions of Eqs. (3.30) and (3.31). We are now in a position to calculate the angle-dependent Kerr rotation $\theta_K(\varphi)$ and the Kerr ellipticity $\epsilon_K(\varphi)$ of an anisotropic sample for arbitrary angles φ of linear polarization of the incoming beam. All we need is data for the dielectric tensor components, which are the result of an *ab initio* optics calculation. In the following chapters we make use of the theory developed in this exposition to analyze selected optical properties of hydrogenated graphene and an Fe/GaAs(001) model system, such as the optical conductivity and AP-MOKE.

4

Hydrogenated Graphene

The discovery of graphene in 2004 came as a surprise [77]. Not only because of the stunning simplicity of the Scotch tape exfoliation method, but also because the existence of a two-dimensional material seemed to defy fundamental principles. That was the beginning of an unprecedented materials science success story [78].

Historically, it has taken about 40 years for newly designed materials to evolve from mere lab curiosities to standard components of consumer products. Graphene is poised to do that in just ten. Virtually all of its properties are exceptional [79], which makes graphene an extremely attractive material for science and technology, and myriads of applications have been proposed.

In 2013 the European Union launched its *Graphene Flagship*, loaded with one billion euros to support academic and industrial graphene research for the next decade. Furthermore, Korean scientists recently announced the wafer-scale growth of single-crystal monolayer graphene [80]. It is this sort of international effort that could establish graphene as an everyday material in the near future.

Indeed, graphene is likely to cause a paradigm shift [81, 82]. It could enable flexible displays, wearables, biosensors, efficient solar cells, high-performance batteries, etc., and applications we have not yet conceived. This could make it possible to embed digital devices almost everywhere, and thus greatly enhance the quality and extent of a future *internet of things*.

4.1 Graphene

Graphene is a two-dimensional honeycomb lattice of carbon atoms and was first studied as a theoretical model in the middle of the 20th century [83–85]. Decades later, yet before its discovery, it was realized that graphene can serve as a model system for quantum electrodynamics in $(2+1)$ dimensions [86–88]. Indeed, once graphene could be fabricated, its charge carriers were found to behave like massless Dirac fermions with a Fermi velocity (which corresponds to the speed of light) of about $v_F \approx 10^6\,\mathrm{m/s}$ [89]. This allows for studying relativistic phenomena like the Klein paradox [90] or *zitterbewegung* [91] in condensed matter experiments while they are unobservable in particle physics.

The stability of graphene at elevated temperatures seems to defy the Mermin-Wagner theorem that states the instability of two-dimensional crystals at finite temperature [92]. Yet graphene is not strictly flat: It exhibits a rippled structure on a scale much larger than a single unit cell, which can be interpreted as a metastable state [93]. Eventually, stable graphene flakes could be isolated by repeatedly sticking Scotch tape on a sheet of graphite and peeling it off. This simple technique greatly benefits from the remarkably high optical absorption of graphene, which is about 2.3% in the visible spectrum [94], because the resulting graphene flakes on the Scotch tape can be observed with an optical microscope.

Its hexagonal structure is the cause of the quasi-relativistic nature of the charge carriers in graphene—a property that is characteristic for a whole new class of two-dimensional graphene-like materials [95]. The energy-momentum dispersion in graphene is linear for low energies, and its band structure exhibits a formation called the *Dirac cone* at the inequivalent K and K' points at the corners of the two-dimensional hexagonal Brillouin zone. Graphene can thus be viewed as a zero-gap semiconductor, or equivalently as a zero-overlap semimetal.

Harder than diamond, stronger than steel, excellent thermal and electronic conductivity—the list goes on. Roughly two dozen material property superlatives are attributed to graphene, most of which make it the proclaimed wonder material for many technological applications. The transport properties of graphene would make it an ideal material for nanoelectronic devices, if only it had a band gap…

4.2 Chemical Functionalization

Quite some effort has gone into the search for a controlled way of creating and tuning a band gap in graphene. Such a method could pave the way to novel devices that combine the assets of graphene and modern semiconductor technology [96]. We know that restricting its size [97,98] or placing it on special substrates [99] can induce a band gap in graphene, but these approaches are irreversible, difficult to implement in devices, and result in fragile band gaps.

Chemical functionalization of graphene is more promising [100–104]. The decoration of graphene with adsorbates or adatoms is a viable and reversible method to induce robust, tunable band gaps. The adatoms are likely to self-organize into periodic structures on top of graphene, and they can be removed without leaving a trace simply by heating. If it were possible to selectively cover parts of a graphene sample with adatoms, one could induce local chemical alterations, and create confined metallic or semiconducting regions: A whole integrated circuit could be fabricated from a single graphene sheet.

Since graphene is pure surface without bulk, chemically induced changes are very strong, and decoration with adatoms such as oxygen [105], flourine [106, 107], or hydrogen [108–112] alters the properties of graphene significantly. In some cases, such a modification causes graphene to transition to another class of material.

Fully hydrogenated graphene (one carbon sublattice is covered on one side, the other carbon sublattice is covered on the other side) is commonly called *graphane*. It is a nonmagnetic, direct wide-gap semiconductor that was predicted in 2007 from first-principles calculations [113] and demonstrated in the laboratory two years later [114].

Semihydrogenation, in contrast, produces the ferromagnetic, indirect narrow-gap semiconductor *graphone* [115]. Here, only one carbon sublattice is covered on only one side, which corresponds to 50% single-side hydrogenation (SSH). This modification of graphene has not yet been synthesized, but the transition from graphene to graphone and graphane with increasing degree of hydrogenation shows that the amount of adatom coverage is decisive for the properties of the resulting graphene derivate.

The presence of magnetic moments is such a property. Several studies suggest that graphene indeed becomes magnetic for certain degrees of hydrogenation [116–121], which is of particular importance to graphene spintronics [122–124].

The dependence of the exchange-split band structure of hydrogenated graphene on the hydrogen coverage can be studied by optical spectroscopy, which allows us to determine if its ground state is magnetic or not.

The optical properties of graphene itself continue to inspire many possible applications of the material in the field of optoelectronics and photonics [125–128]. Consequently, the optical conductivity of graphene is another property that has been investigated both theoretically and experimentally for many graphene-based systems, including single [129–133] and few layer graphene [134, 135], graphite [136–138], and carbon nanotubes [139].

In this work we use first-principles density functional theory to investigate how hydrogenation of graphene influences its optical conductivity spectrum. We consider four graphene model systems with different degrees of uniform single-side hydrogenation, 50%, 12.5%, 2%, and 0% (pristine graphene), and compare their calculated optical conductivity spectra.

4.3 Method

We use graphene supercells of different size, each containing a single additional hydrogen atom, to represent different degrees of single-side hydrogenation (SSH; see Fig. 4.1). Graphone (50% SSH graphene) is modeled by a standard graphene unit cell consisting of two carbon atoms and one hydrogen atom. The hydrogenation degrees of 12.5% and 2% are represented by a 2×2 and a 5×5 supercell, respectively. The former contains one hydrogen atom and eight carbon atoms, while the latter consists of one hydrogen atom and fifty carbon atoms. Pristine graphene (0% SSH) is given by its standard unit cell. A vertical distance between the graphene sheets of 15 Å is chosen to suppress interlayer coupling.

To ensure structural soundness, the atomic positions of the three hydrogenated graphene cells are optimized using Quantum Espresso [140], a DFT code which implements the plane wave pseudopotential method and a quasi-newton algorithm for atomic force relaxation. Ultrasoft carbon and hydrogen pseudopotentials [141] are used together with the Perdew-Burke-Ernzerhof variant of the generalized gradient approximation (PBE-GGA) [27] for the exchange-correlation functional.

Quantum Espresso is a reasonable choice for the structural optimization of large supercells because plane wave basis sets are computationally efficient and independent of atom positions and species. The calculated total forces are

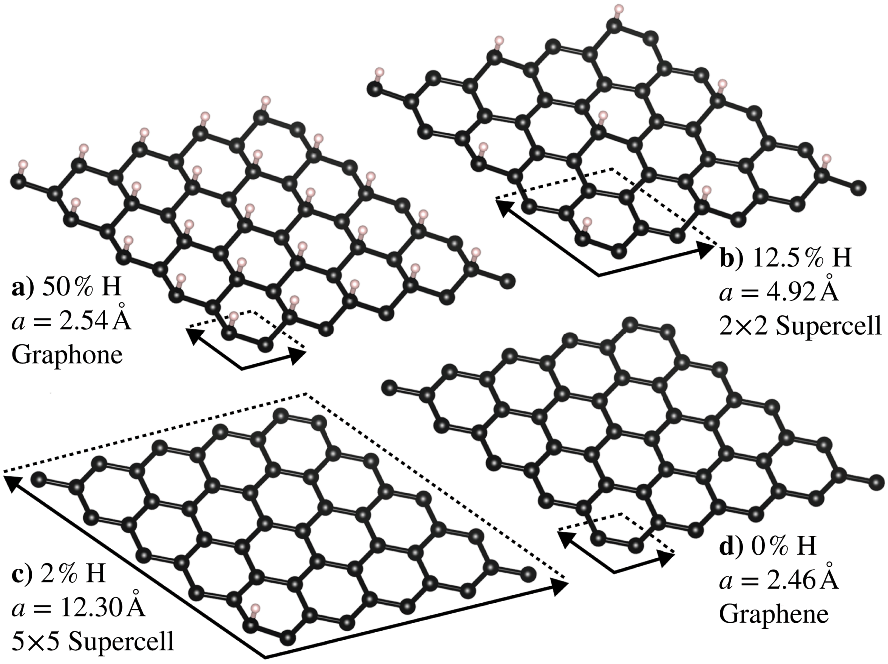

Figure 4.1 – Comparison of the four different model systems investigated in this study using Quantum Espresso structure optimization data. The unit cell of graphone (a) contains 2 C + 1 H atoms and has a single-side hydrogen coverage of 50%. The larger 2×2 (b) and 5×5 (c) supercells contain 8 C + 1 H and 50 C + 1 H atoms, respectively, accounting for 12.5% and 2% of hydrogen coverage. Pristine graphene (d) with two C atoms per unit cell corresponds to 0% hydrogen coverage. The lattice constant a is given for each system.

thus true Hellman-Feynman forces [142] and do not require Pulay basis-set corrections [143]. For the self-consistent structural optimization we choose a kinetic energy cutoff for the wave functions of 30 Ry. We use a Monkhorst-Pack [144] grid of $(30 \times 30 \times 1)$ k points in the full first Brillouin zone of graphene, which corresponds to $(15 \times 15 \times 1)$ and $(8 \times 8 \times 1)$ k points in the case of the 2×2 and the 5×5 supercell, respectively. A total energy difference smaller than 10^{-8} Ry and a force difference smaller than 10^{-3} a.u. for subsequent iterations serve as convergence criteria. With this choice of parameters we obtain relaxed structures that exhibit well-converged optical properties.

The optimized structural parameters of each system are given in Table 4.1, where the quantity Δ / d_{CC} represents the tetragonal out-of-plane distortion (rippling). It increases with decreasing hydrogen coverage, because each C-H bond effectively removes an electron from the graphene plane, which weakens the C-C bonds of the hydrogenated carbon atoms and expands the structure. That expansion becomes less pronounced for decreasing densities of hydrogenated carbon atoms, while their vertical distance to the graphene plane increases.

Table 4.1 – Structural parameters of the investigated hydrogenated graphene systems after relaxation. The in-plane supercell edge length is denoted by a (the vertical edge length $c = 15$ Å for each supercell), while the C-H bond length and the C-C distance between the carbon atoms surrounding a hydrogenated carbon site are given by d_{H} and d_{CC}, respectively. The parameter Δ describes the vertical distance between a hydrogenated carbon atom and its neighbors, with the ratio Δ/d_{CC} being a measure for the out-of-plane distortion induced by hydrogenation. All lengths are given in angstroms (Å).

System	SSH	a	d_{H}	d_{CC}	Δ	Δ/d_{CC}
Graphone	50 %	2.54	1.158	2.537	0.322	12.9 %
2×2	12.5 %	4.92	1.131	2.500	0.344	13.8 %
5×5	2 %	12.30	1.128	2.516	0.363	14.4 %

In the next step we calculate the electronic band structure and the total density of states (DOS) for each SSH graphene model system using the full-potential linearized augmented plane wave [42,43] code WIEN2k [47]. Again, we choose PBE-GGA as the exchange-correlation functional and obtain the self-consistent electronic ground state density for each system. We require that the charge distance between two consecutive iterations of the self-consistent field cycle, integrated over the unit cell, be smaller than $10^{-5}e$, where e is the positive value of the elementary charge.

The irreducible Brillouin zone is sampled with $(9 \times 9 \times 1)$ Monkhorst-Pack k points for the 5×5 supercell, and at least $(15 \times 15 \times 1)$ k points for the other systems. The effect of adatom-induced magnetic moments on the optical properties of hydrogenated graphene can be studied by performing both nonmagnetic (the calculation explicitly disregards the electron spin) and spin-polarized calculations for each system. For pristine graphene we perform only a nonmagnetic reference calculation.

Having obtained the converged Kohn-Sham eigenenergies and eigenstates, we calculate the imaginary part of the complex dielectric function according to Eq. (3.15). Since the calculation of optical properties requires very dense k-point meshes, we choose a sampling of $(45 \times 45 \times 1)$ k points for the 5×5 supercell and at least $(51 \times 51 \times 1)$ k points for the other supercells. The integration in k space follows the Blöchl tetrahedron method [145], and we only take into account direct interband transitions from occupied to unoccupied bands up to an energy of 20 eV above the Fermi energy.

Finally, we use Eq. (3.12) to calculate the real part of the complex optical conductivity from the imaginary part of the dielectric function. Note that this results in the optical conductivity associated with a three-dimenstional slab supercells, rather than an essentially two-dimensional hydrogenated graphene film. To obtain the desired value of the optical conductivity associated with the two-dimensional system, we have to multiply the result of the three-dimensional case by the interlayer spacing of 15 Å. Furthermore, we normalize the calculated spectra to the universal ac optical conductivity of graphene [94, 146–148], which is given by $\sigma_0 = e^2/(4\hbar)$. This facilitates interpreting the results and comparing them to existing theoretical and experimental work.

4.4 Results

In pristine graphene, each carbon atom is sp^2 hybridized and covalently bonded to its three neighbors, while the hydrogenated carbon atoms in hydrogenated graphene are closer to an sp^3-hybridized tetrahedral conformation with the C-H bond axis oriented perpendicular to the graphene layer. The carbon atoms carrying a hydrogen atom are thus shifted out of plane, which leads to a buckling of the graphene sheet in the vicinity of hydrogenated carbon sites.

In the dilute limit of hydrogenation, an isolated hydrogen adatom alters the properties of graphene only locally, whereas a high degree of hydrogen coverage significantly changes its atomic and electronic structure. For instance, each additional isolated hydrogen atom contributes a magnetic moment of 1 μ_B.

To study the influence of those magnetic moments on the electronic band structure and the optical conductivity of hydrogenated graphene, we perform a spin-polarized and a non-spin-polarized (nonmagnetic) calculation for each model system. Moreover, with the help of the calculated electronic band structure and the total DOS presented in Figs. 4.2–4.5, we identify those direct interband transitions that significantly contribute to the pronounced features of the optical conductivity spectra shown in Fig. 4.7.

Arrows and capital letters in Figs. 4.2–4.5 mark transitions representative of all transitions that can occur between a given pair of bands at different values of **k**. Those transitions match the features identified with the same capital letters in Fig. 4.7. A summary of the calculated band gap widths at high-symmetry points and the exchange splittings at the Fermi energy is given by Table 4.2. The exchange splittings have been derived by determining the distance between corresponding characteristic peaks in the spin-resolved total DOS (see the bottom right panels of Figs. 4.2–4.4).

Table 4.2 – Band gaps at the Γ and K point (non-magnetic case), and exchange splitting at the Fermi energy (spin-polarized case), given in electron volts (eV).

System	SSH	Γ gap	K gap	Exchange splitting
Graphone	50 %	3.93	8.20	2.01
2×2	12.5 %	1.87	2.63	0.80
5×5	2 %	1.27	0.62	0.27

Electronic Structure

The Dirac cone at the K point is absent in the spin-polarized and the nonmagnetic case of graphone (see Fig. 4.2). A band gap opens, and a relatively flat midgap state, which is exchange split in the spin-polarized case, appears close to the Fermi level. In the nonmagnetic case, that midgap state crosses the Fermi level, resulting in a metallic band structure. Its exchange-split equivalent in the spin-polarized case results in an indirect band gap of about 0.47 eV between the valence band maximum along the $\overline{K\Gamma}$ high-symmetry line and the conduction band minimum at the Γ point. These bands are responsible for the characteristic features of the optical conductivity spectra at energies $\lessapprox 5$ eV. Owing to their high DOS they provide the initial or final states for many transitions.

The 12.5 % SSH graphene case (see Fig. 4.3) is similar to the previous case, but shows a smaller exchange splitting of the bands in the spin-polarized calculation (see Table 4.2). The midgap states are flatter and their smaller splitting leads to a narrower indirect band gap of about 0.39 eV in the spin-polarized case, whereas the nonmagnetic case is metallic. This is consistent with the smaller areal density of magnetic moments in the 2×2 supercell as compared to the small cell of graphone, which illustrates the decreased influence of the magnetic moments in this case of intermediate hydrogen coverage. Another observation is that the K point states of the neighboring bands (or exchange-split band pairs) above and below the midgap states are closer to the Fermi energy than for graphone.

In the dilute limit of 2% SSH graphene (see Fig. 4.4) the exchange splitting is even smaller than in the previous cases, aligning the spin-polarized with the nonmagnetic band structure. This is because the magnetic moments contributed by the hydrogen adatoms are distributed over the fifty carbon atoms of the 5×5 supercell. The midgap states are almost completely flat, and the neighboring bands above and below the midgap states approach each other at the K points. If the hydrogen coverage were reduced below 2%, a Dirac cone would eventually reform. The reference calculation for pristine graphene is given in Fig. 4.5.

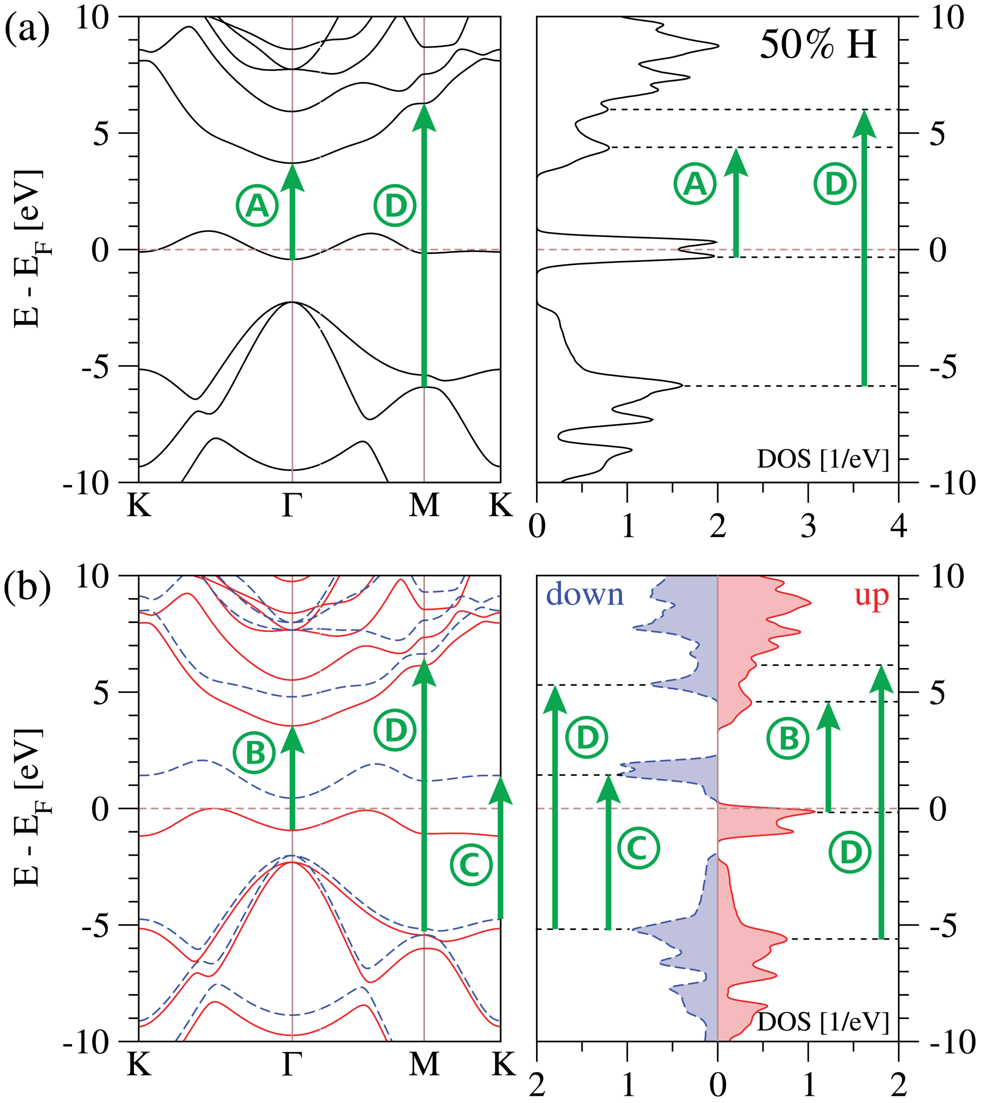

Figure 4.2 – Calculated electronic band structure along high-symmetry lines in the first Brillouin zone (left panels) and broadened total DOS per unit cell (right panels) for the nonmagnetic (a) and the spin-polarized (b) 50% SSH case (graphone). In the spin-polarized case the spin-resolved total DOS is shown; quantities associated with spin up (down) are shown as solid red (dashed blue) lines. Energies are given relative to the Fermi energy E_F. Labeled arrows indicate direct interband transitions corresponding to pronounced features in the optical conductivity spectra (see Fig. 4.7).

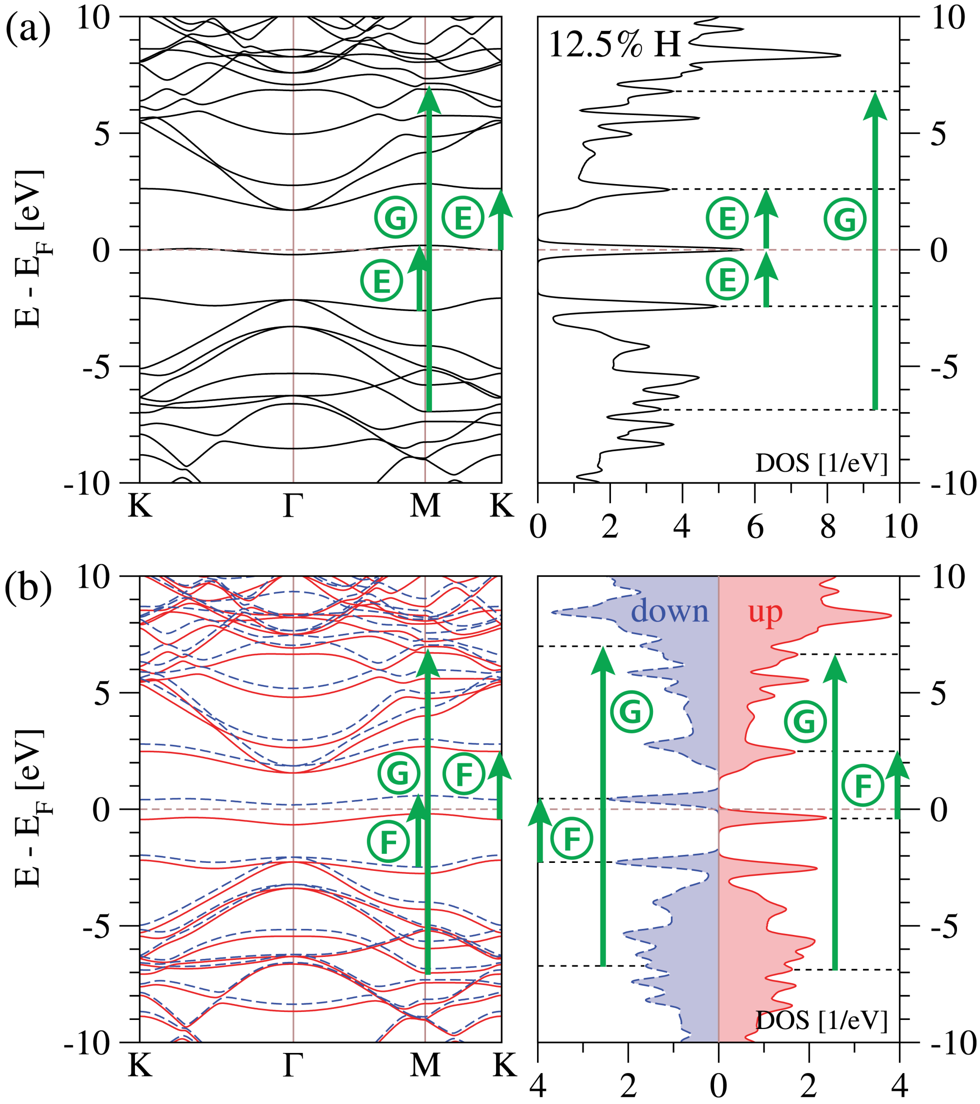

Figure 4.3 – See caption of Fig. 4.2, but for the 12.5% SSH case (2×2 supercell).

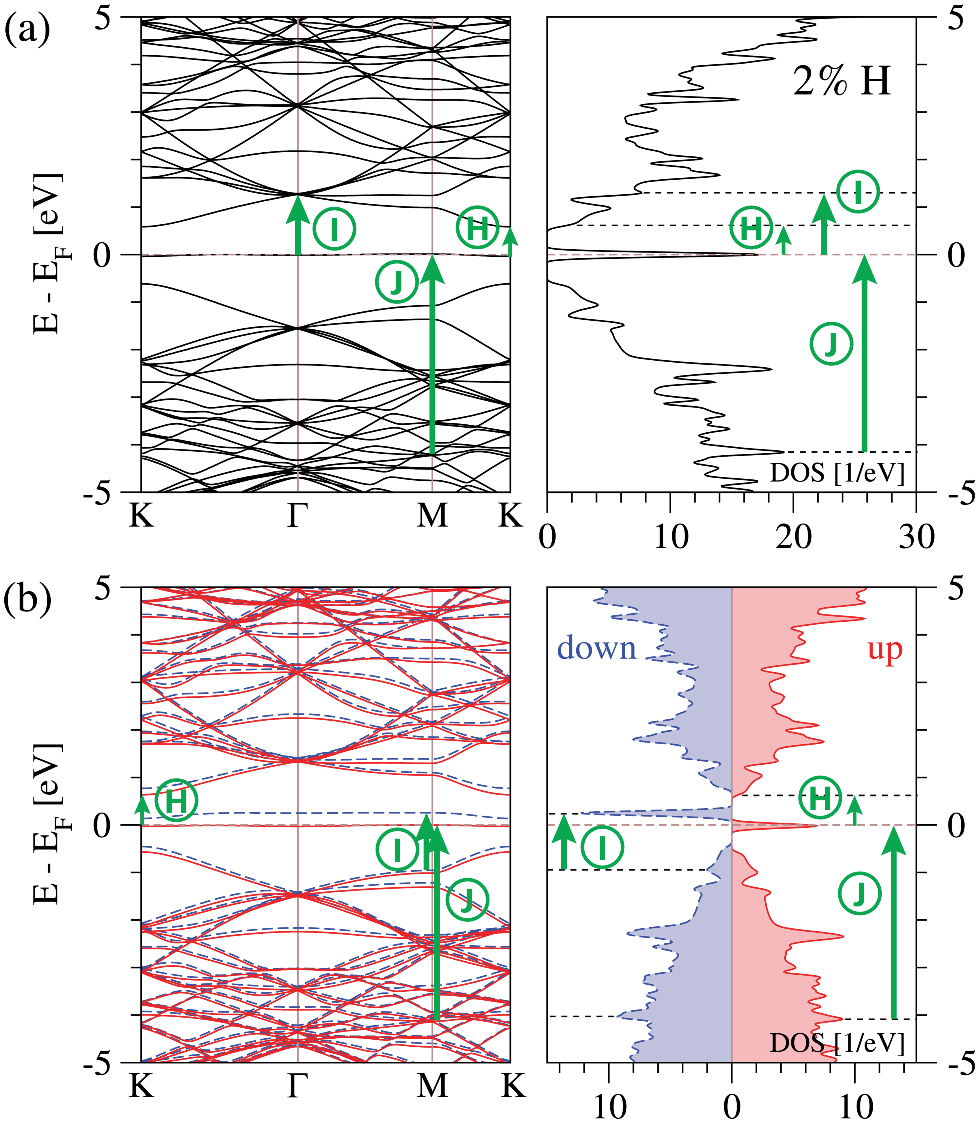

Figure 4.4 – See caption of Fig. 4.2, but for the 2% SSH case (5 × 5 supercell).

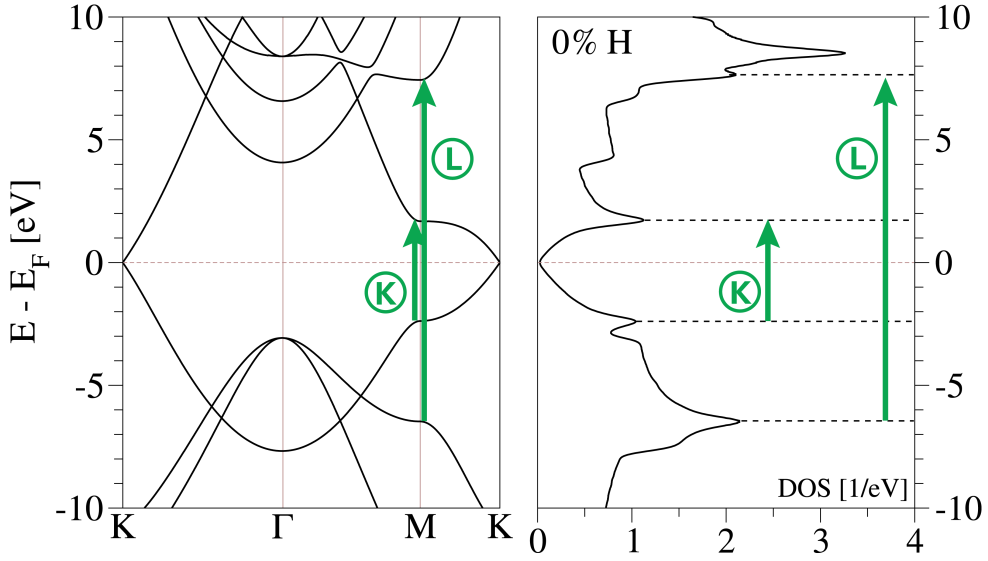

Figure 4.5 – See caption of Fig. 4.2, but for nonmagnetic pristine graphene.

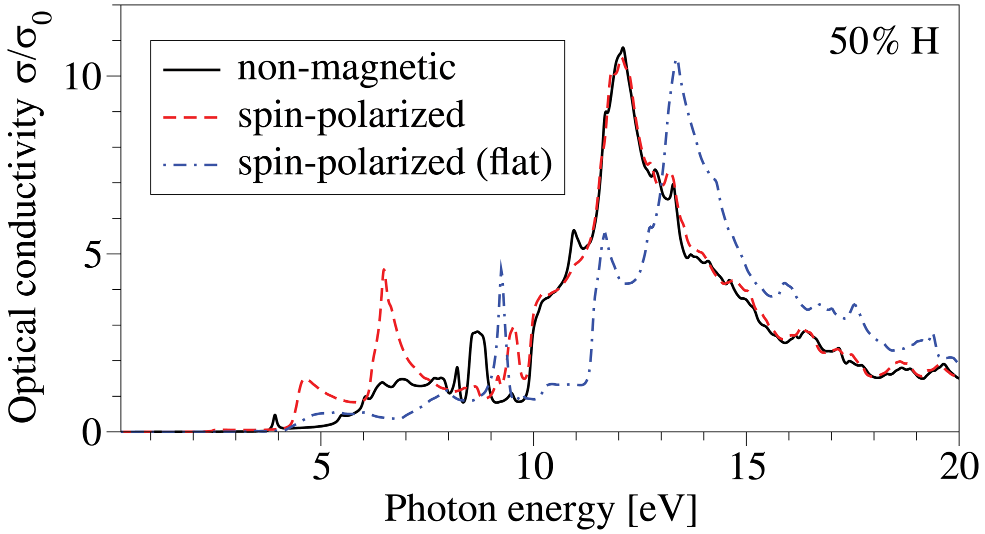

Figure 4.6 – Calculated real part of the complex optical conductivity σ in units of the universal ac optical conductivity σ_0 of graphene for 50% SSH graphene, comparing the nonmagnetic, the spin-polarized, and another spin-polarized but unrelaxed flat case, in which all carbon atoms are restricted to the same plane.

Influence of Structure and Magnetic Moments

In order to determine how strongly the presence of magnetic moments, or of different structural characteristics, influences the optical conductivity spectrum of hydrogenated graphene, we compare the spectra of 50% SSH graphene for the following three cases: the nonmagnetic case, the spin-polarized case, and an artificially flat spin-polarized case in which all carbon atoms are restricted to the same plane. The results are shown in Fig. 4.6, which is equivalent to Fig. 4.7a, except for the additional curve of the flat spin-polarized case.

The spectrum of the flat spin-polarized case is shifted towards higher energies with respect to the nonmagnetic case, but the overall shape is similar and both cases have their most pronounced spectral features in common. In contrast, the result for the relaxed (buckled) spin-polarized case is very different (as discussed above). This indicates that magnetism in the flat case is quenched. Hence, we conclude that the out-of-plane distortion of the hydrogenated carbon atom is a structural characteristic that is crucial to the optical properties of hydrogenated graphene within the PBE-GGA framework.

The influence of magnetic moments, if present, is also considerable, which is why we expect an optical measurement to be able to detect the presence of magnetic moments in real hydrogenated graphene samples. However, it should be noted that Casolo *et al.* [149] demonstrated that the quenching of magnetism in the flat hydrogenated graphene system is due to the self-interaction error afflicting GGA functionals such as PBE, and thus not physical, and that magnetism in the flat system is recovered in calculations employing hybrid functionals such as PBE0, which mixes PBE exchange with Hartree-Fock exchange.

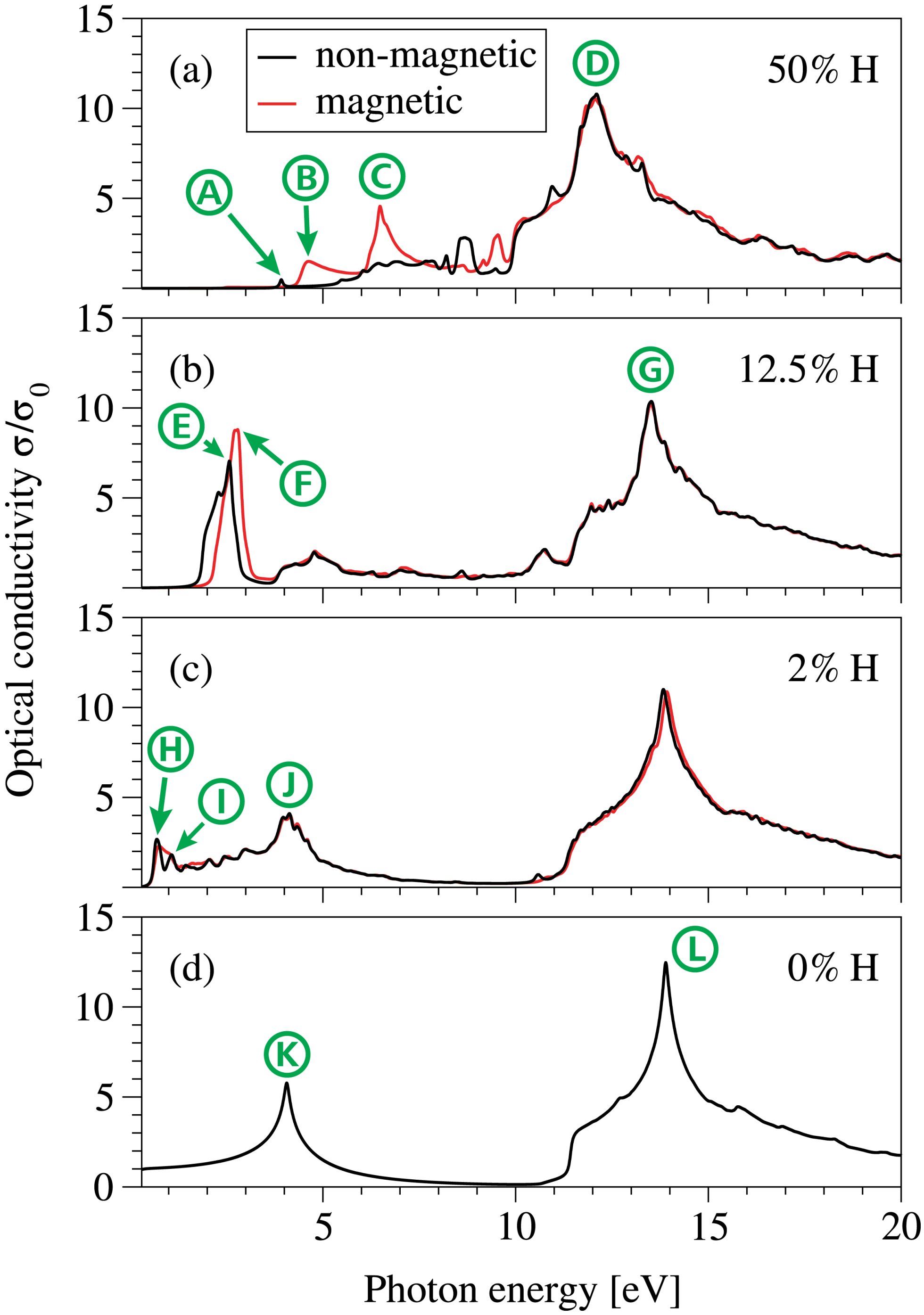

Figure 4.7 – Calculated real part of the complex optical conductivity σ for 50% (a), 12.5% (b), and 2% (c) SSH graphene, as well as pristine graphene (d), given in units of the universal ac optical conductivity σ_0 of graphene. Pronounced features of the spectra are labeled in concordance with the arrows in Figs. 4.2–4.5, indicating the most important transitions contributing to them.

Optical Conductivity

The optical conductivity spectra for all four systems are calculated for photon energies ranging from 0.3 to 20 eV with a resolution of 1.36 meV, comprising the infrared, visible, and ultraviolet (IR-VIS-UV) parts of the electromagnetic spectrum. To account for finite-lifetime effects a Lorentzian broadening of 50 meV is applied. Figure 4.7 presents the results of both the spin-polarized and the nonmagnetic calculation for each hydrogenated system. In the following, we will refer to the labels used in Figs. 4.2–4.7 by capital letters in parentheses, such as (A).

Within the energy range covered by our calculation, graphone (see Fig. 4.7a) is transparent for photon energies below 5 eV, except for a small peak (A) at 3.9 eV. The most prominent feature is a broad peak at about 12.1 eV (D). For energies between 4 and 10 eV the spectra of the nonmagnetic and the spin-polarized case differ considerably, as the spin-split band structure of the latter gives rise to two new peaks at 4.6 eV (B) and 6.6 eV (C), while the spectra are similar for energies above 10 eV. This indicates that for 50% single-side hydrogenation the optical conductivity spectrum is significantly influenced by magnetic moments for photon energies below 10 eV.

The 12.5% SSH graphene case shows an interesting feature (see Fig. 4.7b). By coincidence, the transitions to and from the midgap state (or the exchange-split midgap states in the spin-polarized case) are of the same energy, and both contribute to a pronounced peak at 2.5 eV (E) or 2.8 eV (F) in the visible part of the electromagnetic spectrum between 1.5 and 3 eV. The center of the broad peak similar to that in the 50% SSH case is shifted to higher energies and is centered at 13.6 eV (G).

The dilute 2% hydrogenation case (see Fig. 4.7c) shows many features in the low-energy region from 0.3 to 5 eV, the most important of which are the absorption peaks at 0.7 eV (H), 1.1 eV (I), and 4.2 eV (J). The broad peak centered at 13.9 eV is shifted to higher energies compared to the previous two cases. The spectra for the nonmagnetic and the spin-polarized case hardly differ, which is consistent with the low areal density of magnetic moments in the 2% SSH case (1 μ_B per 50 carbon atoms). The overall shape of the spectrum is approaching the reference spectrum of pure graphene (see Fig. 4.7d), whose most pronounced features are the peaks at 4.1 eV (K) and 13.9 eV (L).

4.5 Conclusions

We studied the influence of hydrogenation on the optical conductivity of hydrogenated graphene from first-principles calculations. Different degrees of hydrogenation were simulated by optimized-geometry graphene supercells of different size, each containing an additional hydrogen atom. Performing both an explicitly nonmagnetic and a spin-polarized calculation for each supercell, we obtained the electronic band structure and total density of states for 50%, 12.5%, 2%, and 0% hydrogenated graphene. These results were used to calculate the corresponding optical conductivity spectra in linear response over the IR-VIS-UV range of the electromagnetic spectrum.

While the dense hydrogenation in the 50% SSH case exhibited a spectrum distinct from that of pure graphene, the influence of the local tetrahedral conformation of the hydrogenated carbon atoms and the resulting magnetic moments degraded with decreasing hydrogenation density. For intermediate values of hydrogenation we observed the coincidental appearance of a pronounced peak in the optical conductivity in the visible part of the spectrum.

Since the influence of hydrogenation on the optical conductivity was found to be significant, one could employ optical measurement techniques (for example an absorption measurement) to monitor the hydrogenation process, or one could tailor the optical conductivity of graphene by reversible hydrogenation. Furthermore, our results suggest that an optical measurement could determine if the ground state of hydrogen-functionalized graphene is magnetic or not.

Finally, a comparison of three different calculations of the 50% SSH case showed that, within the PBE generalized gradient approximation to the exchange-correlation functional, structural changes induced by hydrogen adatoms are ultimately responsible for additional magnetic moments and hydrogenation-dependent optical conductivity spectra.

Going beyond Kohn-Sham DFT with a GW calculation, the electronic structure of hydrogenated graphene exhibits larger band gaps [150–152], leading to a shift in energy of the characteristic optical conductivity peaks of the spectra presented in this work. Although quantitatively different, the linear response spectra derived from a GW calculation should remain qualitatively unchanged. We thus expect our main results to be valid beyond standard DFT.

5

The Fe/GaAs Heterostructure

The vast majority of modern computers follow the *Von Neumann architecture* [153]. They consist of a central processing unit (CPU), a memory unit that stores both data and instructions, external mass storage, as well as input and output devices. The CPU fetches either data or instructions from memory alternatingly; they share a common bus. However, memory and CPU speeds have become increasingly disparate, and modern CPUs can process data much faster than it can be fetched from memory. The performance of computers is often limited by this *Von Neumann bottleneck*, which is aggravated by the inherent inertia of permanent mass storage.

This problem follows from the different subsystems using entirely different material technologies. The information processing subsystem (the CPU and memory) is based on semiconductor technology (CMOS), which relies on switching between logical "0" and "1" states by moving small amounts of charge, while permanent information storage and retrieval operates by reorienting magnetic domains in magnetic materials. We need hybrid devices that can fill both roles within the same technology.

That technology could be semiconductor spintronics [122, 123]. Spintronics is an attempt to generalize conventional electronics by exploiting the electron spin in addition to the electron charge. The goal is to design nanoelectronic devices that exploit spin effects [154–156], and whose fabrication can ideally be integrated into the existing CMOS infrastructure. Whereas conventional charge-based devices are limited by high switching energies and low switching speeds, spin-based devices are fast, energy-efficient, and provide non-volatile storage. It might well be possible that a spin-enabled device eliminates the Von Neumann bottleneck by providing both information processing and non-volatile storage.

Fundamental research in semiconductor spintronics rests on three pillars: spin injection, spin manipulation, and spin detection. First, a non-equilibrium spin distribution needs to be created, for example by spin injection from a ferromagnet into a semiconductor. Exploiting spin-orbit coupling (SOC) effects in the material, the spin can then be manipulated by magnetic or electric fields before the resulting spin distribution is eventually detected.

5.1 Fe/GaAs

The Fe/GaAs heterostructure was the first system in which room-temperature spin injection from a ferromagnet into a semiconductor was achieved [157]. It is an ideal model system for spin injection: Iron contributes its high Curie temperature and spin moment, and gallium arsenide its high carrier mobility and its long spin lifetime. Moreover, the lattice mismatch of these materials is rather small [158]. That allows for the epitaxial growth of unstrained Fe/GaAs interfaces, whose preparation is cheap and has been demonstrated repeatedly [159–161].

Although the Fe/GaAs(001) interface quality is known to be limited by various surface reconstructions and possible interdiffusion processes, it is easier to prepare than the Fe/GaAs(110) variant [162, 163]. It is thus the more widely studied system. The interface structure crucially determines the electronic structure of the system, such as the spin-polarization at the Fermi level and the magnetic moments. It has been found that arsenic termination of the Fe/GaAs(001) interface limits diffusion processes and favors a flat interface [164, 165]. Consequently, an As-terminated flat interface was chosen as the basic structure for the model calculations presented in the following.

The microscopic structure of the Fe/GaAs(001) interface exhibits C_{2v} symmetry [123], which manifests itself in many properties of the system. For example, the in-plane magneto-crystalline anisotropy of thin Fe layers on GaAs(001) has a dominant uniaxial contribution [166–171]. Furthermore, Fe/GaAs(001) shows a small but very robust tunneling anisotropic magneto-resistance effect, which was demonstrated by Moser *et al.* in 2007 [172]. The tunneling anisotropic magneto-thermopower and spin Seebeck effects are similar phenomena that have been predicted for this system [173,174]. All these anisotropic effects can be directly attributed to the C_{2v} symmetry of the effective SOC magnetic field at the Fe/GaAs(001) interface [175–177], which includes both Bychkov-Rashba [178] and Dresselhaus [179] contributions that stem from the structure inversion asymmetry and the bulk inversion asymmetry of the system, respectively.

Our goal is to investigate the influence of the anisotropic interface SOC fields on the optical properties of the Fe/GaAs(001) heterostructure by means of density functional theory model calculations. While we find the direction of magnetization of the Fe layer to have a negligible effect on the optical properties, the intrinsic (or crystallographic) optical anisotropy is significant. We show that it is manifest in an anisotropic optical conductivity as well as an anisotropic polar magneto-optical Kerr effect (AP-MOKE). The latter means that the Kerr angles (rotation and ellipticity) at normal incidence of the probing beam depend on its direction of linear polarization, thus reflecting the underlying anisotropy of the optical constants of the material (see Section 3.4).

We find the AP-MOKE of our Fe/GaAs(001) model system to have the same C_{2v} symmetry as the SOC fields at the interface. The anisotropy that we observe in the optical conductivity of our C_{2v} structure is to be contrasted with the *absence* of anisotropy in the Boltzmann dc conductivity [180] of a two-dimensional electron gas with Bychkov-Rashba and Dresselhaus spin-orbit interactions.

5.2 Method

We choose a slab supercell of 15 atoms (see Fig. 5.1) to model an Fe/GaAs(001) interface consisting of 9 monolayers of GaAs(001) and 3 monolayers of Fe. The interface is As-terminated and flat, and the vacuum distance between neighboring slabs is 6 Å. The structure is not relaxed, but experimental values for the lattice constants and interatomic distances are chosen. Passivation of the structure with hydrogen is not necessary since an explicit calculation shows that the SOC contribution of the As atoms at the bottom of the structure to the optical properties is negligible.

The linearized augmented plane wave method, as implemented in the DFT code package WIEN2k, is used to calculate the electronic structure of the system for various directions of the magnetization in the Fe layer. Here, a Monkhorst-Pack mesh of $(12 \times 12 \times 1)$ k points in the full first Brillouin zone is used, and an

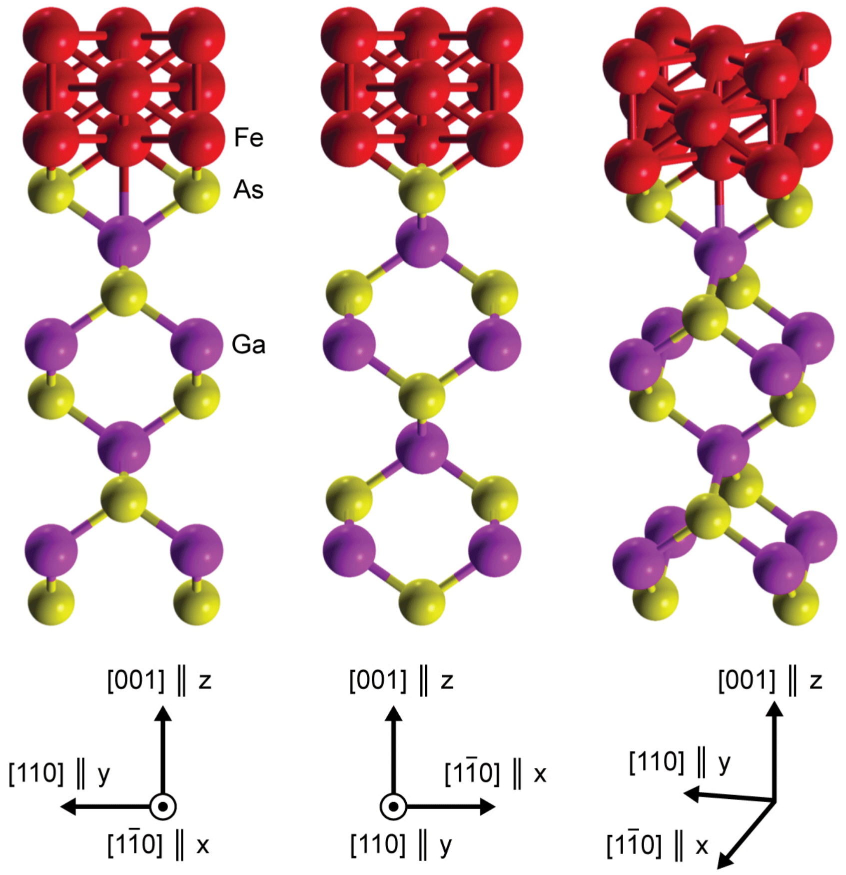

Figure 5.1 – The supercell used to model the Fe/GaAs(001) interface from three different angles. The coordinate tripods indicate the mapping of Cartesian to crystallographic axes.

accuracy of 10^{-7} Ry in the total energy is chosen as the convergence criterion. We again use the Perdew-Burke-Ernzerhof variant of the generalized gradient approximation for the exchange-correlation functional. Spin-orbit coupling is included in all calculations and for all atoms of the supercell using the method of second diagonalization native to WIEN2k. To study the magnetization-induced anisotropy of the system, the calculations are performed for the magnetization $\mathbf{M}$ oriented along x, y, and z as well as selected intermediate directions in the xy plane. The mapping of Cartesian to crystallographic axes is given in Fig. 5.1.

On top of the converged electronic densities of the previous step we calculate the dielectric function and the optical conductivity in linear response. Here, a much denser Monkhorst-Pack mesh consisting of at least $(70 \times 70 \times 1)$ k points is used. The obtained results are converged for all practical purposes. The WIEN2k optics package makes use of Eq. (3.15) to calculate the imaginary part of the complex dielectric tensor from the converged Kohn-Sham eigensystem.

The k-space integration uses the Blöchl tetrahedron method and only direct interband transitions from occupied to unoccupied bands up to an energy of 20 eV above the Fermi level are taken into account. An energy resolution of 13.6 meV is chosen for the photon energy $\hbar\omega$, and a Lorentzian broadening of 100 meV is applied to account for finite-lifetime effects. Since that broadening distorts the results unphysically for energies on the same order, results for energies smaller than 300 meV are not shown.

The real part of the optical conductivity is obtained from the imaginary part of the dielectric function by Eq. (3.12). The imaginary part of the optical conductivity is then calculated according to the Kramers-Kronig transformation (3.14).

Finally, the AP-MOKE rotation and ellipticity angles, which depend both on the photon energy $\hbar\omega$ and the polarization state of the probing light beam at normal incidence, are calculated according to the procedure described in Section 3.4.

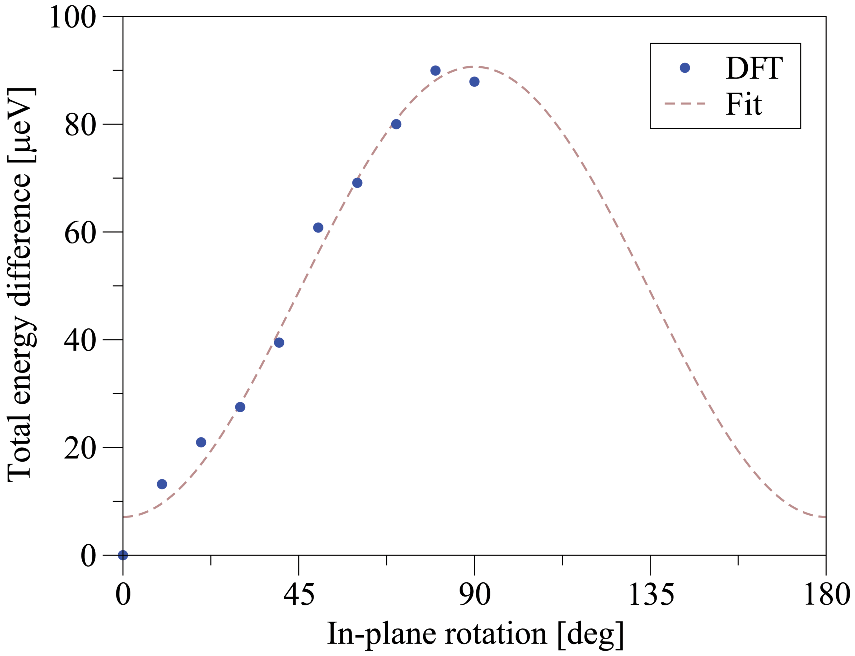

Figure 5.2 – Calculated anisotropy of E_{tot} (filled blue circles) with respect to the angle between $\mathbf{M}$ in the xy plane and the x axis, relative to $E_{\mathrm{tot}}^{\mathrm{min}}$. The DFT results are fitted with a C_{2v}-symmetric function (dashed brown line).

5.3 Results

In order to study the anisotropy of our model system with respect to the direction of the magnetization $\mathbf{M}$, we calculate the total energy per supercell E_{tot} and the real and imaginary part of σ_{xx} for $\mathbf{M}$ oriented along x, y, and z, as well as selected intermediate directions in the xy plane. The total energy E_{tot} exhibits a C_{2v}-symmetric anisotropy of about 88 μeV (see Fig. 5.2), with a minimum of $E_{\mathrm{tot}}^{\mathrm{min}} = -53437.34893468$ Ry for $\mathbf{M}$ oriented along x, and a maximum of $E_{\mathrm{tot}}^{\mathrm{max}} = -53437.34892822$ Ry for $\mathbf{M}$ oriented along y.

In contrast, the anisotropy of the diagonal components of σ with respect to the orientation of $\mathbf{M}$ is found to be negligible over the whole calculated energy range (not shown). Note that all subsequent results are obtained for $\mathbf{M}$ oriented along z, and that σ is given in CGS-Gaussian units.

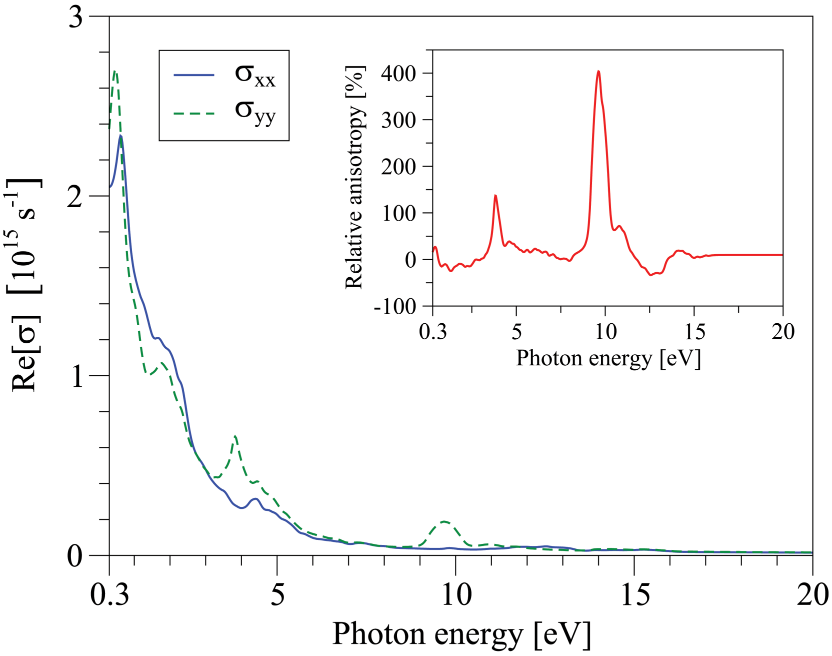

Figure 5.3 – Real part of σ_{xx} (solid blue line) and σ_{yy} (dashed green line) with respect to the photon energy. The inset shows the relative intrinsic anisotropy A_{xy}^{Re} (solid red line) with respect to the photon energy.

Intrinsic Anisotropy

In contrast to its negligible magnetization-induced anisotropy, the Fe/GaAs(001) model system exhibits a significant intrinsic anisotropy. Figure 5.3 shows the differing real parts of σ_{xx} and σ_{yy}. Both components show pronounced peaks of different height centered at 0.5 eV (σ_{yy}) and 0.65 eV (σ_{xx}), and an asymptotic decrease to zero for high energies. The σ_{yy} component shows three intermediate peaks where the relative deviation of the two components is largest. The inset of Fig. 5.3 presents that relative intrinsic anisotropy A_{xy}^{Re} of the real parts of σ_{xx} and σ_{yy} calculated according to

$$A_{xy}^{\mathrm{Re}} = \frac{\mathrm{Re}[\sigma_{yy}] - \mathrm{Re}[\sigma_{xx}]}{\mathrm{Re}[\sigma_{xx}]}. \tag{5.1}$$

While A_{xy}^{Re} is on the order of tens of percent in the visible range of the electromagnetic spectrum, it reaches values above 100% and 400% for 3.9 and 9.6 eV, respectively. Equivalent results for the imaginary part of the optical conductivity are presented in Fig. 5.4. The corresponding relative intrinsic anistropy A_{xy}^{Im}, given by

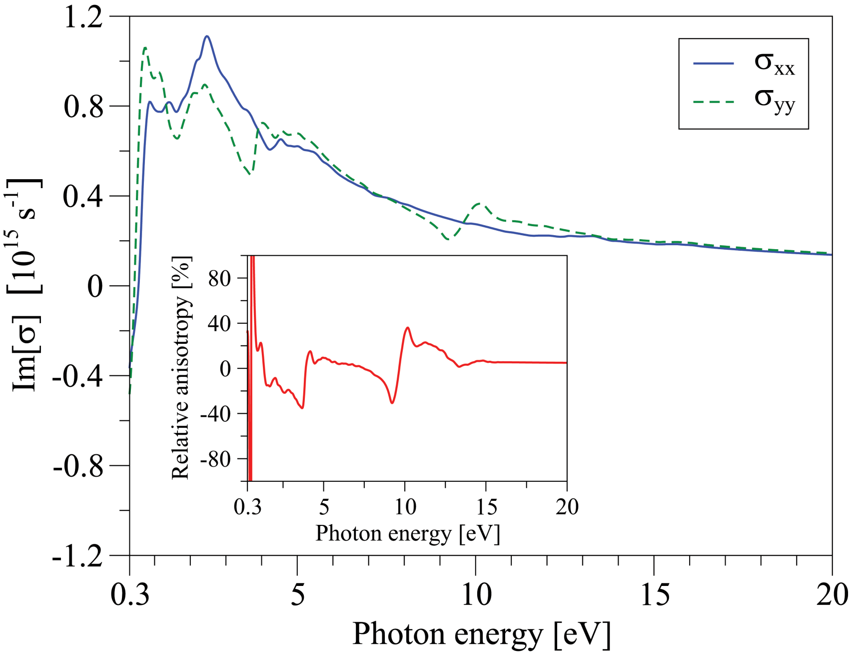

Figure 5.4 – See the caption of Fig. 5.3, but for the imaginary part.

$$A_{xy}^{\mathrm{Im}} = \frac{\mathrm{Im}[\sigma_{yy}] - \mathrm{Im}[\sigma_{xx}]}{\mathrm{Im}[\sigma_{xx}]}, \tag{5.2}$$

is shown in the inset of Fig. 5.4. It is on the order of tens of percent for the most of the calculated energy range, with pronounced extrema at energies of 3.7, 9.3, and 10.2 eV. The divergence at 0.6 eV is a consequence of $\mathrm{Im}[\sigma_{xx}]$ crossing zero at that energy.

Well converged off-diagonal components of the optical conductivity tensor and the dielectric tensor are crucial for the calculation of magneto-optical quantities such as the Kerr rotation θ_K or the Kerr ellipticity ϵ_K. Figure 5.5 shows the result for the off-diagonal component σ_{xy}, which is found to be sufficiently converged at 8100 k points in the full first Brillouin zone. Note that it is an order of magnitude smaller than the diagonal components.

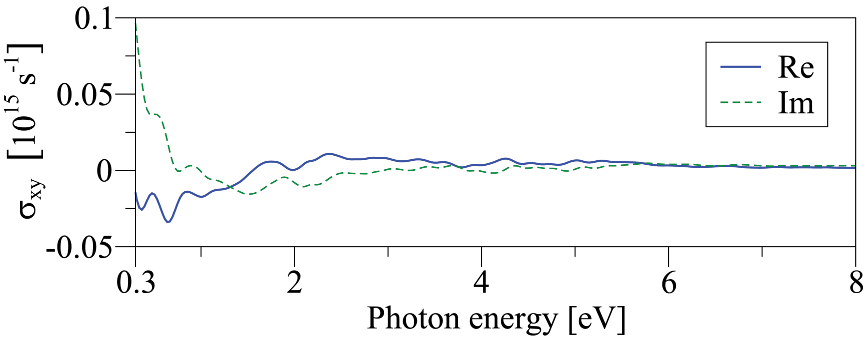

Figure 5.5 – Real (solid blue line) and imaginary part (dashed green line) of the off-diagonal component σ_{xy} of the optical conductivity with respect to the photon energy.

Anisotropic Polar MOKE

The AP-MOKE rotation and ellipticity are obtained according to the procedure described in Section 3.4. Figure 5.6 shows the Kerr rotations for incoming beams polarized along x and y at normal incidence along $-z$. Their absolute values are smaller than 1° over the whole calculated energy range, with the largest deviation at an energy of about 10 eV. The inset shows the absolute difference in Kerr rotation for the x- and y-polarized incoming beams with respect to an experimentally relevant wavelength range. The absolute value of that difference does not exceed 0.1° in the given wavelength range.

Analogous results for the Kerr ellipticity are presented in Fig. 5.7. The absolute value of the ellipticity is smaller than 0.5° for energies smaller than 8 eV, while it is on the order of 1° for higher energies. The largest deviation in Kerr ellipticity for an x- and y-polarized incoming beam occurs at about 9 eV. The inset shows the absolute difference in Kerr ellipticity for the x- and y-polarized case with respect to the wavelength. It is bounded by ±0.1° over the given wavelength range.

The AP-MOKE for arbitrary linear polarization angles of the incoming beam is illustrated by the polar plots in Figs. 5.8–5.11. The azimuth in those plots corresponds to the angle φ (see Sect. 3.4) between the direction of linear polarization of the incoming beam and the x direction, which corresponds to the crystallographic $[1\bar{1}0]$ direction (see Fig. 5.1). The photon energy or the wavelength are given along the radial direction, and the color scale indicates the respective magneto-optical quantity.

These plots serve to visualize the C_{2v} symmetry of AP-MOKE (with the two mirror axes along x and y), which is a manifestation of the underlying effective

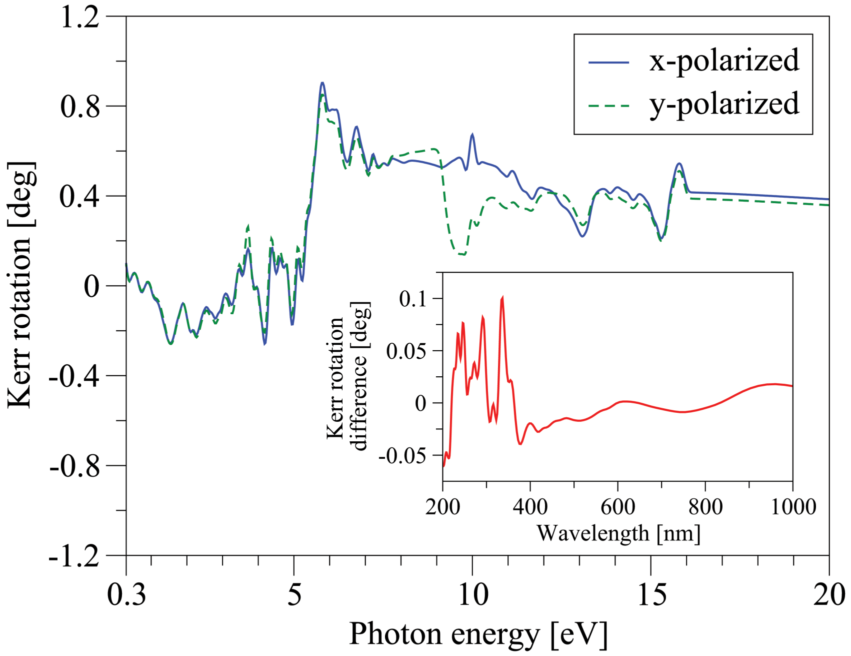

Figure 5.6 – Kerr rotation for beams linearly polarized along x (solid blue line) and y (dashed green line) at normal incidence with respect to the photon energy. The inset shows the absolute difference in Kerr rotation (solid red line) for x- and y-polarized incoming beams with respect to the wavelength.

SOC field symmetry at the Fe/GaAs interface. Depending on its initial polarization state, the reflection of the incoming beam is governed by a transformed dielectric tensor or optical conductivity tensor, which results in an anisotropy of the calculated magneto-optical quantities.

5.4 Conclusions

We studied the anisotropic optical properties of an Fe/GaAs(001) model system from first-principles calculations. While the anisotropy of the optical conductivity with respect to the direction of magnetization in the Fe layer is found to be negligible, the intrinsic anisotropy is significant. The relative intrinsic anisotropy of the real and imaginary part of the optical conductivity in the infrared, visible, and ultraviolet spectrum is on the order of tens of percent, with maxima of up to 100% and 400% at certain energies.

In addition to the optical conductivity, the anisotropic polar magneto-optical Kerr effect was studied for arbitrary linear polarization directions of the probing

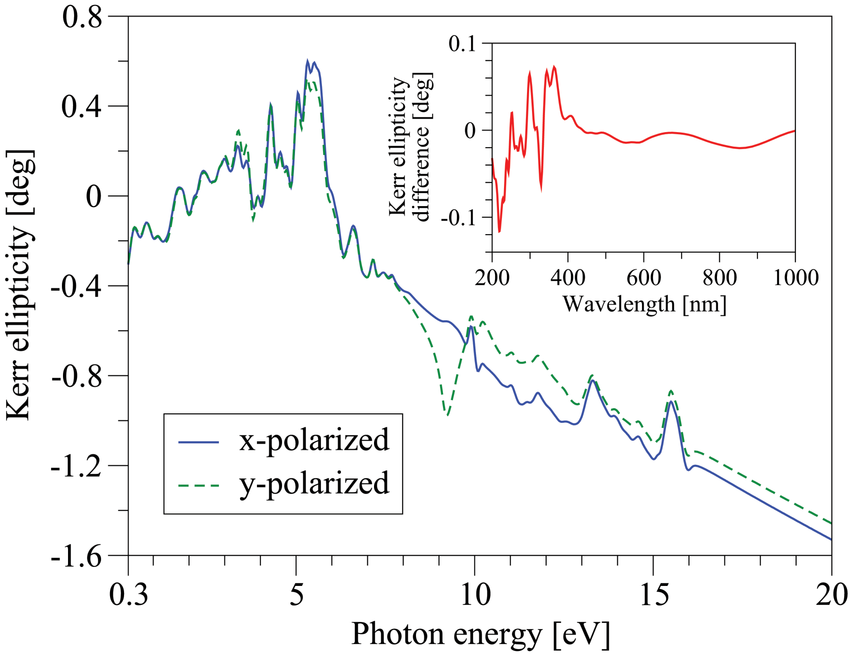

Figure 5.7 – See the caption of Fig. 5.6, but for the Kerr ellipticity.

beam at normal incidence. The resulting anisotropic Kerr rotation and Kerr ellipticity reach values up to about ±1° and reflect the underlying C_{2v} symmetry of the Fe/GaAs(001) interface.

While interface imperfections and protective capping layers [181,182] might lead to quantitatively different experimental results, the qualitative results presented here are expected to be observable in high-quality samples using state-of-the-art optical setups.

In conclusion, our results suggest that the effects of the C_{2v}-symmetric effective SOC fields at the Fe/GaAs(001) interface can be studied by purely optical means in experimentally relevant samples. Interfacial effects, including lowering of the planar symmetry along the interface, play an increasingly important role in the electronic transport and the optics of nanostructures. By controlling the interface electrically, for example, one could also control the spin-orbit fields and thus modify the electric and optical properties of the connected electronic system (in our case ferromagnetic iron).

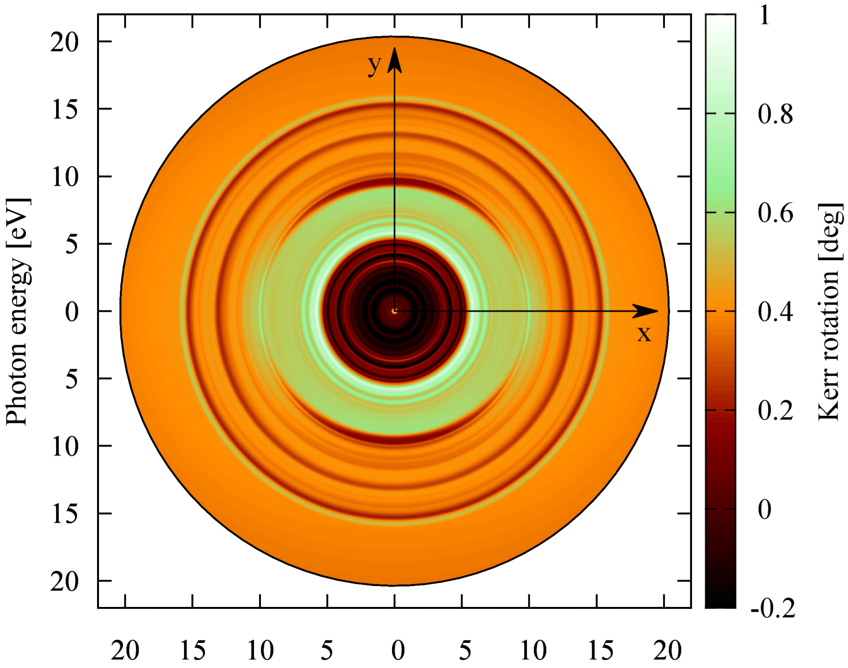

Figure 5.8 – Kerr rotation of a probing beam incident along $-z$ with respect to the photon energy. The azimuth indicates the angle between the x axis and the direction of linear polarization of the probing beam.

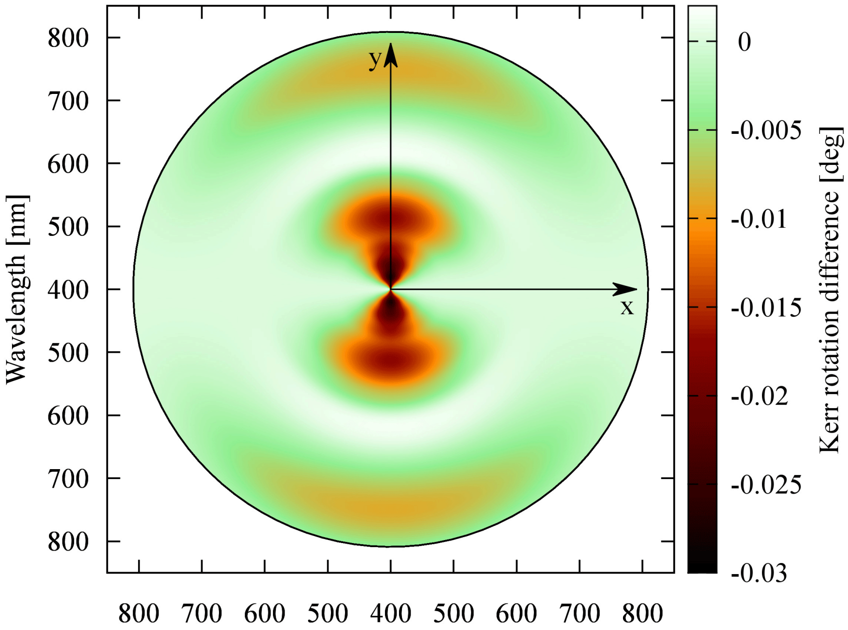

Figure 5.9 – Kerr rotation of a probing beam incident along $-z$, relative to the Kerr rotation of a probing beam polarized along the x direction, with respect to the wavelength. The azimuth indicates the angle between the x axis and the direction of linear polarization of the probing beam.

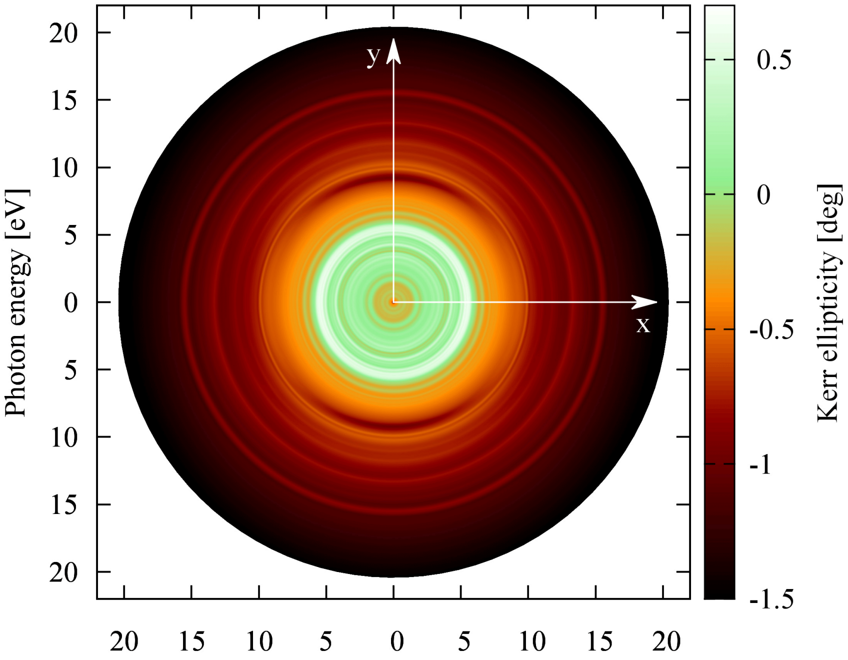

Figure 5.10 – See the caption of Fig. 5.8, but for the Kerr ellipticity.

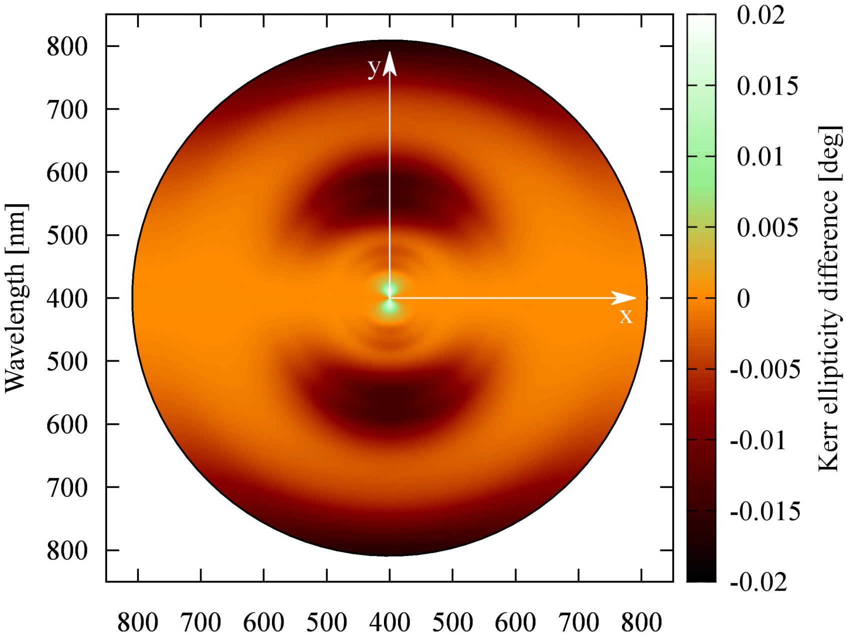

Figure 5.11 – See the caption of Fig. 5.9, but for the Kerr ellipticity.

Outlook

Hydrogenated graphene and Fe/GaAs(001) are candidate systems for novel graphene- and semiconductor-based spintronics devices. However, before they can enter the technology stage, a substantial amount of fundamental research needs to be facilitated and conducted. In this work we have investigated the optical properties of these systems from first-principles DFT calculations. One of our goals was to motivate the use of optical methods in the experimental study of hydrogenated graphene and Fe/GaAs(001).

Indeed, our results suggest that optical methods can be used to study important properties of these systems, such as the effects of the spin-orbit coupling fields at the Fe/GaAs interface. A better understanding of those can help advance the design of efficient spin injection devices. Other interesting properties that can be studied by optical methods are the hydrogenation-induced band gap and magnetism in graphene. Eventually, this could lead to graphene-based spin manipulation devices such as graphene transistors. In the case of hydrogenated graphene, the optical properties themselves are interesting in terms of possible applications involving graphene-based optical elements or sensors.

The model systems investigated in this work were chosen particularly with regard to experimental applicability. Furthermore, our results provide certain design guidelines for possible experiments, for example as to the hydrogen concentration, the structure of the Fe/GaAs interface, and the optimum probing wavelengths. Although we do not claim to have produced quantitatively accurate results (limiting factors are abundant), their semiquantitative character can simplify the design of relevant experiments involving optical methods.

Note that we use carefully chosen *model systems* to make semiquantitative predictions limited by the accuracy of the employed methods and the available computing power. Our choice of DFT methods for the electronic structure calculations, and linear response methods for the optics, was a trade-off between accuracy, applicability, efficiency, ease of use, reproducibility, and passed-down experience in our group. Certainly there are methods that outperform our chosen methods in one or more of these criteria, but they would not have been optimal.

We hope that this work not only produced results that will eventually help advance the study and design of spintronics devices, but also that it provides useful introductory material to newcomers in the field of solid-state *ab initio* calculations, with a particular focus on optical properties. This twofold purpose has been an important goal from the beginning.

Future work seeking to complement the results presented here should consider accurate electronic structure methods such as GW. Going beyond linear response, such a study should make use of more advanced optics methods based on the Bethe-Salpeter equation or on time-dependent DFT, which will become increasingly feasible for large supercells.

Hydrogenated graphene and Fe/GaAs(001) are just two systems that could be used in spintronics applications; there are many more. The potential of spintronics is too intriguing not to advance this field rapidly, and it is very likely that within a decade or so we will witness the advent of generic spintronics devices.

Recent advances have brought spintronics into the scope of not only academic, but also industrial research, which will further accelerate its development. Moreover, large multinational funding projects like the European graphene flagship are likely to result in substantial progress in graphene technology. Material technologies have shaped entire eras— promoting them is a wise decision.

Acknowledgment

Over the last few years I have received invaluable support from many people. First of all, I am deeply indebted to my supervisor Jaroslav Fabian, who has mentored me since my first undergraduate research projects. He has continued to inspire me with his contagious enthusiasm for science. I am especially grateful for the attendances of international conferences he made possible. Every single one was a great experience!

It was Martin Gmitra who taught me the art of *ab initio*. I am thankful for his patience and the knowledge and experience he shared with me. He is a great mentor and friend.

Furthermore, let me express my gratitude to Martin Raith, Benedikt Scharf, and Sergej Konschuh, who not only shared an office with me, but became friends over the years. I was lucky to have the best office mates I could wish for. Thank you for your personal and academic support, and our legendary coffee breaks. Without you, my time in Regensburg would have been rather dull.

I am also thankful to the other current and former members of our group, namely Alex Matos-Abiague, Denis Kochan, Carlos López-Monís, Tobias Frank, Susanne Irmer, and Petra Högl. I very much enjoyed learning and working in this international group of likeable people.

Finally, I would like to thank my friends and family for providing continuous support and encouragement. Special thanks go to Klaus Kronfeldner, for being a good friend and an excellent beekeeper.

This work was funded by *Sonderforschungsbereich 689* and *Graduiertenkolleg 1570* of the German Research Foundation. I gratefully acknowledge their support.

References

[1] Feynman, R. P. *Simulating Physics with Computers.* Int. J. Theor. Phys. **21**, 6/7 (1982).

[2] Putz, S., Gmitra, M. & Fabian, J. *Optical conductivity of hydrogenated graphene from first principles.* Phys. Rev. B **89**, 035437 (2014).

[3] Putz, S., Gmitra, M. & Fabian, J. *Anisotropic optical properties of Fe/GaAs(001) nanolayers from first principles.* Unpublished [arXiv:1309.3463].

[4] Dawkins, R. *The Selfish Gene: 30th Anniversary edition* (Oxford University Press, Oxford, 2006).

[5] Dawkins, R. *The Extended Phenotype: The Long Reach of the Gene* (Oxford University Press, Oxford, 1999).

[6] Anderson, P. W. *More Is Different.* Science **177**, 4047 (1972).

[7] Crick, F. *What Mad Pursuit* (Basic Books, New York, 2008).

[8] Merkle, R. C. *Energy Limits to the Computational Power of the Human Brain.* Foresight Update **6** (1989).

[9] Landau, D. & Binder, K. *A Guide to Monte Carlo Simulations in Statistical Physics* (Cambridge University Press, Cambridge, 2009).

[10] Adler, J. *Educating the next generation of Computational Physicists.* Phys. Procedia (in press).

[11] Moore, G. E. *Cramming more components onto integrated circuits.* Electronics **38**, 8 (1965).

[12] Kohn, W. *Nobel Lecture: Electronic structure of matter—wave functions and density functionals.* Rev. Mod. Phys. **71**, 1253–1266 (1999).

[13] Schrödinger, E. *Quantisierung als Eigenwertproblem I.* Ann. Phys. **79**, 361–376 (1926).

[14] Schrödinger, E. *Quantisierung als Eigenwertproblem II.* Ann. Phys. **79**, 489–527 (1926).

[15] Schrödinger, E. *Quantisierung als Eigenwertproblem III.* Ann. Phys. **80**, 734–756 (1926).

[16] Schrödinger, E. *Quantisierung als Eigenwertproblem IV.* Ann. Phys. **81**, 109–139 (1926).

[17] Thomas, L. H. *The calculation of atomic fields.* Proc. Cambridge Phil. Roy. Soc. **23**, 542–548 (1927).

[18] Fermi, E. *Un metodo statistico per la determinazione di alcune priorieta dell'atome.* Rend. Accad. Naz. Lincei **6**, 602–607 (1927).

[19] Dirac, P. A. M. *Note on exchange phenomena in the Thomas-Fermi atom.* Proc. Cambridge Phil. Roy. Soc. **26**, 376–385 (1930).

[20] Hohenberg, P. C. & Kohn, W. *Inhomogeneous electron gas.* Phys. Rev. **136**, B864–B871 (1964).

[21] Kohn, W. *Density Functional Theory: Fundamentals and Applications.* In Bassani, F., Fumi, F. & Tosi, M. P. (eds.) *Highlights in Condensed Matter Theory* (North Holland, Amsterdam, 1985).

[22] Levy, M. *Electron densities in search of Hamiltonians.* Phys. Rev. A **26**, 1200–1208 (1982).

[23] Kohn, W. & Sham, L. J. *Self-Consistent Equations Including Exchange and Correlation Effects.* Phys. Rev. **140**, A1133–A1138 (1965).

[24] Martin, R. M. *Electronic Structure: Basic Theory and Practical Methods* (Cambridge University Press, Cambridge, 2004).

[25] Perdew, J. P., Ruzsinszky, A., Tao, J., Staroverov, V. N., Scuseria, G. E. & Csonka, G. I. *Prescription for the design and selection of density functional approximations: More constraint satisfaction with fewer fits.* J. Chem. Phys. **123**, 062201 (2005).

[26] Perdew, J. P. & Schmidt, K. *Jacob's ladder of density functional approximations for the exchange-correlation energy.* In Van Doren, V., Van Alsenoy, C. & Geerlings, P. (eds.) *Density Functional Theory and Its Applications to Materials* (American Institute of Physics, Melville, NY, 2001).

[27] Perdew, J. P., Burke, K. & Ernzerhof, M. *Generalized Gradient Approximation Made Simple.* Phys. Rev. Lett. **77**, 3865–3868 (1996).

[28] Becke, A. D. *Density-functional exchange-energy approximation with correct asymptotic behavior.* Phys. Rev. A **38**, 3098 (1988).

[29] Lee, C., Yang, W. & Parr, R. G. *Development of the Colle-Salvetti correlation-energy formula into a functional of the electron density.* Phys. Rev. B **37**, 785 (1988).

[30] Langreth, D. C. & Perdew, J. P. *Theory of nonuniform electronic systems. I. Analysis of the gradient approximation and a generalization that works.* Phys. Rev. B **21**, 5469–5493 (1980).

[31] Tao, J., Perdew, J. P., Staroverov, V. N. & Scuseria, G. E. *Climbing the Density Functional Ladder: Nonempirical Meta–Generalized Gradient Approximation Designed for Molecules and Solids.* Phys. Rev. Lett. **91**, 146401 (2003).

[32] Adamo, C. & Barone, V. *Toward reliable density functional methods without adjustable parameters: The PBE0 model.* J. Chem. Phys. **110**, 6158 (1999).

[33] Perdew, J. P., Staroverov, V. N., Tao, J. & Scuseria, G. E. *Density functional with full exact exchange, balanced nonlocality of correlation, and constraint satisfaction.* Phys. Rev. A **78**, 052513 (2008).

[34] Pickett, W. E. *Pseudopotential methods in condensed matter applications.* Comp. Phys. Rep. **9**, 115 (1989).

[35] Dederichs, P. H. & Zeller, R. *Self-consistency iterations in electronic-structure calculations.* Phys. Rev. B **28**, 5462–5472 (1983).

[36] Broyden, C. G. *A class of methods for solving nonlinear simultaneous equations.* Math. Comput. **19**, 577–593 (1965).

[37] Bendt, P. & Zunger, A. *New approach for solving the density-functional self-consistent-field problem.* Phys. Rev. B **26**, 3114–3137 (1982).

[38] Srivastava, G. P. *Broyden's method for self-consistent field convergence acceleration.* J. Phys. A **17**, L317 (1984).

[39] Vanderbilt, D. & Louie, S. G. *Total energies of diamond (111) surface reconstructions by a linear combination of atomic orbitals method.* Phys. Rev. B **30**, 6118–6130 (1984).

[40] Singh, D., Krakauer, H. & Wang, C. S. *Accelerating the convergence of self-consistent linearized augmented-plane-wave calculations.* Phys. Rev. B **34**, 8391–8393 (1986).

[41] Johnson, D. D. *Modified Broyden's method for accelerating convergence in self-consistent calculations.* Phys. Rev. B **38**, 12807–12813 (1988).

[42] Andersen, O. K. *Linear methods in band theory.* Phys. Rev. B **12**, 3060–3083 (1975).

[43] Singh, D. J. *Planewaves, Pseudopotentials, and the APW Method* (Kluwer Academic Publishers, Boston, 1994).

[44] Slater, J. C. *Wavefunction in a periodic potential.* Phys. Rev. **51**, 846–851 (1937).

[45] Slater, J. C. *An augmented plane wave method for the periodic potential problem.* Phys. Rev. **92**, 603–608 (1953).

[46] Blaha, P., Schwarz, K., Sorantin, P. & Trickey, S. B. *Full-potential, linearized augmented plane wave programs for crystalline systems.* Comp. Phys. Comm. **59(2)**, 399 (1990).

[47] Blaha, P., Schwarz, K., Madsen, G. K. H., Kvasnicka, D. & Luitz, J. *WIEN2k, An Augmented Plane Wave Plus Local Orbitals Program for Calculating Crystal Properties* (Vienna University of Technology, 2001).

[48] Schwarz, K., Blaha, P. & Madsen, G. K. H. *Electronic structure calculations of solids using the WIEN2k package for material sciences.* Comp. Phys. Comm. **147**, 71–76 (2002).

[49] Slater, J. C. *Solid-State and Molecular Theory: A Scientific Biography* (John Wiley and Sons, New York, 1975).

[50] Jones, R. O. *Introduction to Density Functional Theory and Exchange-Correlation Energy Functionals.* In Grotendorst, J., Blügel, S. & Marx, D. (eds.) *Computational Nanoscience: Do It Yourself!*, vol. 31 of *NIC Series*, p.45–70 (John von Neumann Institute for Computing, Jülich, 2006).

[51] Cohen, A. J., Mori-Sánchez, P. & Yang, W. *Challenges for Density Functional Theory.* Chem. Rev. **112**, 289–320 (2012).

[52] Perlmutter, S. *Nobel Lecture: Measuring the acceleration of the cosmic expansion using supernovae.* Rev. Mod. Phys. **84**, 1127–1149 (2012).

[53] The BICEP2 Collaboration. *BICEP2 I: Detection Of B-mode Polarization at Degree Angular Scales*. Unpublished [arXiv:1403.3985].

[54] The BICEP2 Collaboration. *BICEP2 II: Experiment and Three-Year Data Set*. Unpublished [arXiv:1403.4302].

[55] Landau, L. & Lifshitz, E. *Electrodynamics in Continuous Media* (Pergamon Press, New York, 1960).

[56] Pershan, P. S. *Magneto-Optical Effects*. J. Appl. Phys. **38**, 1482 (1967).

[57] Dressel, M. & Grüner, G. *Electrodynamics of Solids* (Cambridge University Press, Cambridge, 2001).

[58] Kronig, R. *On the theory of the dispersion of X-rays*. J. Opt. Soc. Am. **12**, 547–557 (1926).

[59] Kramers, H. A. *La diffusion de la lumiére par les atomes*. Atti del Congresso Internazionale dei Fisici, Como-Pavia-Roma **2**, 545–557 (1927).

[60] Ambrosch-Draxl, C. & Sofo, J. O. *Linear optical properties of solids within the full-potential linearized augmented planewave method*. Comput. Phys. Commun. **175**, 1–14 (2006).

[61] Kerr, J. *On Rotation of the Plane of the Polarization by Reflection from the Pole of a Magnet*. Phil. Mag. **3**, 321 (1877).

[62] Kotissek, P. *et al. Cross-sectional imaging of spin injection into a semiconductor*. Nature Phys. **3**, 872 (2007).

[63] Endres, B. *et al. Bias dependence of spin injection into GaAs from Fe, FeCo, and (Ga,Mn)As contacts*. J. Appl. Phys. **109**, 07C505 (2011).

[64] Endres, B. *et al. Nonuniform current and spin accumulation in a 1μm thick n-GaAs channel*. Appl. Phys. Lett. **100**, 092405 (2012).

[65] Endres, B. *et al. Demonstration of the spin solar cell and spin photodiode effect*. Nature Comm. **4**, 2068 (2013).

[66] Hamrle, J., Ferré, J., Nývlt, M. & Višňovský, i. c. v. *In-depth resolution of the magneto-optical Kerr effect in ferromagnetic multilayers*. Phys. Rev. B **66**, 224423 (2002).

[67] Mansuripur, M. *The Physical Principles of Magneto-optical Recording* (Cambridge University Press, Cambridge, 1998).

[68] Faraday, M. *Experimental Researches in Electricity. Nineteenth Series.* Phil. Trans. R. Soc. Lond. **136**, 1 (1846).

[69] Yeh, P. *Optics of anisotropic layered media: A new 4 × 4 matrix algebra.* Surf. Sci. **96**, 41–53 (1980).

[70] Schoenes, J. *Magneto-Optical Properties of Metals, Alloys and Compounds.* In Cahn, R. W., Haasen, P. & Kramer, E. J. (eds.) *Materials Science and Technology*, vol. 3a, p.147–225 (VCH-Verlag, Weinheim, 1992).

[71] Jones, R. C. *A New Calculus for the Treatment of Optical Systems.* J. Opt. Soc. Am. **31**, 488–493 (1941).

[72] Born, M. & Wolf, E. *Principles of Optics* (Pergamon Press, Oxford, 1980).

[73] Oppeneer, P. M. *Magneto-Optical Kerr Spectra.* In Buschow, K. H. J. (ed.) *Handbook of Magnetic Materials*, vol. 13, 229–422 (North-Holland, Amsterdam, 2001).

[74] Oppeneer, P. M., Galanakis, I., James, P., Eriksson, O. & Ravindran, P. *Theory of the anisotropic magneto-optical Kerr effect in artificial FeAu and MnAu and in* XAu_4 *(X=V, Cr, Mn) compounds.* J. Magn. Soc. Jpn. **23**, S1 21–26 (1999).

[75] Fumagalli, P. *Magneto-optical Kerr effect study on the high field superconductors* $Eu_{1\text{-}x}Pb_xMo_6S_8$ *and* $Eu_{1\text{-}x}Sn_xMo_6S_{8\text{-}y}Se_y$. Ph.D. thesis, Swiss Federal Institute of Technology, Zurich (1990).

[76] Oppeneer, P. M., Sticht, J., Maurer, T. & Kübler, J. *Ab initio investigation of microscopic enhancement factors in tuning the magneto-optical Kerr effect.* Z. Phys. B **88**, 309 (1992).

[77] Novoselov, K. S. *et al. Electric field effect in atomically thin carbon films.* Science **306**, 666–669 (2004).

[78] Geim, A. K. & Novoselov, K. S. *The rise of graphene.* Nature Mater. **6**, 183–191 (2007).

[79] Castro Neto, A. H., Peres, N. M. R., Novoselov, K. S. & Geim, A. K. *The electronic properties of graphene.* Rev. Mod. Phys. **81**, 109–162 (2009).

[80] Lee, J.-H. *et al. Wafer-Scale Growth of Single-Crystal Monolayer Graphene on Reusable Hydrogen-Terminated Germanium.* Science **344**, 286–289 (2014).

[81] Geim, A. K. *Graphene: Status and Prospects.* Science **324**, 1530 (2009).

[82] Novoselov, K. S., Fal'ko, V. I., Colombo, L., Gellert, P. R., Schwab, M. G. & Kim, K. *A roadmap for graphene.* Nature **490**, 192–200 (2012).

[83] Wallace, P. R. *The band theory of graphite.* Phys. Rev. **71**, 622–634 (1947).

[84] McClure, J. W. *Diamagnetism of graphite.* Phys. Rev. **104**, 666–671 (1956).

[85] Slonczewski, J. C. & Weiss, P. R. *Band structure of graphite.* Phys. Rev. **109**, 272–279 (1958).

[86] Semenoff, G. W. *Condensed-matter simulation of a three-dimensional anomaly.* Phys. Rev. Lett. **53**, 2449–2452 (1984).

[87] Fradkin, E. *Critical behavior of disordered degenerate semiconductors.* Phys. Rev. B **33**, 3263–3268 (1986).

[88] Haldane, F. D. M. *Model for a quantum Hall effect without Landau levels: Condensed-matter realization of the parity anomaly.* Phys. Rev. Lett. **61**, 2015–2018 (1988).

[89] Novoselov, K. S. *et al. Two-Dimensional Gas of Massless Dirac Fermions in Graphene.* Nature **438**, 197–200 (2005).

[90] Katsnelson, M. I., Novoselov, K. S. & Geim, A. K. *Chiral tunnelling and the Klein paradox in graphene.* Nature Phys. **2**, 620–625 (2006).

[91] Katsnelson, M. I. *Zitterbewegung, chirality, and minimal conductivity in graphene.* Eur. Phys. J. B **51**, 157–160 (2006).

[92] Mermin, N. D. *Crystalline order in two dimensions.* Phys. Rev. **176**, 250–254 (1968).

[93] Meyer, J. C., Geim, A. K., Katsnelson, M. I., Novoselov, K. S., Booth, T. J. & Roth, S. *The structure of suspended graphene sheets.* Nature **446**, 60–63 (2007).

[94] Nair, R. R. *et al. Fine Structure Constant Defines Visual Transparency of Graphene.* Science **320**, 1308 (2008).

[95] Novoselov, K. S., Jiang, D., Schedin, F., Booth, T. J., Khotkevich, V. V., Morozov, S. V. & Geim, A. K. *Two-dimensional atomic crystals.* PNAS **102**, 10451–10453 (2005).

[96] Schwierz, F. *Graphene transistors.* Nature Nanotech. **5**, 487–496 (2010).

[97] Han, M. Y., Özyilmaz, B., Zhang, Y. & Kim, P. *Energy Band-Gap Engineering of Graphene Nanoribbons.* Phys. Rev. Lett. **98**, 206805 (2007).

[98] Li, X., Wang, X., Zhang, L., Lee, S. & Dai, H. *Chemically Derived, Ultrasmooth Graphene Nanoribbon Semiconductors.* Science **319**, 1229–1232 (2008).

[99] Giovannetti, G., Khomyakov, P. A., Brocks, G., Kelly, P. J. & van den Brink, J. *Substrate-induced band gap in graphene on hexagonal boron nitride: Ab initio density functional calculations.* Phys. Rev. B **76**, 073103 (2007).

[100] Balog, R. *et al. Bandgap opening in graphene induced by patterned hydrogen adsorption.* Nature Mater. **9**, 315–319 (2010).

[101] Schedin, F., Geim, A. K., Morozov, S. V., Hill, E. W., Blake, P., Katsnelson, M. I. & Novoselov, K. S. *Detection of individual gas molecules adsorbed on graphene.* Nature Mater. **6**, 652–655 (2007).

[102] Gierz, I., Riedl, C., Starke, U., Ast, C. R. & Kern, K. *Atomic Hole Doping of Graphene.* Nano Lett. **8**, 4603–4607 (2008).

[103] Boukhvalov, D. W. & Katsnelson, M. I. *Chemical functionalization of graphene.* J. Phys.: Condens. Matter **21**, 344205 (2009).

[104] Wehling, T., Katsnelson, M. & Lichtenstein, A. *Adsorbates on graphene: Impurity states and electron scattering.* Chem. Phys. Lett. **476**, 125–134 (2009).

[105] Hossain, M. Z. *et al. Chemically homogeneous and thermally reversible oxidation of epitaxial graphene.* Nature Chem. **4**, 305–309 (2012).

[106] Robinson, J. T. *et al. Properties of Fluorinated Graphene Films.* Nano Lett. **10**, 3001–3005 (2010).

[107] Sahin, H., Topsakal, M. & Ciraci, S. *Structures of fluorinated graphene and their signatures.* Phys. Rev. B **83**, 115432 (2011).

[108] Duplock, E. J., Scheffler, M. & Lindan, P. J. D. *Hallmark of Perfect Graphene.* Phys. Rev. Lett. **92**, 225502 (2004).

[109] Boukhvalov, D. W., Katsnelson, M. I. & Lichtenstein, A. I. *Hydrogen on graphene: Electronic structure, total energy, structural distortions and magnetism from first-principles calculations.* Phys. Rev. B **77**, 035427 (2008).

[110] Ryu, S., Han, M. Y., Maultzsch, J., Heinz, T. F., Kim, P., Steigerwald, M. L. & Brus, L. E. *Reversible Basal Plane Hydrogenation of Graphene.* Nano Lett. **8**, 4597–4602 (2008).

[111] Haberer, D. *et al. Tunable band gap in hydrogenated quasi-free-standing graphene.* Nano Lett. **10**, 3360–3366 (2010).

[112] Luo, Z. *et al. Modulating the electronic structures of graphene by controllable hydrogenation.* Appl. Phys. Lett. **97**, 233111 (2010).

[113] Sofo, J. O., Chaudhari, A. S. & Barber, G. D. *Graphane: A two-dimensional hydrocarbon.* Phys. Rev. B **75**, 153401 (2007).

[114] Elias, D. C. *et al. Control of Graphene's Properties by Reversible Hydrogenation: Evidence for Graphane.* Science **323**, 610–613 (2009).

[115] Zhou, J., Wang, Q., Sun, Q., Chen, X. S., Kawazoe, Y. & Jena, P. *Ferromagnetism in Semihydrogenated Graphene Sheet.* Nano Lett. **9**, 3867 (2009).

[116] Yazyev, O. V. & Helm, L. *Defect-induced magnetism in graphene.* Phys. Rev. B **75**, 125408 (2007).

[117] Yazyev, O. V. *Magnetism in disordered graphene and irradiated graphite.* Phys. Rev. Lett. **101**, 037203 (2008).

[118] Yazyev, O. V. *Emergence of magnetism in graphene materials and nanostructures.* Rep. Prog. Phys. **73**, 056501 (2010).

[119] Wang, Y., Huang, Y., Song, Y., Zhang, X., Ma, Y., Liang, J. & Chen, Y. *Room-Temperature Ferromagnetism of Graphene.* Nano Lett. **9**, 220–224 (2009).

[120] McCreary, K. M., Swartz, A. G., Han, W., Fabian, J. & Kawakami, R. K. *Magnetic Moment Formation in Graphene Detected by Scattering of Pure Spin Currents.* Phys. Rev. Lett. **109**, 186604 (2012).

[121] Rudenko, A. N., Keil, F. J., Katsnelson, M. I. & Lichtenstein, A. I. *Exchange interactions and frustrated magnetism in single-side hydrogenated and fluorinated graphene.* Phys. Rev. B **88**, 081405 (2013).

[122] Žutić, I., Fabian, J. & Das Sarma, S. *Spintronics: Fundamentals and applications.* Rev. Mod. Phys. **76**, 323–410 (2004).

[123] Fabian, J., Matos-Abiague, A., Ertler, C., Stano, P. & Žutić, I. *Semiconductor Spintronics.* Acta Phys. Slovaca **57**, 565–907 (2007).

[124] Gmitra, M., Kochan, D. & Fabian, J. *Spin-Orbit Coupling in Hydrogenated Graphene.* Phys. Rev. Lett. **110**, 246602 (2013).

[125] Konstantatos, G. *et al. Hybrid graphene-quantum dot phototransistors with ultrahigh gain.* Nature Nanotech. **7**, 363–8 (2012).

[126] Bonaccorso, F., Sun, Z., Hasan, T. & Ferrari, A. C. *Graphene photonics and optoelectronics.* Nature Photon. **4**, 611–622 (2010).

[127] Mueller, T., Xia, F. & Avouris, P. *Graphene photodetectors for high-speed optical communications.* Nature Photon. **4**, 297–301 (2010).

[128] Xia, F., Mueller, T., Lin, Y.-m., Valdes-Garcia, A. & Avouris, P. *Ultrafast graphene photodetector.* Nature Nanotech. **4**, 839–843 (2009).

[129] Gusynin, V. P., Sharapov, S. G. & Carbotte, J. P. *Magneto-optical conductivity in graphene.* J. Phys.: Condens. Matter **19**, 026222 (2007).

[130] Dawlaty, J. M., Shivaraman, S., Strait, J. & George, P. *Measurement of the optical absorption spectra of epitaxial graphene from terahertz to visible.* Appl. Phys. Lett. **93**, 131905 (2008).

[131] Mak, K. F., Sfeir, M. Y., Wu, Y., Lui, C. H., Misewich, J. A. & Heinz, T. F. *Measurement of the Optical Conductivity of Graphene.* Phys. Rev. Lett. **101**, 196405 (2008).

[132] Stauber, T., Peres, N. M. R. & Geim, A. K. *Optical conductivity of graphene in the visible region of the spectrum.* Phys. Rev. B **78**, 085432 (2008).

[133] Peres, N. M. R., Ribeiro, R. M. & Castro Neto, A. H. *Excitonic Effects in the Optical Conductivity of Gated Graphene.* Phys. Rev. Lett. **105**, 055501 (2010).

[134] Nicol, E. J. & Carbotte, J. P. *Optical conductivity of bilayer graphene with and without an asymmetry gap.* Phys. Rev. B **77**, 155409 (2008).

[135] Crassee, I., Levallois, J., van der Marel, D., Walter, A. L., Seyller, T. & Kuzmenko, A. B. *Multicomponent magneto-optical conductivity of multilayer graphene on SiC.* Phys. Rev. B **84**, 035103 (2011).

[136] Kuzmenko, A. B., van Heumen, E., Carbone, F. & van der Marel, D. *Universal Optical Conductance of Graphite.* Phys. Rev. Lett. **100**, 117401 (2008).

[137] Trevisanutto, P. E., Holzmann, M., Côté, M. & Olevano, V. *Ab initio high-energy excitonic effects in graphite and graphene.* Phys. Rev. B **81**, 121405 (2010).

[138] Falkovsky, L. A. *Quantum magneto-optics of graphite with trigonal warping.* Phys. Rev. B **84**, 115414 (2011).

[139] Ugawa, A., Hwang, J., Gommans, H., Tashiro, H., Rinzler, A. & Tanner, D. *Far-infrared to visible optical conductivity of single-wall carbon nanotubes.* Curr. Appl. Phys. **1**, 45 (2001).

[140] Giannozzi, P. *et al. QUANTUM ESPRESSO: a modular and open-source software project for quantum simulations of materials.* J. Phys.: Condens. Matter **21**, 395502 (2009).

[141] Vanderbilt, D. *Soft self-consistent pseudopotentials in a generalized eigenvalue formalism.* Phys. Rev. B **41**, 7892 (1990).

[142] Feynman, R. P. *Forces in Molecules.* Phys. Rev. **56**, 340–343 (1939).

[143] Pulay, P. *Ab initio calculation of force constants and equilibrium geometries in polyatomic molecules.* Mol. Phys. **17**, 197–204 (1969).

[144] Monkhorst, H. J. & Pack, J. D. *Special points for Brillouin-zone integrations.* Phys. Rev. B **13**, 5188 (1976).

[145] Blöchl, P. E., Jepsen, O. & Andersen, O. K. *Improved tetrahedron method for Brillouin-zone integrations.* Phys. Rev. B **49**, 16223 (1994).

[146] Ando, T., Zheng, Y. & Suzuura, H. *Dynamical Conductivity and Zero-Mode Anomaly in Honeycomb Lattices.* J. Phys. Soc. Jpn. **71**, 1318–1324 (2002).

[147] Gusynin, V. P., Sharapov, S. G. & Carbotte, J. P. *Unusual Microwave Response of Dirac Quasiparticles in Graphene.* Phys. Rev. Lett. **96**, 256802 (2006).

[148] Falkovsky, L. A. & Varlamov, A. A. *Space-time dispersion of graphene conductivity.* Eur. Phys. J. B **56**, 281–284 (2007).

[149] Casolo, S., Flage-Larsen, E., Løvvik, O. M., Darling, G. R. & Tantardini, G. F. *Role of the self-interaction error in studying chemisorption on graphene from first-principles.* Phys. Rev. B **81**, 205412 (2010).

[150] Lebègue, S., Klintenberg, M., Eriksson, O. & Katsnelson, M. I. *Accurate electronic band gap of pure and functionalized graphane from GW calculations.* Phys. Rev. B **79**, 245117–245117 (2009).

[151] Fiori, G., Lebègue, S., Betti, A., Michetti, P., Klintenberg, M., Eriksson, O. & Iannaccone, G. *Simulation of hydrogenated graphene field-effect transistors through a multiscale approach.* Phys. Rev. B **82**, 153404 (2010).

[152] Kharche, N. & Nayak, S. K. *Quasiparticle band gap engineering of graphene and graphone on hexagonal boron nitride substrate.* Nano Lett. **11**, 5274 (2011).

[153] Von Neumann, J. *First Draft of a Report on the EDVAC.* In *IEEE Annals of the History of Computing*, vol. 15, Issue 4, p.27–75 (1993).

[154] Datta, S. & Das, B. *Electronic analog of the electrooptic modulator.* Appl. Phys. Lett. **56**, 665–667 (1990).

[155] Jonker, B. T. *Progress toward electrical injection of spin-polarized electrons into semiconductors.* Proc. IEEE **91**, 5 (2003).

[156] Žutić, I. & Dery, H. *Spintronics: Taming spin currents.* Nat. Mater. **10**, 647 (2011).

[157] Hanbicki, A. T., Jonker, B. T., Itskos, G., Kioseoglou, G. & Petrou, A. *Efficient electrical spin injection from a magnetic metal/tunnel barrier contact into a semiconductor.* Appl. Phys. Lett. **80**, 1240 (2002).

[158] Chambers, S. A., Xu, F., Chen, H. W., Vitomirov, I. M., Anderson, S. B. & Weaver, J. H. *Simultaneous epitaxy and substrate out-diffusion at a metal-semiconductor interface: Fe/GaAs(001)-c(8x2).* Phys. Rev. B **34**, 6605 (1986).

[159] Waldrop, J. R. & Grant, R. W. *Interface chemistry of metal-GaAs Schottky-barrier contacts.* Appl. Phys. Lett. **34**, 630 (1979).

[160] Krebs, J. J., Jonker, B. T. & Prinz, G. A. *Properties of Fe single-crystal films grown on (100)GaAs by molecular-beam epitaxy.* J. Appl. Phys. **61**, 2596 (1987).

[161] Wastlbauer, G. & Bland, J. A. C. *Structural and magnetic properties of ultrathin epitaxial Fe films on GaAs(001) and related semiconductor substrates.* Adv. Phys. **54**, 137–219 (2005).

[162] Li, C. H. *et al. Spin injection across (110) interfaces: Fe/GaAs(110) spin-light-emitting diodes.* Appl. Phys. Lett. **85**, 1544 (2004).

[163] Grünebohm, A., Herper, H. C. & Entel, P. *Ab initio study of the interface properties of Fe/GaAs(110).* Phys. Rev. B **80**, 064417 (2009).

[164] Ashraf, T., Gusenbauer, C., Stangl, J., Hesser, G., Wegscheider, M. & Koch, R. *Stress and interdiffusion during molecular beam epitaxy of Fe on As-rich GaAs(001).* J. Phys.: Condens. Matter **23**, 042001 (2011).

[165] Fleet, L. R. *et al. Correlating the interface structure to spin injection in abrupt Fe/GaAs(001) films.* Phys. Rev. B **87**, 024401 (2013).

[166] Gester, M., Daboo, C., Hicken, R. J., Gray, S. J., Ercole, A. & Bland, J. A. C. *Continuous evolution of the in-plane magnetic anisotropies with thickness in epitaxial Fe films.* J. Appl. Phys. **80**, 347 (1996).

[167] Zölfl, M. *et al. Magnetic films epitaxially grown on semiconductors.* J. Magn. Magn. Mater. **175**, 16 (1997).

[168] Brockmann, M., Zölfl, M., Miethaner, S. & Bayreuther, G. *In-plane volume and interface magnetic anisotropies in epitaxial Fe films on GaAs(001).* J. Magn. Magn. Mater. **198-199**, 384–386 (1999).

[169] Bensch, F., Moosbühler, R. & Bayreuther, G. *Onset of magnetic anisotropy in epitaxial Fe films on GaAs(001).* J. Appl. Phys. **91**, 8754 (2002).

[170] Zakeri, K., Kebe, T., Lindner, J. & Farle, M. *Magnetic anisotropy of Fe/GaAs(001) ultrathin films investigated by in situ ferromagnetic resonance.* J. Magn. Magn. Mater. **299**, L1–L10 (2006).

[171] Bayreuther, G., Premper, J., Sperl, M. & Sander, D. *Uniaxial magnetic anisotropy in Fe/GaAs(001): Role of magnetoelastic interactions.* Phys. Rev. B **86**, 054418 (2012).

[172] Moser, J., Matos-Abiague, A., Schuh, D., Wegscheider, W., Fabian, J. & Weiss, D. *Tunneling Anisotropic Magnetoresistance and Spin-Orbit Coupling in Fe/GaAs/Au Tunnel Junctions.* Phys. Rev. Lett. **99**, 056601 (2007).

[173] López-Monís, C., Matos-Abiague, A. & Fabian, J. *Tunneling magnetothermopower in magnetic tunnel junctions.* Phys. Rev. B **89**, 054419 (2014).

[174] López-Monís, C., Matos-Abiague, A. & Fabian, J. *Tunneling Anisotropic Thermopower and Seebeck Effects in Magnetic Tunnel Junctions.* Unpublished [arXiv:1309.3463].

[175] Matos-Abiague, A. & Fabian, J. *Anisotropic tunneling magnetoresistance and tunneling anisotropic magnetoresistance: Spin-orbit coupling in magnetic tunnel junctions.* Phys. Rev. B **79**, 155303 (2009).

[176] Matos-Abiague, A., Gmitra, M. & Fabian, J. *Angular dependence of the tunneling anisotropic magnetoresistance in magnetic tunnel junctions.* Phys. Rev. B **80**, 045312 (2009).

[177] Gmitra, M., Matos-Abiague, A., Draxl, C. & Fabian, J. *Magnetic Control of Spin-Orbit Fields: A First-Principles Study of Fe/GaAs Junctions.* Phys. Rev. Lett. **111**, 036603 (2013).

[178] Bychkov, A. & Rashba, E. I. *Properties of a 2D electron gas with lifted spectral degeneracy.* JETP Lett. **39**, 78 (1984).

[179] Dresselhaus, G. *Spin-orbit coupling effects in zinc blende structures.* Phys. Rev. **100**, 580–586 (1955).

[180] Trushin, M. & Schliemann, J. *Anisotropic current-induced spin accumulation in the two-dimensional electron gas with spin-orbit coupling.* Phys. Rev. B **75**, 155323 (2007).

[181] Tacchi, S., Stollo, A., Gubbiotti, G., Carlotti, G., Košuth, M. & Ebert, H. *Influence of Au capping layer on the magnetic properties of Fe/GaAs(001) ultrathin films.* Surf. Sci. **601**, 4311 (2007).

[182] Lei, N., Tian, Y., Tian, C. S., Zhou, L. H., Yin, L. F., Dong, G. S. & Jin, X. F. *Capping effects of Au on Fe/GaAs(001) studied by magneto-optical Kerr effect.* Thin Solid Films **515**, 7290 (2007).